THEORY AND DESIGN OF SMITH-PURCELL SEMICONDUCTOR TERAHERTZ SOURCES

A Dissertation

by

DON DEEWAYNE SMITH

Submitted to the Office of Graduate and Professional Studies of
Texas A&M University
in partial fulfillment of the requirements for the degree of

DOCTOR OF PHILOSOPHY

Chair of Committee,	Alexey Belyanin
Committee Members,	Christi K. Madsen
	Peter M. McIntyre
	Donald G. Naugle
Head of Department,	George R. Welch

December 2013

Major Subject: Applied Physics

ABSTRACT

A wealth of unique physics makes the frequency band from 0.3 – 3.0THz technologically relevant, and compact room-temperature semiconductor sources would enable many new spectroscopic applications. All semiconductor sources currently have serious difficulties reaching the THz, and no THz device *of any type* operates on the full range at room temperature. This dissertation proposes a novel semiconductor source which utilizes the transferred-electron (Gunn) effect and the Smith-Purcell effect to operate over the majority of the 0.3 – 3.0THz band at room temperature. Mathematical derivations provide a theoretical analysis of the device and computer simulations explore its performance as a function of design.

The dissertation begins with a description of the device and an overview of the field of terahertz science. A literature review establishes the relevance and uniqueness of the work and highlights the physical principles required to model the operation of the device. Next, the mathematical "machinery" required model the device is built, starting with a derivation of the Butcher-Fawcett "equal-areas" method used to calculate the Gunn effect. A description of the computer code written to implement the equal-areas method and examples validating its correct operation follow. A derivation of the Smith-Purcell effect provides a closed-form solution for the electric field, which is then combined with the Gunn effect results.

With the theoretical methods thus established, a detailed explanation of the simulation methods used to model the device is provided, followed by a detailed comparison between theory and simulation – in which it is shown that the theoretical methods display a high degree of agreement with computer simulations of the device. The results of an extensive design study are then presented that map the range of

predicted results for this terahertz device. The Smith-Purcell device is found to perform better than or comparable to any state-of-the-art semiconductor THz source. At room temperature, a single $100\mu m$-wide device is predicted to generate $365\mu W$ of power at 0.28THz and $1\mu W$ at 2.5THz. The dissertation concludes with suggestions for subsequent research – most urgently for an attempt to experimentally verify the predictions of this work.

DEDICATION

To my family who has patiently supported me throughout this very long process.

ACKNOWLEDGEMENTS

Firstly – and by far most importantly – I acknowledge my family, without whom my life would be a meaningless mess. My wife, Luci, has endured more than anyone should have to put up with in two lifetimes while I've tilted at the academic windmill (twice), comprising the majority of our adult lives. You are the one that showed me that there's a real world outside my head that can be a wonderful place – I love you. Thank you for not letting me quit when the goal was so close at hand. It's because of you that I really am one of the luckiest men alive and that is a fact.

I acknowledge and am looking forward to the time when our children – Nikki, Trey, Sidney, and Marcus – know their father without the burden of unfinished business always looming over his head. Likewise, we became grandparents over this long course of study, and I think Zachary and Avery will enjoy their Papi just a little more than they already do. I love my big family and thank you guys for being the most awesome joy – it's because of you and your mother that I cannot wait to get home from work every single day. Thank you.

I acknowledge the crucial role that my parents played in making this journey possible. My mother Ethel has been a rock of support throughout my entire life, not just during graduate school. My late father, DeWayne (Smitty), was not able to see my second trip through school firsthand but I can attest that I have felt his presence often and he drops by in dreams occasionally to assure me that I am still on the right path. Thank you both.

This work could not have been completed without the patient support of my advisor, Dr. Alexey Belyanin. I greatly appreciate you taking on a new student from a different discipline and allowing him to drift from quantum optics into high-

frequency electronics. I don't think there are many faculty members who would have put up with a student that let their research drift on for years like you did with me. Thank you.

Dr. Peter McIntyre has been a spectacular mentor and role model for a long time...since about 1990, to be exact. Without Peter, it's doubtful that my graduate career in physics could have even started at Texas A&M. There is no doubt that I could have had the spectacular career I've enjoyed thus far without his leadership and support throughout my first pass through graduate school between 1989 and 1994. It was in his labs that I discovered semiconductors, so the jury is still out on whether that is a blessing or a curse...and it was Peter who found me a spot when I was laid off from work in 2002 and decided to come back for a Ph.D. at the tender age of 37. Perhaps most importantly, Peter modeled the personal responsibility that all scientists and technologists ought to have in trying to use our gifts and knowledge for the betterment of all people. Thank you.

I would be remiss to thank my employers and managers over the past several years for their acknowledgement and sometimes grudging support of the load I was doggedly determined to drag along with me. Looking back, it is easy to see the insanity of expecting to juggle being a full-time engineer, a full-time husband, a full-time father, and a full-time graduate student. It is evident that I have dropped all these balls repeatedly – my juggling skills leave a lot to be desired. Thank you.

Speaking of juggling life skills, special thanks go to the group of men that have been my steadfast social network for the past four years. Collectively, you group of Cream Puffs (also sometimes known as the ΣΜΦ fraternity) have shown me by living, breathing example how a real man walks through life with dignity, integrity, and compassion. You guys are my heroes and someday I want to be just like you if I ever grow up. Thank you.

Finally, special thanks to Mr. Randy Rossi for playing the role of wise counsel for the past few years – adult supervision has proven to be quite worthwhile during this last season of change. I doubt very seriously that I could have gotten over the last couple hills without your help. Thank you.

TABLE OF CONTENTS

LIST OF FIGURES

FIGURE Page

LIST OF TABLES

TABLE Page

1. INTRODUCTION

Figure 1.1 illustrates a proposed room-temperature semiconductor device that combines the Smith-Purcell effect and the transferred electron effect to generate coherent, variable-frequency narrowband terahertz (THz) radiation. These physical effects have been extensively but *separately* studied for over 40 years. To the best of our knowledge, this is the first report *jointly* applying them to solve a specific problem – namely, to design a compact THz source. The device consists of *three* monolithic layers – a *bulk* semiconductor, a dielectric spacer, and a metallic grating.

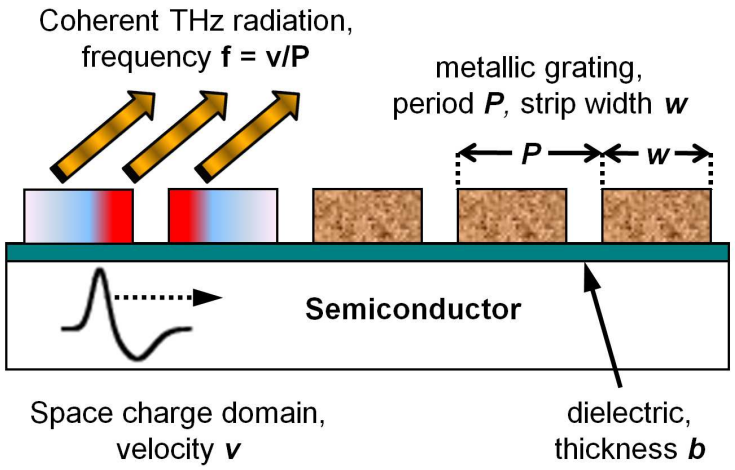

Figure 1.1: Smith-Purcell Semiconductor THz source. Its performance compares favorably with state of the art and it is compatible with silicon manufacturing. [1] Reprinted with permission from D. D. Smith and A. Belyanin, "Room-temperature semiconductor coherent Smith-Purcell terahertz sources," Appl. Phys. Lett., vol. 98, no. 6, pp. 063 501-063 504, Feb. 2011. Copyright 2011, AIP Publishing LLC.

As will be discussed below, the transferred electron (or Gunn) effect is a well-known solid-state phenomenon in high-frequency semiconductor device physics. Un-

der a sufficiently strong applied electric field, semiconductors with suitable energy band structure exhibit *negative differential resistance* (NDR). At the onset of NDR, fundamental conduction current instability causes spontaneous high-frequency current oscillation. Theoretical prediction of the effect was made in the early 1960's by the team of Ridley and Watkins and independently by Hilsum. For this reason, many textbooks refer to the "Ridley-Watkins-Hilsum" effect. [2, 3]

The transferred electron effect was first experimentally observed by Gunn in 1964, which is why his name is also used synonymously with the effect. [4] Gunn demonstrated that a simple semiconductor block with electrodes affixed to either end formed a two-terminal high-frequency device known as the *Gunn diode*. Gunn diodes operate in different oscillation modes. Of particular interest to this research is the *freely-traveling dipole mode*, in which a narrow space-charge packet called a *Gunn domain* forms at one terminal of the device and travels to the other terminal at constant velocity.

In the THz device proposed in Figure 1.1, the Gunn domain induces an image-charge dipole on each grating tooth as it traverses the semiconductor layer. These image-charge dipoles radiate via the Smith-Purcell effect. In 1953, Smith and Purcell hypothesized that a metallic diffraction grating placed near a constant-current (DC) electron beam in vacuum would generate electromagnetic radiation with frequency equal to the ratio of the electron velocity to the grating period. Using a high-energy electron beam, their experiments created visible light. [5] This discovery led to the development of several different high power vacuum-electronic devices. As will be discussed below, several key concepts of these devices can be applied to the present work, but first we give an overview of the importance of the terahertz regime.

1.1 Relevance of Terahertz (THz) Technology

Terahertz (THz) science and technology has experienced an explosion of interest in the past several decade, but it is interesting to note that the field *actually began in the 1890's* – shortly after Hertz experimentally confirmed Maxwell's prediction of radio waves. Overviews by Wiltse (1984) and Siegel (2002) provide the interested reader with a concise and well-referenced history of how THz science emerged as an independent discipline, distinct from the radiofrequency (RF) and millimeter-wave specialties both in its applications and technology. [6, 7]

Fascination with the THz regime is twofold: A wealth of interesting and useful physics occurs in what has historically proven to be the most inaccessible portion of the electromagnetic spectrum – the now-infamous "THz gap" that exists between the millimeter-wave and the far-infrared, as illustrated in Figure 1.2. [8]

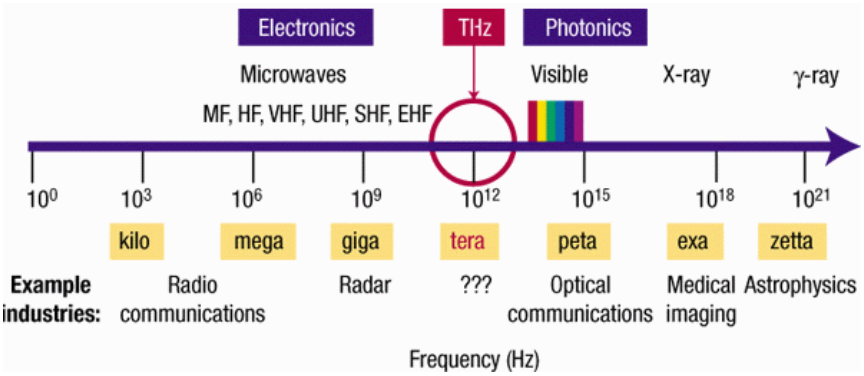

Figure 1.2: Electromagnetic spectrum showing the THz gap. Devices bridging the gap are divided into two classes: Bottom up (electronic) and top down (photonic).

The terahertz spectrum may be viewed with equal accuracy either as extremely high-frequency radio waves or extremely long-wavelength infrared light, and this is

reflected in the literature – authors with RF and/or millimeter-wave backgrounds refer to "sub-mm waves", while authors from the optical fields instead refer to "far-infrared light". Figure 1.2 illustrates two qualitative categories used to classify the efforts to develop new sources of THz radiation. The "bottom-up" category labels efforts to *increase the operating frequency* of electronic devices, while "top-down" approaches seek to *increase the operational wavelength* (or equivalently, to decrease the operational frequency) of photonic devices. [8, 9]

As will be discussed below, the "bottom-up" and the "top-down" approaches both encounter serious performance issues within the "THz gap". Objective evaluation of the efficacy of different THz sources requires a specific and consistent definition of the term "terahertz". Variation of this definition within the literature seems confusing, since some authors define "terahertz" as 0.1 – 10 THz, while others define "terahertz" as 0.3 – 3.0 THz. In general, the difference in the definitions of "terahertz" arises from the authors' backgrounds. Authors from the *photonic* field tend to use the wider definition, and authors from the *electronic* field prefer the narrower definition.

We adopt the narrower definition of the terahertz range based on the relationship between the wavelength λ and frequency f of an electromagnetic wave:

$$\lambda f = c, \tag{1.1}$$

where c is the speed of light in vacuum. Equation (1.1) in standard SI units shows that the wavelength of a 0.3 THz wave is exactly one millimeter (mm). Thus 0.3 THz is the logical lower boundary dividing millimeter-wave from THz. Similarly, 3.0 THz corresponds to a wavelength of 100 micrometers (μm), which falls approximately in the middle of the far-infrared range. Irrespective of how "terahertz" is defined, there is broad multi-disciplinary agreement that improved terahertz technol-

ogy represents a compelling advancement opportunity due to the fact that certain physical mechanisms occur *only* within the THz regime, as illustrated in Figure 1.3. [10, 11, 12, 13, 14]

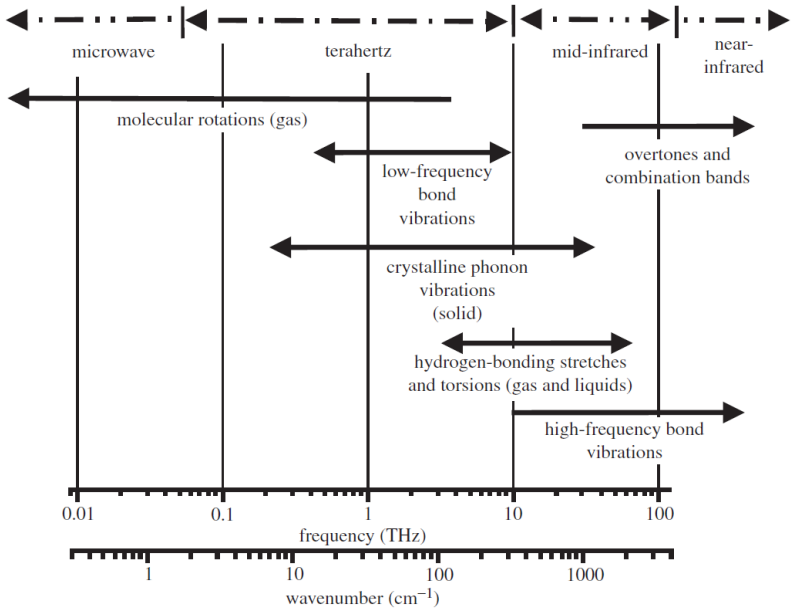

Figure 1.3: Frequency ranges of physical processes unique to the terahertz.

As an example of how terahertz can create compelling new technological applications, we consider an important industrial mainstay application – spectroscopy. The interaction of electromagnetic radiation with matter is usually modeled as an incoming wave of known physical characteristics – frequency, intensity, direction and phase. The electromagnetic wave interacts with matter through the physical mechanisms of absorption, reflection, and refraction. The radiation-matter interaction creates an outgoing wave (or multiple outgoing waves) with different physical characteristics. A detailed model of the material under consideration allows calculation

of its response to radiation across different wavelengths (*i.e.* its spectrum). In many practical applications, however, the physical properties of a sample of a material under consideration are not known, and therefore the spectrum of the material is collected, allowing the radiation-matter calcluation to be "worked backward" in order to determine information about the physical state of the sample. Empirical spectral data collection (spectroscopy) is perhaps one of the most pervasive modern technical applications used in modern manufacturing.

Fourier transform infrared spectroscopy (FTIR) is a particularly effective technique – especially in the mid- and near-infrared (IR). FTIR hardware is based on the Michelson interferometer developed in 1907, although Michelson never performed spectroscopy. The two most critical parts of the mechanism are the IR source and the mirror drive. Once the technique was successfully demonstrated, its usefulness was quickly realized by workers in the physics, chemistry, and engineering disciplines.

Performing FTIR (and spectroscopy in general) is highly challenging from a technical perspective, and it was only the *commercialization* of spectroscopy that quickly moved it from a *scientific endeavor* to a *technical application.* [15] Commercial FTIR tools have been available for decades and are now indispensible to numerous industries. In fact, the most important modern industries – food processing, pharmaceuticals, and semiconductors to name a few – literally could not operate manufacturing facilites without automated spectroscopy tools. Modern FTIR systems utilize highly-controlled IR sources, robots, computers, and optimized calculation algorithms. This level of automation allows a manufacturing technician to quickly collect accurate FTIR data without assistance from an engineer or scientist.

Terahertz pulsed spectroscopy (TPS) is but one example of how discovering the limitations of a well-established technique like FTIR leads to the development of a new terahertz application. History suggests that terahertz technology may transform

twenty-first century industrial manufacturing in the same way that IR and Raman spectroscopy helped revolutionize twentieth century manufacturing.

TPS is a new technique that has recently been demonstrated as a practical and particularly effective chemical analysis methodology which significantly outperforms state-of-the-art FTIR systems in terms of sensitivity and repeatability. TPS could potentially allow the pharmaceutical industry to move away from its current *batch processing scheme* required by United States federal law to the *continuous processing scheme* employed in many other industries – for example, the semiconductor industry.

Batch processing presents an "all-or-nothing" approach to manufacturing – first an entire production line is dedicated to producing a quantity of finished goods, then the quality of the whole batch is tested. If the quality checks fail, then the *entire* batch is scrapped. Continuous processing allows for nearly real-time detection of discrepant product, thus mimimizing the financial impact of scrap material.

The development of TPS not only shows how a new terahertz application addresses the known limitations of the established approach, it shows how the terahertz application can create new capabilities. In many cases the terahertz approach delivers a simpler and more streamlined technical solution, as is the case with TPS – *using only a few microwatts (uW) of radiated THz power.* [10]

Terahertz pulsed spectroscopy is an example of a *broadband* application in which a powerful femtosecond laser excites a semiconductor photoconductive THz antenna made of gallium arsenide (GaAs) to generate a wideband THz signal covering the majority of the frequency spectrum between 0.3 – 3.0 THz with each laser pulse. The use of the laser-semiconductor antenna THz generation scheme increases the THz signal enough to eliminate the liquid-helium-cooled detectors required in far-infrared FTIR systems. The reduction of system complexity that TPS affords allows it to be put into a full production environment. State of the art for terahertz sources covers

a broad spectrum of disciplines. [16, 17] In order to identify the correct context in which to evaluate the performance of the proposed device, we next review the current status of the field.

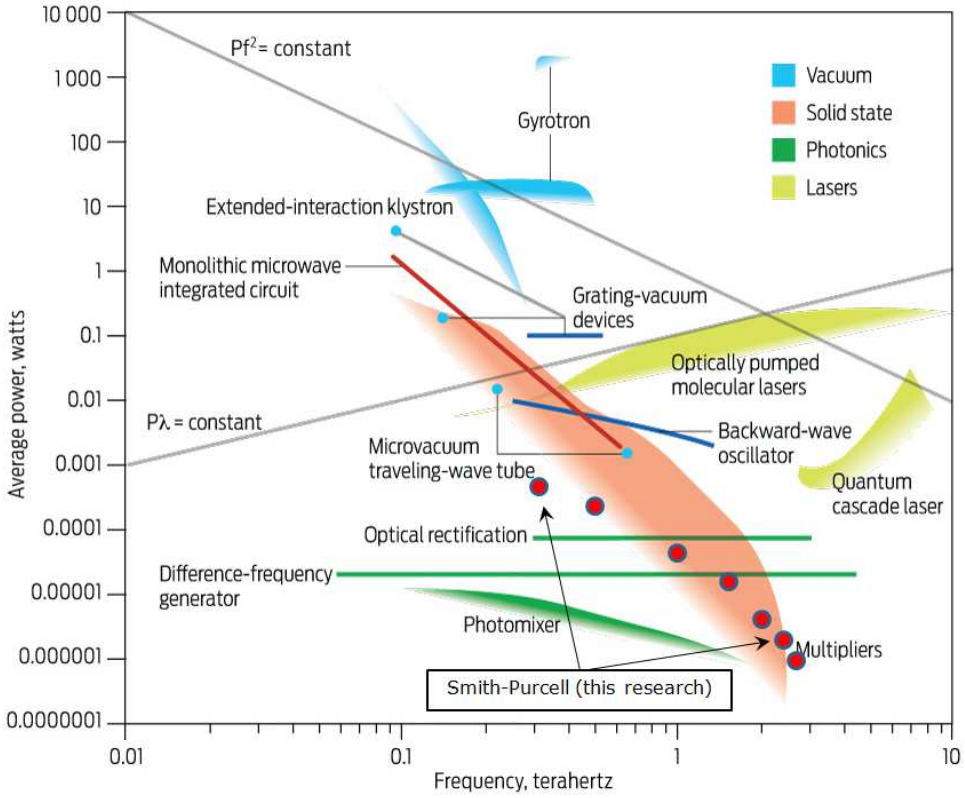

Figure 1.4: This research compared to all other THz sources.

1.2 Current State of the Art for THz Sources

Figure 1.4 [18] illustrates the power-frequency map of the many types of available terahertz sources – the performance range spans two orders of magnitude in frequency and *ten* orders of magnitude in power. In general, vacuum devices yield high power and lasers yield high frequency, which provides clear guidance as to what approaches

would be best-suited for applications tailored to these regimes. The situation becomes more complex below 10μW and above 0.1 THz due to the existence of multiple THz sources currently capable of delivering enough power at the required frequency, as illustrated in Figure 1.5. [19]

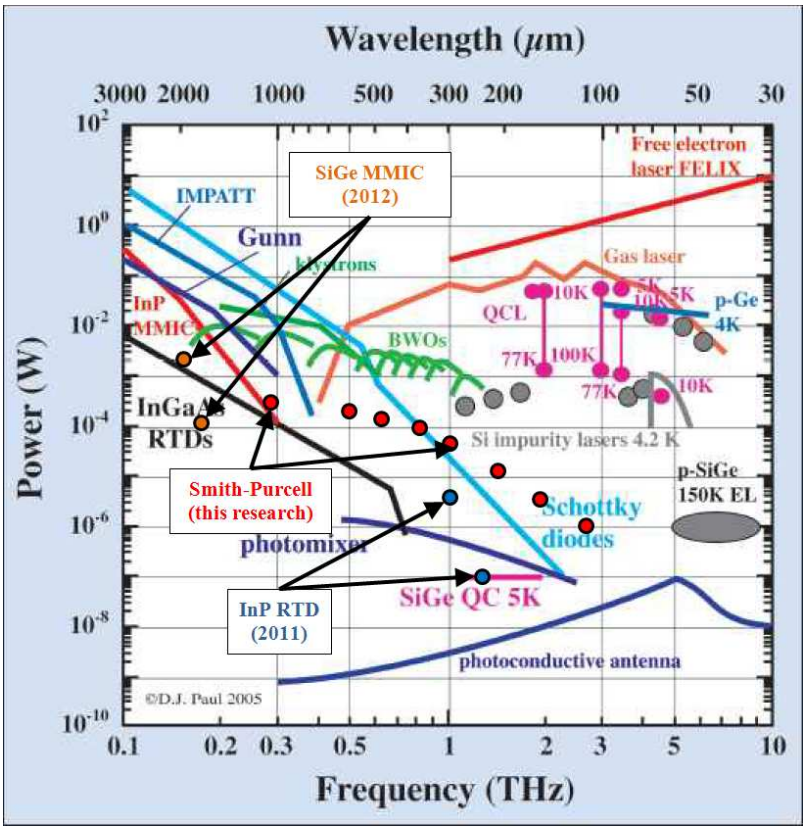

Figure 1.5: This research compared to other semiconductor THz sources.

The above example of how terahertz pulsed spectroscopy evolved from FTIR showed how compelling technological applications exist at the lowest THz power levels and that the attractiveness of a given solution depends on more than just the output of the radiation source. For instance, a THz source that can only operate at

liquid-helium temperatures adds tremendous cost and complexity to any system in which it is used. Similarly, an expensive THz source cannot successfully be implemented in a low-cost application – the important criteria of cost and complexity will be discussed in more detail below.

This research focuses on a novel *semiconductor* THz source, therefore it is appropriate to summarize the current status of other existing THz semiconductor sources. Many semiconductor textbooks present a reasonably complete taxonomy of the many specialized high-frequency electronic devices that have been developed over the last several decades. Sze [20] in particular provides details of the physical operation of each device. The majority of these devices are under active scrutiny to determine their applicability in millimeter-wave and THz applications.

As can be seen in Figure 1.5, the majority of semiconductor sources are of the "bottom-up" type discussed above, with the notable exception of the quantum cascade laser (QCL). The QCL is an important optoelectronic semiconductor device that was developed at Bell Laboratories in the 1990's, first being demonstrated in 1994 by the research groups of Capasso and Cho. QCL technology matured quickly and was already commercially available by 2002. [21] The QCL differs from the laser-pumped photoconductive THz antennas discussed above in that the QCL is an intrisically *narrowband* device – it is a laser. The QCL utilizes a complex stack of deposited films to achieve its operation, as shown in Figure 1.6. [22] In the past decade, the main thrusts of QCL research have been to lower its operational frequency while increasing its operating temperature. [23, 24, 25, 26]

The majority of QCL development to date has been done completely with III-V compound semiconductor systems, such as gallium arsenide (GaAs), indium phosphide (InP), and their alloys. As will be discussed in detail below, established compound semiconductors have a direct bandgap which imbues them with several highly

desirable device properties. However, compound semiconductor processing represents a *much* more expensive solution than silicon processing, for several reasons.

Much of the excess cost associated with compound semiconductors has to do with the substrate (or wafer) upon which devices are fabricated. The process to grow large-diameter, high-quality silicon ingots is very mature and well-established. Additionally, large (200mm and above) silicon wafers are mechanically robust and can be used in high volume with typical breakage yield well in excess of 97%. By way of reference, state of the art substrate diameters for GaAs and InP are 150mm and 100mm, respectively. Additionally, the cost of an individual semiconductor device is reduced as the *inverse square* of the substrate diameter, so for practical applications there is a large advantage to develop a THz device on a silicon substrate.

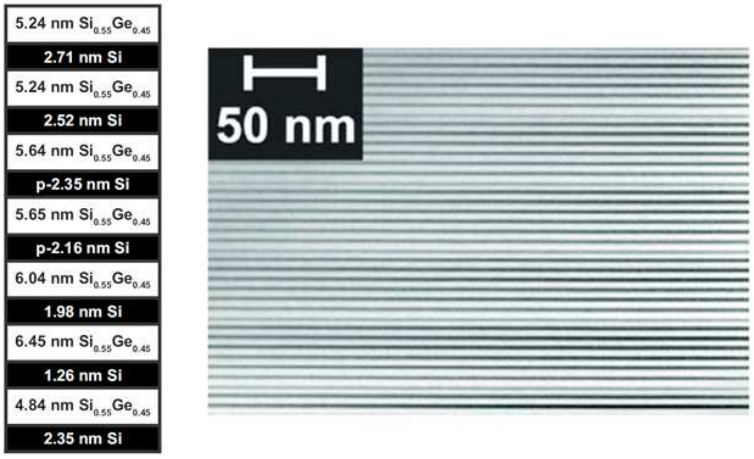

Figure 1.6: Film stack schematic and corresponding cross-sectional micrograph of a QCL active stack.

It is precisely for these reasons that recent efforts have intensely focused on QCL development within the silicon and silicon-germanium (SiGe) materials system. To

date, THz emission has been achieved, but not a functional laser. [22] The QCL has revolutionized the commercial availability of off-the-shelf semiconductor THz sources while illustrating the desirability of an approach that can leverage existing silicon-processing infrastructure. In this respect, it is more likely that one of the "bottom-up" approaches will yield a working THz device on a silicon substrate – although a different optical semiconductor holds a potentially important clue as to what the future may hold for hybrid silicon-compound semiconductor devices.

Widegap semiconductors have received intense research focus in order to enable new high-frequency and high-power semiconductor devices, but have also been demonstrated to be highly useful in the development of state of the art light emitting diode (LED) technology. One of the more promising LED materials, gallium nitride (GaN) comes from the "three-nitride" (III-N) family of compound semiconductors which are expected to enable several new semiconductor THz device technologies. GaN has been identified as a desirable semiconductor material for several years, and has begun to achieve some level of practical maturity. [27, 28]

The above-mentioned Gunn diode has a performance trend in Figure 1.5 showing its high power in the $0.1-0.3$ THz range. III-N materials are particularly exciting for high-frequency devices due to their high electron velocity, and in fact the investigation of an indium nitride (InN) Gunn diode forms the basis of a large portion of this research. Recently, investigation has begun into what specific challenges must be overcome to develop working III-N Gunn diodes. [29, 30, 31, 32]

The widespread interest in silicon-compound semiconductor systems has spurred the development of commercially available process technologies. One approach uses crystalline rare-earth oxides (REO) as an intermediate lattice-matching layer to enable full-wafer deposition of compound semiconductors on silicon, and recently 200mm GaN-on-Si process tools have been offered commercially. [33, 34] A different

approach has been developed in which lattice-mismatch defectivity is managed by epitaxial overgrowth on a pattern of oxide trenches on a silicon substrate. [35, 36] These techniques may prove to be fruitful as selective epitaxial growth has been for SiGe in mainstream silicon processing.

Silicon-germanium alloys have been crucial in the past two decades to enable ever-higher frequency operation of bipolar-complimentary-metal-oxide-silicon (BiCMOS) circuits. The primary semiconductor device in mainstream high-frequency BiCMOS integrated circuits (IC's) today is the heterojunction bipolar transistor (HBT). Typical epitaxial crystal growth is performed over the entire surface of a substrate. The SiGe crystal lattice is larger than a silicon lattice, and the strain of the larger SiGe lattice allows higher frequency HBT operation than using pure silicon – but potentially inducing large numbers of lattice defects and destroying HBT function.

Therefore modern HBT devices rely on *selective* epitaxial growth of the silicon-germanium (SiGe) alloy onto only small areas of the substrate where actual devices will be fabricated. Additional improvements in process technology have been crucial to increasing HBT operational frequency. In typical usage, the HBT is a room-temperature device, but as is common with most semiconductor devices, performance is enhanced at lower temperatures. Recently an operational SiGe HBT was reported at 0.5 THz at liquid-helium temperature. [37] The most typical use of HBTs's, however, is not as a discrete standalone element, but as part of an integrated circuit operated at room temperature.

The optical and millimeter-wave disciplines face distinctly different challenges based on their respective operational wavelengths. Recent advances in millimeter-wave imaging highlight the immense advantages that a *terahertz integrated circuit* operating in pulsed mode could provide – real-time, three-dimensional materials imaging. [38] Current state of the art in the high-speed IC field is the millimeter-wave

integrated circuit (MMIC). For the last 20 years, only compound semiconductors could achieve the speed necessary to fabricate working MMIC's. Initially, MMIC's were only fabricated in GaAs, but the advent of InP process maturity and the inherently higher electron velocity that InP provides has made it the MMIC material of choice for the highest-speed devices, as can be seen in Figure 1.5.

The automotive industry provided a "killer application" that has begun to fundamentally change this situation – automotive radar. Radar safety systems have been available for many years as an expensive option on top-end luxury cars. The primary reason for the relative inaccessability of these features was due to the complexity and expense of the GaAs devices comprising the systems. It was the cost advantages in the marketplace that drove the extension of SiGe BiCMOS MMIC technology to reach the 77GHz frequency and above. This achievement has led to the expectation that *multiple* SiGe-based radar safety features will be widely available on all cars within the next 3 years. Consequently, the performance of SiGe-based MMIC's have begun to approach InP MMIC's, as indicated by the overlay in Figure 1.5. Discussion of circuit-design principles is beyond the scope of this discussion. Therefore it is sufficient to note that the success of SiGe MMIC's in automotive radar systems lies as much in the availability of integrated support devices on the MMIC to enable the complex circuit designs necessary to implement two-way radar communications. [39, 40]

In much the same way that radar provided the impetus to move millimeter-wave integrated circuits into the mainstream with silicon-based process technology, it is expected that *wireless communication* will help drive the development of affordable THz integrated circuits. As illustrated in the detailed spectroscopy example above, applications require a *system* solution, not necessarily just one improved component. In the case of THz communications, there are a number of technical issues beyond

just transmitting power that must be addressed before any potential solutions become available. [41] Therefore in wireless communications, as for many other new THz applications, the "holy grail" would be a room-temperature integrated circuit technology capable of supporting multiple designs that deliver usable power level across the $0.3 - 3.0$ THz range.

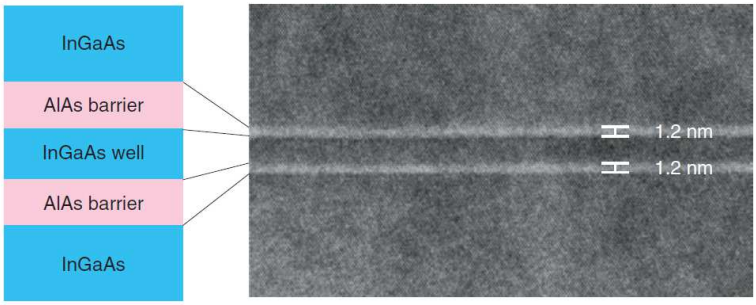

Figure 1.7: Hyper-abrupt epitaxy used to fabricate a working 1.04 THz resonant tunneling diode (RTD).

The resonant-tunneling diode (RTD) represents current state-of-the-art for InP-based semiconductor THz device technology, with recent reports of fundamental oscillations in the THz range. This is one of the more compelling THz semiconductor devices to date with demonstrated output power of 7μW at 1.04THz. The device uses standard monolithic process technology and allows for an integrated slot antenna to boost output power. [42] The THz RTD requires hyper-abrupt epitaxial growth to achieve its performance, as shown in Figure 1.7. [43] This is a much simpler process than is required to fabricate the complex film stack necessary for QCL's.

Underscoring the feasibility of the migration to a "hybrid theory" of silicon-compound semiconductor integration, a working InP-based RTD was recently re-

ported in which the RTD was fabricated on a silicon substrate as shown in Figure 1.8. [44] The silicon semiconductor industry has realized the difficulties that silicon faces at advanced technology nodes, and has researched the integration of III-V materials into standard process flows for a number of years. The SEMATECH consortium recently reported the successful fabrication of 50nm InGaAs transistors on a 200mm silicon substrate compatible with modern state-of-the-art silicon processing using a GaAs buffer layer. [45] Selective epitaxy of InP on silicon is showing promise at the research phase for developing working diode lasers with integrated waveguides. [46]

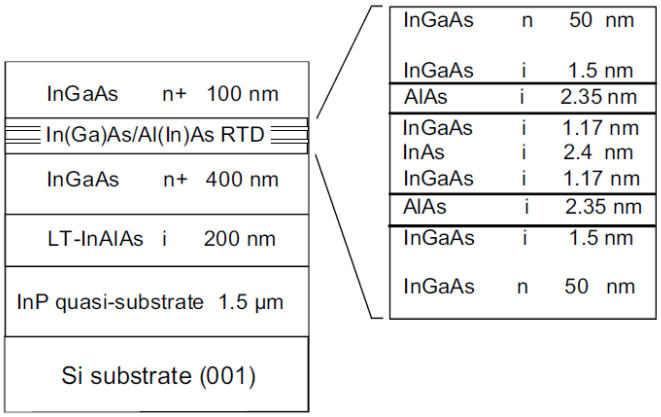

Figure 1.8: Film stack to fabricate a working InP-based RTD on a silicon substrate.

This introduction has set the context for the current research by capturing some of the major trends and relevant ideas for state-of-the-art THz semiconductor devices:

1. Widegap materials → higher electron velocities → higher frequency
2. Integrated circuits → higher integration → more powerful solutions
3. Silicon substrates → more devices per wafer → lower cost

4. Simpler processes → higher yield → lower cost

The Smith-Purcell Semiconductor THz Source is specifically designed to integrate into a silicon-based integrated circuit technology in a very straightforward and simple manner, using the techniques referenced in this Introduction. This device may provide a realistic path to useful THz integrated circuits that can be used in many emerging application spaces. For the purposes of discussion of the methods and results of this research, we next provide some background on the two primary physical phenomena utilized by the device and how their joint application provides a viable solution to the problem of the compact semiconductor THz source.

1.3 Smith-Purcell Radiation

The Smith-Purcell effect was first hypothesized and observed as a *vacuum electronic* effect. The nature of Smith-Purcell radiation (SPR) depends on the manner in which electrons interact with the grating. Weak, *incoherent* radiation known as *spontaneous SPR* is produced when single electrons randomly interact with a metallic diffraction grating – this is the type of SPR originally obeserved by Smith and Purcell. They observed that the wavelength λ' of the radiated light in their experiments depended on the reduced electron velocity $\beta = v/c$, observation angle θ, and grating period P according to:

$$\lambda'_{SPR} = P\,[\,\beta^{-1} - \cos\theta\,] \tag{1.2}$$

Here the prime indicates the case of relativistic electrons to distinguish it from the non-relativistic case to be considered in detail below. Issues such as imperfect vacuum and dense-beam electron optics are practical considerations for electron beam devices, but relativistic beams are routinely used in high-power SPR applications. [47, 48] In

fact, relativistic SPR is one of the primary focus areas of modern research. [49, 50]

Experimental SPR studies indicate that radiated power P_{SPR} varies with the distance between the charges and the grating b (called the *impact parameter*), the number of charges N, and the velocity of the charges v as:

$$P_{SPR} = CN^2v^4 \exp^{-\alpha b} \tag{1.3}$$

Equation (1.3) represents C and α as constants for clarity, but in reality they are complicated functions related to the specifics of a given experimental setup. To maximize SPR power, tradeoffs must be made among conflicting requirements. The impact parameter must be minimized while the number of charges and their velocity are maximized. This situation must be maintained over the largest possible distance. Electron beam focusing poses significant challenges to vacuum Smith-Purcell devices. Space-charge repulsion within a highly-focused electron beam tends to push the beam apart. Thus the distance over which the beam interacts optimally with the grating is limited to some characteristic distance around the beam waist. [51]

The typical minimum impact parameter in a high-power vacuum device is of the order of hundreds or thousands of microns. In contrast to vacuum devices, typical separation between the gate electrode and the conduction electrons in modern silicon transistors is of order 10Å. In high-power semiconductor devices, the gate dielectric may be a few hundred angstroms thick. This is several orders of magnitude smaller than the impact parameter associated with vacuum devices. As will be discussed in more detail below, it is precisely this very small impact parameter that allows the Smith-Purcell effect to be seriously considered as a viable radiation mechanism for a semiconductor device.

Quantitative theoretical calculation of SPR power proved to be much more dif-

ficult than experimental production of SPR devices. In 1961, Ishiguro and Tako performed early experiments on SPR wavelength and power. As a physical model of the radiation mechanism, they calculated the Larmor power of an oscillating dipole with moment perpendicular to the grating plane. Their experiments did confirm Smith and Purcell's wavelength dependence in Equation (1.2), but the SPR power they observed was much lower than their theoretical prediction. [52] The "blinking electric dipole" utilized by Ishiguro and Tako has subsequently appeared as one of the most common simplified physical SPR models to appear in the literature. *It is worthwhile to note that the blinking-dipole model of SPR immediately predicts that radiation intensity will be minimum in the direction normal to the grating plane.*

In 1960, Giuliano Toraldo diFrancia proposed an SPR theory in which the field of a uniformly moving electron is expanded into a set of evancescent basis waves that independently interact with the grating. Once each wave has interacted with the grating, superposition of the set of outgoing waves are found to contain *real* propagating waves that correspond to observed SPR. [53] The diFrancia theory was notoriously difficult to use for practical calculations, and therefore was not amenable to direct confirmation.

Thirteen years later, Peter van den Berg later expanded diFrancia's theory and was able to solve the specific case of a sinusoidal grating, both for a point charge and a line charge. [54, 55] To underscore the difficulty of the evanescent-wave theory of spontaneous SPR, even van den Berg's more specific calculations were not experimentally confirmed until until 1997 by Goldstein and Walsh – nearly *40 years after diFrancia's initial publication*! [51]

In contrast to the spontaneous SPR produced by a DC electron beam in proximity to a diffraction grating, if the vacuum electron beam can be bunched tightly enough in a self-consistent manner, then all electrons in each bunch are observed to radiate

coherently. This much stronger version of the Smith-Purcell effect is called *stimulated SPR*, and it the physical radiation mechanism used in certain types of free-electron lasers. In fact, the first high-power Smith-Purcell device – called the orotron – first introduced by Rusin in 1965 was later shown to be the first free-electron laser. [56] The Smith-Purcell semiconductor THz source described in this work can conceptually be considered as a 'solid-state orotron', although the detailed operation of the devices differ radically since the orotron is a vacuum device, as will be discussed in detail below.

In the orotron, an initally DC electron beam creates *spontaneous* (single-charge) SPR that feeds a resonant mode of the device. The resonant cavity mode bunches the electron beam and generates *stimulated* (many-charge) SPR. In free-electron laser terminology, the transition from spontaneous to stimulated SPR is when the device begins to lase. Stimulated SPR power varies as the square of the number of charges in the bunch and as the fourth power of the bunch velocity. Modern pulsed orotrons are reported to generate 60mW pulsed power at 0.36THz. [57, 58, 59] Smaller vacuum-electronic Smith-Purcell devices have been reported in which a grating is inserted into the electron beam column of a modified scanning electron microscope (SEM), and experimental studies of Smith-Purcell radiation have been performed using this method. [60, 61]

In order to observe SPR, the charge carriers need to be moving at constant velocity for a distance comparable with one grating period. For electrons in vacuum this is not an issue since the electron conduction is collisionless, and electrons in vacuum experience what is known as *ballistic transport* (motion without collisions). The velocity of the electrons in a vacuum beam travelling between two charged plates without collisions is limited only by the electric potential that can be held between the electrodes. This is why relativistic devices can readily be built within the vacuum

electronics disciplines.

In a semiconductor device, however, it is the electrical conduction current of charge carriers (electrons and/or holes) which must play the physical analog of the electron beam in a vacuum SPR device. As charge carriers in a crystalline material attempt to respond to the influence of an externally-applied electric field, they encounter an extremely high collision rate. Crystal defects, intentionally-introduced impurities (dopants), and vibrations of the crystal lattice (phonons) can all interact with charge carriers in the form of scattering events (collisions). These collisions prevent charge carriers from being accelerated to arbitrarily high velocities, no matter how high the applied electric field. Typically the maximum charge-carrier velocity is referred to as the *drift velocity*. Thus the very nature of electrical conduction in semiconductors provides two immediate challenges for SPR in semiconductors – mean free path (average distance the carrier moves between collisions) and the finite *drift velocity* that results.

One of the key properties used to describe semiconductors is its *mobility* (generally denoted by μ), the definition of which characterizes the complex collision physics at microscopic scale as a proportionality between the drift velocity v_d and the applied electric field E:

$$v_d = \mu E, \tag{1.4}$$

The mobility μ is in general a complex function of electric field, temperature, doping concentration, and other variables. All semiconductors display a maximum drift velocity at extremely high applied electric field. This is referred to as the *saturation velocity*, and will be dicussed in more detail in the next section. Typical semiconductor saturation velocity is on the order of 10^5 m/s, which is three orders of magnitude slower than that of relativistic electrons. Thus in the remainder of this work we only

consider the non-relativistic case of Smith-Purcell radiation.

The non-relativistic Smith-Purcell relationship between radiation wavelength and electron velocity given in Equation (1.2) simplifies to a directionally-isotropic scenario described by:

$$\lambda_{SPR} = \frac{c}{f}, \tag{1.5}$$

where the frequency f of the radiation is the same as given in Figure 1.1, namely the ratio of the electron velocity v to the grating period P:

$$f = \frac{v}{P} \tag{1.6}$$

With drift velocity of order of 10^5 m/s, Equation (1.6) shows that mm-wave and THz frequencies can be readily achieved with micron and sub-micron grating periods, provided that uninterrupted carrier motion in the semiconductor could be arranged. Unfortunately, electron mean free path decreases dramatically with temperature in semiconductors due to increased thermal lattice vibration (phonon activation)Worse yet, doping the semiconductor (to improve its current-carrying ability) also dramatically reduces mean free path due to the charge carriers being scattered off the doping impurities. These considerations imply that in order to observe spontaneous SPR in semiconductors, very pure samples at low temperatures must be used. The literature of SPR from solid-state devices – specifically SPR from semconductors – is very small when compared to the extensive body of literature for SPR from vacuum devices. Gornik investigated spontaneous SPR from cryogenic semiconductor samples; the observed power was indeed very small. [62]

Since SPR power varies as the fourth power of velocity, any spontaneous SPR power from semiconductors is simply too weak to be able to bunch the conduction

current in a semiconductor sample and generate stimulated SPR. Gornik's experiments also confirmed that only very pure semiconductors at cryogenic temperatures were able to produce any SPR. Therefore it is clear that the propsect of room-temperature stimulated SPR from a semiconductor is indeed bleak without some sort of additional physics available to overcome the serious obstacles observed by Gornik. Fortunately, nature has provided a very simple method for automatically "bunching" the conduction current in many semiconductor materials – at room temperature and for highly-doped samples. This, of course, is precisely the primary characteristic of the transferred electron (or Gunn) effect.

1.4 Transferred Electron (Gunn) Effect

The transferred electron effect makes it possible to consider room temperature generation of stimulated SPR from a semiconductor device. As noted above, the transferred electron effect was independently predicted in theoretical works by Ridley and Watkins and by Hilsum. The first experimental observations of the effect were reported by Gunn, which is why the effect also bears his name. Ironically, the end goal that drove the discovery of the transferred electron effect was none other than *the development of a high-power terahertz source – over 50 years ago.*

In the late 1950's, Kroemer noted that the energy band structure of certain semiconductors predicted conditions under which charge carriers could display *negative effective mass* along certain preferred crystal axes as shown in Figure 1.9. Kroemer proposed that charge carriers in germanium samples subjected to high magnetic fields would be forced near the edges of the energy band, where their effective masses in crossed electric and magnetic fields would have anisotropic components – and that at least one of these effective mass values would be negative. Kroemer's primary physical requirement was that the charge carrier have enough kinetic energy to reach

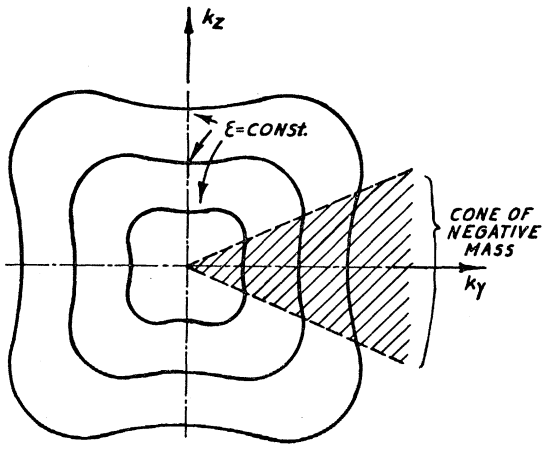

Figure 1.9: Re-entrant energy band structure of germanium showing region of negative effective mass.

the band edge, where it would experience negative effective mass. Typically the kinetic energy of charge carriers is increased by applying an external electric field to the semiconductor crystal. [63]

The charge carriers are thus said to be "heated" by the electric field because their velocity (and therefore their kinetic energy) is increased according to Equation (1.4). Kroemer predicted that "hot carrier" effects would lead to the novel macroscopic observation of *bulk negative resistivity*, in which the resistance of the semiconductor would *decrease* in response to an *increasing* electric field. He proposed that negative resistance in semiconductors would enable the design and fabrication of high-frequency amplifiers operating into the terahertz (THz) frequency range by placing the highly-biased semiconductor crystal into a resonant cavity. The initial experiments to observe this effect were not successful, but the approach was later shown to work, and in fact high-power THz sources for use in astrophysical research are based on Kroemer's approach using high magnetic and electric fields. [64]

In 1961, parallel work by Hilsum and the team of Ridley and Watkins proposed

a theoretical alternative to Kroemer's negative-effective-mass approach to attaining negative resistance in semiconductors. Instead of attempting to determine the conditions under which *bulk negative resistivity* could be attained, they instead realized that if the energy band structure of a semiconductor contained *two different effective mass bands*, then it might be possible to populate the higher-energy (and higher effective mass) band with "hot" carriers. They showed that as long as the hot carriers could tunnel into the higher-mass band and not decay back to the lower-energy band too quickly, then *bulk negative differential resistance* (NDR) would be displayed in the material.

In what is now called *Ridley-Watkins-Hilsum theory*, semiconductor NDR manifests as a change in curvature of the conduction current versus applied electric field plot. Figure 1.10 from Hilsum's original paper demonstrates both the higher-mass "satellite" energy bands found in gallium arsenide (GaAs) as well as the predicted current-field relationship with the onset of NDR occurring at an applied field of approximately 3 kv/cm. [2] Both authors noted that at the onset of NDR the voltage-current (VI) characteristic of the material would contain a fundamental instability that could potentially prove useful for high-frequency device applications. They predicted that the nature of this instability would lead to the observation of high-electric-field "domains" that would freely travel through the material.

As hot carriers populate the high-field satellite valley, their effective mass increases and their drift velocity drops since the "heavy" carriers move more slowly at the same applied field. As a result of carrier accumulation, a space-charge dipole boundary layer can detach from one electrode of the sample and freely propagate through its length. The electric field in the vicinity of the dipole layer is typically much higher than the electric field in the remainder of the device, and can be quite narrow in the direction of propagation.

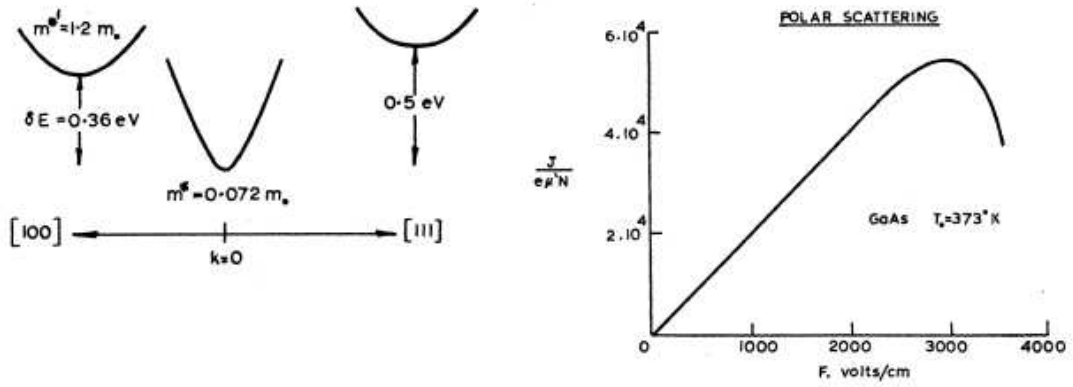

Figure 1.10: (left) Band structure of gallium arsenide (GaAs) showing the high-effective-mass "satellite valleys" available to hot carriers. (right) Calculated current-field plot predicting NDR at approximately 3kv/cm.

As mentioned above, J. B. Gunn experimentally investigated the properties of high-field conduction current in gallium arsenide (GaAs) in 1964. He observed the spontaneous transition of GaAs conduction current from DC to RF at about 3kV/cm, as predicted by Ridley-Watkins-Hilsum theory. Gunn's observation led to a rush of experimental work on the phenomenon which came to be named after him. It was finally Kroemer who provided the key insights necessary to definitively show that the various experimental "Gunn-like" experimental phenomena were inclusively described by the Ridley-Watkins-Hilsum theory of the transferred-electron effect. [65]

The transferred-electron effect found almost immediate widespread attention as a method of easily building high-frequency, high-power electronic devices. Therefore the literature contains many references concerning the theory, modeling, and fabrication of novel devices and analysis methods. In order to effectively apply the transferred-electron effect to practical devices, the size, shape, and speed of the high-field domains that are produced at the onset of NDR must be controlled.

Butcher, Fawcett and Hilsum published a particularly useful method for calculating fully-formed domain shapes. The method was so successful that today it is the standard analysis presented in semiconductor textbooks. The Butcher-Fawcett-Hilsum domain calculation method is commonly referred to as the "equal-areas method". In most cases, the domain shapes easily calculated by this semi-analytic method agree very well with much more detailed Monte Carlo calculations. The only inputs required to apply the equal-areas method are the relationship between drift velocity and applied electric field – the *v-E characteristic* and a value for the mobility in the material of interest. [66] The next section details how the method was implemented for this research.

The validity of the equal-areas method was experimentally verified shortly after its publication. As Gunn diodes were incorporated into practical applications, it was essential to establish solid connections between design (theory) and experiment. Gunn used a capacitive-probe technique to measure domain profiles under various experimental conditions. [67] Shoji later demonstrated that electrodes on the surface of Gunn diodes produced predictable current waveforms and enabled the experimental investigation of 2D domain dynamics. [68] Shoji's work demonstrated clearly that domains traveling under metallic surface electrodes induce image charge. [69, 70]

In this Introduction, it has been established that all aspects of Figure 1.1 have separately been experimentally investigated, and a thorough literature review shows *that this specific device has never previously been proposed or studied.* The next section provides an exposition of the theoretical methods and results used to perform this research. The theoretical methods are then applied to investigate the characteristics of the Smith-Purcell radiation generated from a metallic diffraction grating fabricated near the surface of a Gunn diode under various device conditions.

2. GUNN EFFECT

This research proposes the novel synthesis of two physical phenomena – the solid-state transferred-electron effect and the electrodynamic Smith-Purcell effect – to address the specific problem of generating terahertz (THz) radiation from a room-temperature semiconductor device. This section presents the methods used to theoretically analyze the performance of the proposed device, beginning with a brief review of the physics of the transferred-electron effect and its various practical manifestations.

The Butcher-Fawcett-Hilsum "equal-areas" method is then derived, which provides the means to calculate the detailed shape of a fully-formed dipole domain using only the velocity-field (v-E) characteristic and the mobility of a given semiconductor material. This method makes it possible to accurately calculate domain charge profiles for new semiconductor materials before device fabrication technology exists.

A first-principles derivation of non-relativistic Smith-Purcell radiation from a single charge follows, in the limit of very close charge-grating spacing appropriate to a semiconductor device. *It is found that the "blinking dipole" model commonly used in the literature of vacuum Smith-Purcell devices incorrectly predicts the radiative properties of the semiconductor device.*

Superposition allows the single-charge SPR result to be readily extended to an arbitrary charge distribution. Device performance is predicted by applying superposition of the single-charge SPR result to the charge distribution of a dipole domain. To close the section, the analytically calculated electic field from the device is compared to finite-element electromagnetic computer simulations of the device. Agreement

between the methods validates the theoretical analysis.

Gunn diodes can oscillate in several different modes, depending on their size and doping level. Of particular interest to this research is the *transit-time dipole-layer mode*, which requires that the diode be long enough *and* contain enough charge for the domain to fully form before it exits the device. In the literature these requirements for dipole domain formation in GaAs and InP are expressed as a minimum threshold value for the product of the doping level n_0 and length L of the device, namely:

$$n_0 L > 10^{12} cm^{-2} \text{ for dipole-layer mode oscillation} \tag{2.1}$$

Due to the intrinsic instability of a semiconductor at the onset of NDR, small fluctuations in conduction current lead to domain formation. Domain nucleation and growth are not directly observable for devices that are long compared with domain width, and the capacitive measurement technique is required to observe domain growth. [71] The domain quickly grows until it collects its maximum quantity of charge, after which it is called a *fully-formed* dipole domain. The fully-formed domain drifts at constant velocity through the the device with no change in shape.

Modeling of domain growth dynamics is typically done with Monte Carlo simulations tailored to specific experimental conditions. A recent theoretical analysis of gallium nitride (GaN) Gunn diodes including thermal effects illustrates some limitations of Monte Carlo and provides overview references. [30] Evaluation of the proposed Smith-Purcell THz source relative to other THz sources, however, only requires knowledge of the physical characteristics of the fully-formed dipole domain. For Smith-Purcell radiation, the important physical characteristics of the dipole domain are its velocity, peak charge density, and width. All these quantities are readily obtained from the equal-areas method.

2.1 Derivation of the Equal-Areas Condition

Butcher, Fawcett, and Hilsum developed the equal-areas method as a conceptually simple theoretical framework with which to accurately calculate the shape of a fully-formed dipole domain, given only a semiconductor's mobility and its velocity-field (v-E) characteristic. [72, 66] The equal-areas method is the main technique provided by modern semiconductor physics textbooks to analysis domain shapes. A brief review of the textbook derivation from Reference [20] is given, followed by confirmation of the numerical code written to implement the equal-areas method for use in this research.

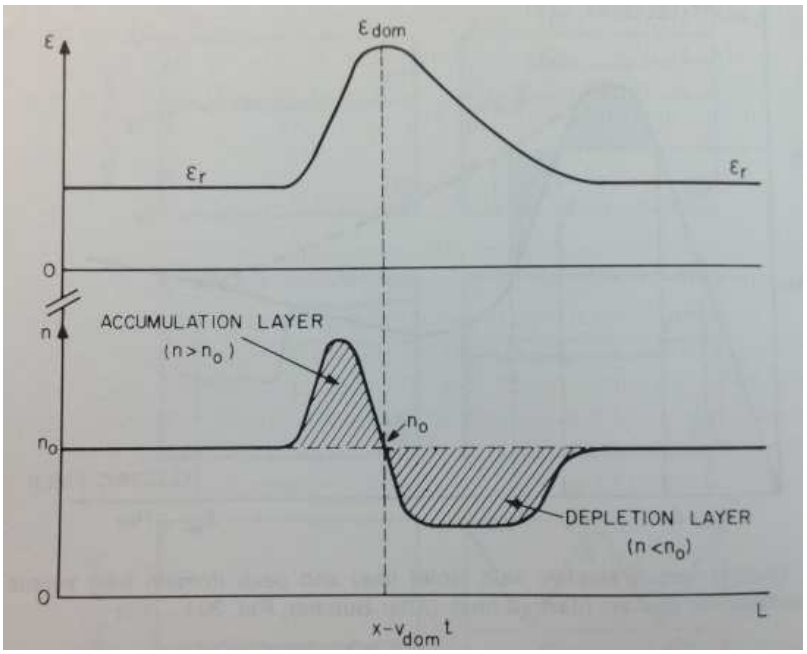

Figure 2.1: Electric field and electron distribution in a dipole domain.

A dipole domain is a region where the electric field E is greater than field in the remainder of the device E_r, as illustrated in Figure 2.1. [20] The electron con-

centration n is equal to the doping level n_0 outside the domain and at the point of maximum electric field E_{dom}. The "front half" of the domain is electron-depleted, while electrons accumulate in the "back half", showing the origin of the name *dipole domain*.

The goal of the equal-areas method is to determine the electric field E and electron concentration n as a function of position in the semiconductor by self-consistently solving Poisson's equation and the conservation of current density equation:

$$\nabla \cdot \boldsymbol{E} = \frac{\rho}{\epsilon} \tag{2.2}$$

$$\nabla \cdot \boldsymbol{J} = 0 \tag{2.3}$$

The first simplification is to write a *one-dimensional* theory by assuming that the electric field E points along the x axis, causing the electrons of charge q to drift in the positive x direction. This allows Poisson's equation to be rewritten in terms of the number of electrons n and number of ionized donors n_0 (the doping level) as:

$$\frac{\partial E}{\partial x} = \frac{q(n - n_0)}{\epsilon} \tag{2.4}$$

where the doping n_0 is assumed to be uniform throughout the length L of the device.

The total electron current density J is composed of contributions from conduction, diffusion, displacement currents. The conduction current is just the total charge qn times the known field-dependent electron velocity $v(E)$, which is a given input to the problem. The diffusion current is also a function of the electric field, since in general the electron diffusivity $D(E)$ is field dependent. Once the final differential equation for the problem is derived, the diffusivity will be replaced by the *diffusion constant*. Finally, the displacement current term (from Maxwell's equations) gives

the expression for total current:

$$J = qnv(E) + q\,\frac{\partial}{\partial x}\{D(E)n\} + \epsilon\,\frac{\partial E}{\partial t} \tag{2.5}$$

Since the domain is assumed to move through the semiconductor at constant velocity v_{dom} without changing shape, the next step is to transform to a coordinate system $y = x - v_{dom}t$ that moves with the domain. In this coordinate system, the electron concentration n is a double-valued function of the electric field E as seen in Figure 2.1 – for each value of E between E_r and E_{dom}, the accumulation and depletion regions of the domain have different values of n.

The chain rule allows Equations (2.4) and (2.5) to be to converted to the new coordinate system:

$$\frac{\partial f(y(x))}{\partial x} = \frac{\partial f}{\partial y}\frac{\partial y}{\partial x} \tag{2.6}$$

and since $y = x - v_{dom}t$,

$$\frac{\partial y}{\partial x} = 1 \tag{2.7}$$

$$\frac{\partial y}{\partial t} = -v_{dom} \tag{2.8}$$

therefore

$$\frac{\partial E}{\partial x} = \frac{dE}{dy} \tag{2.9}$$

$$\frac{\partial E}{\partial t} = -v_{dom}\frac{\partial E}{\partial y} \tag{2.10}$$

This allows Poisson's equation and the total current to be rewritten as:

$$\frac{dE}{dy} = \frac{q}{\epsilon}(n - n_0) \tag{2.11}$$

$$J = qnv(E) - q\frac{d}{dy}[D(E)n] - \epsilon v_{dom}\frac{dE}{dy} \tag{2.12}$$

Outside the domain, only the conduction current exists with value $J = qn_0v_r$, where $v_r = v(E_r)$ comes from the known v-E characteristic, as shown in Figure 2.2. Using this value for J and inserting Equation (2.11) into Equation (2.12):

$$qn_0v_r = qnv(E) - q\frac{d}{dy}[D(E)n] - qv_{dom}(n - n_0) \tag{2.13}$$

Dropping the common factor of q, rearranging and collecting terms gives

$$\frac{d}{dy}[D(E)n] = n(v(E) - v_{dom}) - n_0(v_r - v_{dom}) \tag{2.14}$$

This equation can be divided by Equation (2.11) to get a *single* differential equation describing the dipole domain:

$$\frac{q}{\epsilon}\frac{d}{dE}[D(E)n] = \frac{n(v(E) - v_{dom}) - n_0(v_r - v_{dom})}{n - n_0} \tag{2.15}$$

Numerical methods are required to solve the general case of Equation (2.15). Replacing the field-dependent diffusivity $D(E)$ with the normal *diffusion constant* D, however, significantly simplifies the solution. In practice, the diffusion constant D is taken to be proportional to the 300K low-field mobility:

$$D = \frac{\mu kT}{e} \tag{2.16}$$

The Boltzmann constant is $k = 8.617 \times 10^{-5}$ eV/K. Thus for the GaAs samples Butcher and Fawcett considered, the electron mobility and resulting diffusion constant from (2.16) are:

$$\mu = 6860 \frac{cm^2}{Vs} \rightarrow D = 177 \frac{cm^2}{sec} \tag{2.17}$$

Setting the diffusivity equal to the diffusion constant D yields a differential equation that describes the relationship between the electron concentration n and the electric field E:

$$\frac{qD}{\epsilon} \frac{dn}{dE} = \frac{n(v(E) - v_{dom}) - n_0(v_r - v_{dom})}{n - n_0} \tag{2.18}$$

Figure 2.1 shows the boundary conditions that the electric field E and electron concentration n must obey in order to properly satisfy Equation (2.18). In the two limiting cases of the electric field, $E = E_r$ and $E = E_{dom}$, the electron concentration n must equal the background doping $n = n_0$. Valid solutions of (2.18) give the electron concentration as a function of the electric field, $n(E)$. It is then necessary to convert $n(E)$ into the desired *spatial* description of the domain in terms of the moving spatial coordinate y. Once $n(E)$ is known, (2.11) can be converted into an integral equation defining the spatial relationship $E(y)$:

$$y = y_0 + \frac{\epsilon}{q} \int_{E_{dom}}^{E} \frac{dE'}{n - n_0} \tag{2.19}$$

where y_0 is an arbitrary integration constant corresponding to an offset in the definition of y. Once $E(y)$ is known, its derivative gives the electron concentration as a function of position $n(y)$ in accordance with Poisson's equation (2.11).

When D is constant, (2.18) has the formal transcendental solution:

$$\frac{n}{n_0} - \ln\left(\frac{n}{n_0}\right) - 1 = \frac{\epsilon}{qn_0D}\int_{E_r}^{E}\{[v(E') - v_{dom}] - \frac{n_0}{n}(v_r - v_{dom})\}dE' \qquad (2.20)$$

Applying boundary conditions to (2.20) illustrates the origin of the name 'equal-areas' rule. When either $E = E_r$ or $E = E_{dom}$, the boundary condition is that $n = n_0$. In both cases, the left-hand side of (2.20) is identically zero. Thus the integral on the right-hand side must also be zero. The case $E = E_r$ is trivially satisfied because the upper and lower limits of integration are the same. The maximum domain field case $E = E_{dom}$ is non-trivial and provides insight into the solution of the problem.

The integration from E_r to E_{dom} can be carried out in two ways – either over the accumulation or depletion region of the domain. Equation (2.20) must hold true even though n has different values in the depletion and accumulation regions of the domain. Specifically, the second term in the right-hand integral of (2.20) depends on n but must be equal to zero irrepsective of the value of n. This requirement can *only* be met if $v_{dom} = v_r$. Therefore the it is the boundary conditions that force solutions of the original differential equation (2.18) to obey the 'equal-areas' condition shown graphically in Figure 2.2:

$$\int_{E_r}^{E_{dom}}[v(E') - v_r]dE' = 0 \qquad (2.21)$$

The equal-areas method allows the peak domain field E_{dom} and the domain drift velocity v_r to be determined from the applied electric field E_r. As the applied field E_r is increased, the peak domain field E_{dom} increases strongly. The set of points (E_{dom}, v_r) determined by sequential application of the equal-areas condition is called the *dynamic characteristic* line of the device. The dynamic characteristic (shown

by the dashed line in Figure 2.2) shows that there exists a maximum domain field (or equivalently, minimum drift velocity) for stable dipole-mode operation. [20] The Gunn diode fails to operate in the dipole-domain mode at high applied fields that result in a drift velocity below the minimum supported value v_{rm}.

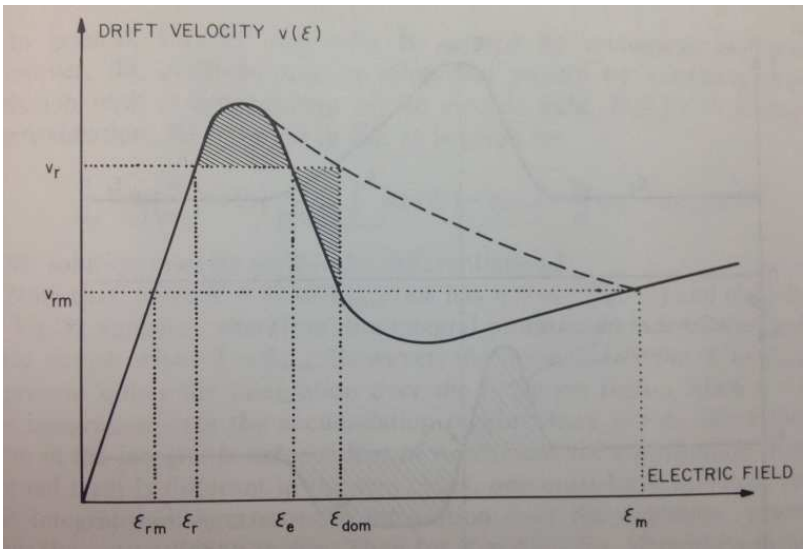

Figure 2.2: Solutions of (2.20) obeying the boundary conditions lead to (2.21), which requires the areas above and below the line $v = v_r$ to be equal.

Figure 2.2 shows that domains with higher peak field are physically wider and move more slowly than lower-field domains – *within the same physical device.* Thus the voltage tunability of the Gunn domain does not simply change just the domain velocity, it also changes the domain size and shape. This will be later seen to be a key consideration in the tradeoff between SPR frequency and power.

2.2 Verification of the Domain Calculation Code

The Butcher-Fawcett-Hilsum equal areas method of domain calculation requires a numerical solution of the set of equations (2.19), (2.20), (2.21), and (2.11). The simple form of these equations allows the method to be readily implemented in a straightforward manner. For this research, a Microsoft Excel® macro was sufficient to accurately calculate domain shape. This section demonstrates the accuracy of the equal-areas code by using it to reproduce Butcher and Fawcett's original results from the literature. Since the method requires a $v(E)$ characteristic as input, the code requires an analytic model at its starting point.

Shur's textbook provides an analytic model for the velocity-field characteristic of GaAs. [73] First the saturated electron drift velocity v_s and the saturation electric field F_s are calculated in Equations (2.22)) and (2.23). Then Equations (2.24) and (2.25) are used to determine fitting parameters A and t. Finally, the electron velocity as a function of electric field $v(E)$ is calculated using Equation (2.26).

$$v_s = 0.6 + 0.6\mu - 0.2\mu^2 \ (10^5 \mathrm{m/s}) \tag{2.22}$$

$$F_s = v_s/\mu \tag{2.23}$$

$$A = 0.6\left[e^{10(\mu-0.2)} + e^{-35(\mu-0.2)}\right]^{-1} + 0.01 \tag{2.24}$$

$$t = 4\left[1 + \frac{320}{\sinh(40\mu)}\right] \tag{2.25}$$

$$v(E) = v_s\left[1 + \frac{F/F_s - 1}{1 + A(F/F_s)^t}\right] \tag{2.26}$$

Shur's $v(E)$ model is the basis from which all domain shapes considered in this work are calculated. For materials other than GaAs, however, the saturation velocity, the saturation field, and the two fitting parameters were manually set instead of being calculated from Equations (2.22) through (2.25). This provided a means to accurately

match published $v(E)$ characteristics. The manual fitting technique allowed the same code to be used for all domain calculations.

The analytic $v(E)$ model also requires a value for the electron mobility μ as an input. Today it is more common to specify the bulk doping concentration n_0 of a sample instead of its mobility. Hilsum observed that a simple empirical relationship between the mobility and μ and n_0 was fairly accurate over several orders of magnitude. [74] Hilsum's relationship depends only on the lattice-limited upper limit of mobility μ_L, which is published for the majority of semiconductor materials:

$$\mu = \frac{\mu_L}{1 + \sqrt{\frac{n_0}{10^{17}}}} \tag{2.27}$$

The GaAs mobility $\mu_L = 10^4\ cm^2/V \cdot s$ will be used in order to compare results of the equal-areas code against Butcher and Fawcett's published results. Using (2.27) in Equations (2.22) – (2.26) fully specifies $v(E)$ in terms of the *doping* of the material. Once $v(E)$ has been determined as decribed above, the integration limits required for the domain calculation can be found. The code calculates the domain in terms of a user-specified drift velocity v_r.

With $v(E)$ and v_r specified, the minimum electric field E_r is readily determined by running a lookup on the data array which holds the data for E and $v(E)$. The maximum peak domain field E_{dom} is then calculated using a simple numerical integration of these data, as required by Equation (2.21). Figure 2.3 shows $v(E)$ for GaAs with $n_0 = 7 \times 10^{16}\ cm^{-3}$. This is the condition for which the domain profiles calculated using this code are compared to Butcher and Fawcett's published domain profiles. The yellow lines in Figure 2.3 indicate the calculated minimum and maximum electric field values E_r and E_{dom} corresponding to a selected drift velocity $v_r = 1 \times 10^7\ cm/s$. The first step of the domain calculation is to solve the

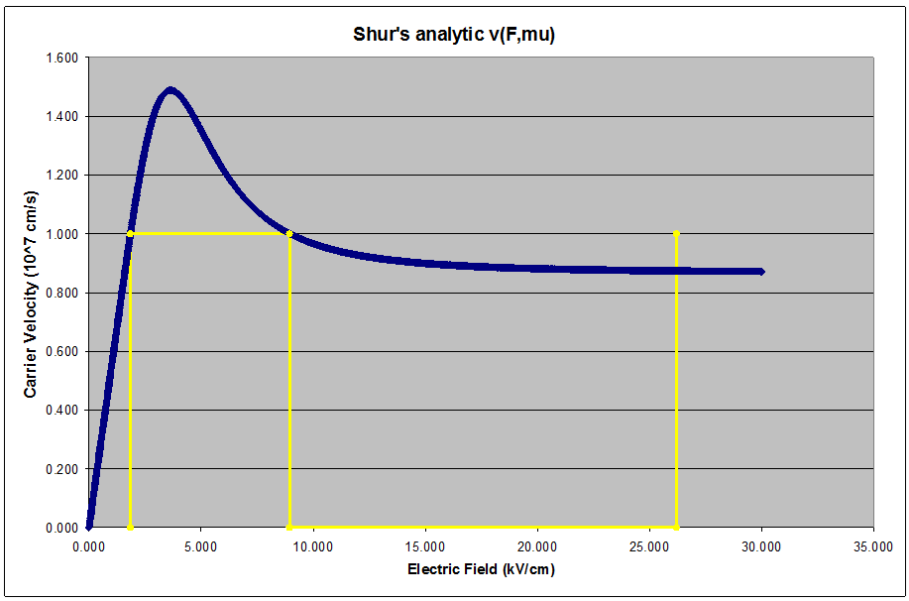

Figure 2.3: Shur's analytic $v(E)$ characteristic for GaAs, $n_0 = 7 \times 10^{16}\ cm^{-3}$. Yellow lines show the equal-areas condition (2.21) for $v_r = 1 \times 10^7\ cm/s$.

transcendental equation (2.20). This solution determines $n(E)$, which is the electron concentration n as a function of electric field E within the domain. The "brute-force" solution of (2.20) is accomplished in the following manner: First the code divides the range of electric field values E between E_r and E_{dom} into a series of discrete mesh points. The mesh density is user-specified, and the electric field values at each mesh point are stored in a data array. Then for each discrete value of E in the mesh, the left and right-hand sides of (2.20) are calculated and stored in separate arrays. For each value in the array of left-hand solutions, a lookup is run to determine whether a matching solution exists in the array of right-hand values. The accuracy of the match between left- and right-hand side values is user-specified in order to improve convergence of the solution. This routine is run over both the accumulation and depletion branches of the domain. The $n(E)$ plot calculated from the conditions of

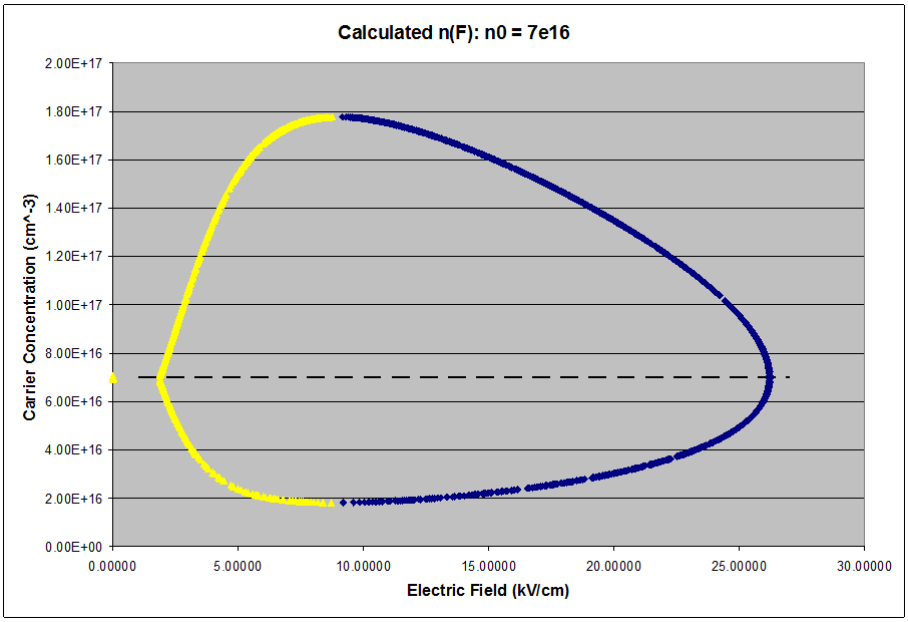

Figure 2.4: The first step of the calculation is to solve transcendental equation (2.20) to determine electron concentration as a function of electric field, $n(E)$.

Figure 2.3 is shown in Figure 2.4.

Once the $n(E)$ calculation has been completed, the second step of the domain calculation is performed. In this step of the calculation, the description of the domain's *electrical* characteristics are converted to a more intuitive *spatial* description. This change in perspective is accomplished by utilizing the integral relationship given in Equation (2.19). For each point in the $n(E)$ solution, Equation (2.19) is solved numerically. This is what determines $E(y)$, the electric field as a function of the moving spatial coordinate. As was done when calculating $n(E)$, the separate solutions are carried out on both the depletion and accumulation branches of the domain. The $E(y)$ plot corresponding to the $n(E)$ solution from Figure 2.4 is shown in Figure 2.5. Butcher and Fawcett published $E(y)$ solutions in the article used for verification of the code under consideration. They preferred to specify domains in terms of the peak

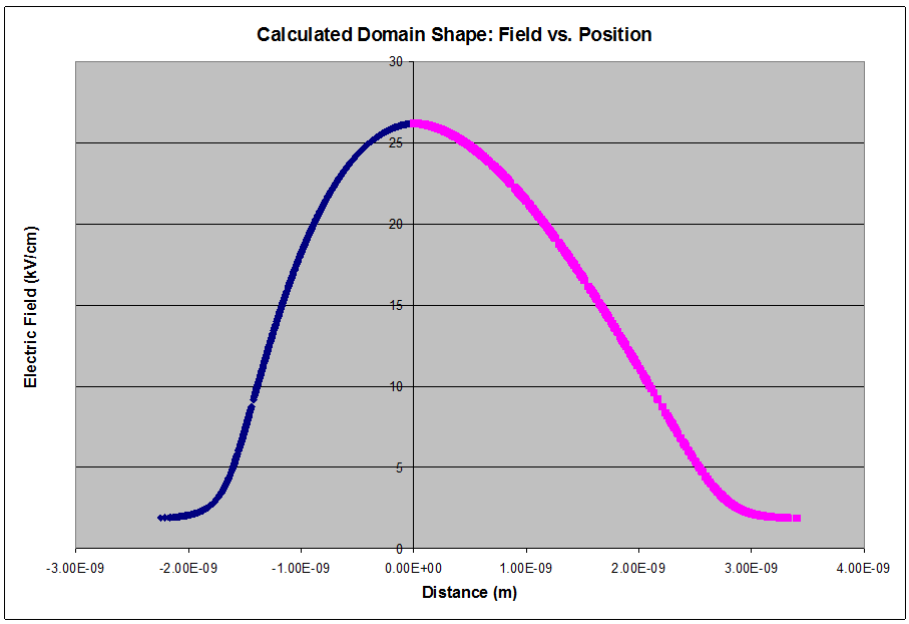

Figure 2.5: The second step of the calculation converts the *electrical* relationship $n(E)$ of Figure 2.4 into the *spatial* profile of the domain's electric field $E(y)$.

electric field E_{dom} instead of the drift velocity v_r used in the calculation code. Since experimental studies of the transferred-electron effect show that the drift velocity of the dipole domain follows the $v(E)$ characteristic, these descriptions are completely equivalent.

In the reference article, Butcher and Fawcett provide six different domain profiles in terms of electric field as a function of moving coordinate $E(y)$. The domains correspond to a range of electric field maxima (*i.e.* six different domain drift velocities). As can be seen in Figure 2.6, domains formed at lower device voltages are narrower (and faster) than higher-voltage domains.

The faster, narrower low-field domains contain less charge than the wider, slower high-field domains. Above it was noted that the radiation frequency of the Smith-Purcell semiconductor THz source depends on domain velocity according to Equation

(1.6). The higher-field domains, however, contain more charge than the lower-field domains, and this generally implies higher radiated power from the Smith-Purcell device. The performance tradeoffs associated with domain size and velocity will be discussed in more detail below.

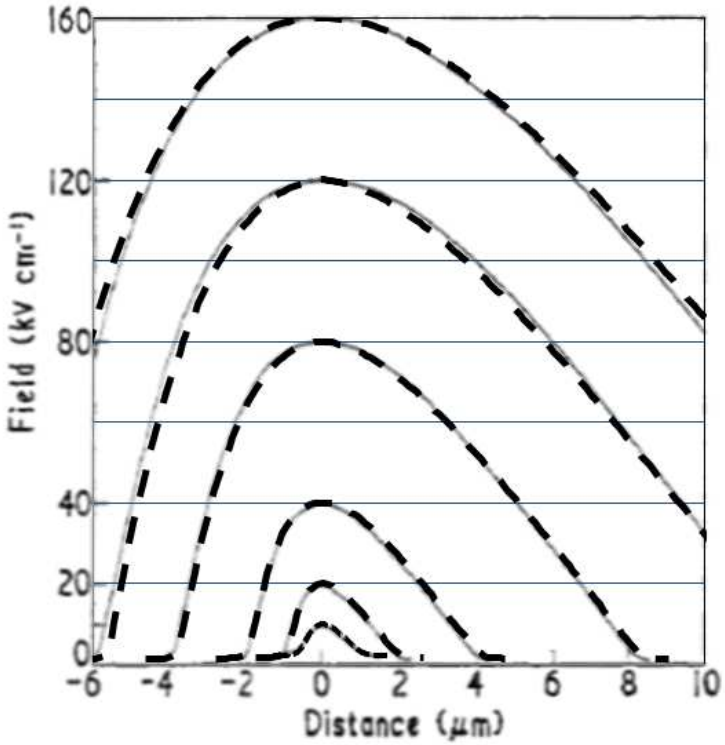

Figure 2.6: Verification of the domain-calculation code. $E(y)$ plots calculated using the code (dashed lines) are overlaid on the published profiles.

To verify that the equal-areas code worked correctly, $E(y)$ domain plots were calculated for the six conditions given in the reference article. An image from Butcher and Fawcett's article was sized to match the ® plots of the six domains. This is in fact the origin of Figure 2.6, and it shows clearly that the code accurately determines

domain profiles. [66]

For analysis of the Smith-Purcell semiconductor device, a domain profile given in terms of the electric field is not as useful as a spatial description of the dipole's charge distribution. Therefore, the third and final step of the domain calculation is to convert $E(y)$ to $n(y)$. Poisson's equation (2.11) shows that a straightforward calculation of the deriviative of $E(y)$ is sufficient to determine $n(y)$. As will be discussed in more detail below, the key quantity for analysis of the Smith-Purcell effect is the *net electron concentration* as a function of position $n(y) - n_0$ shown in Figure 2.7.

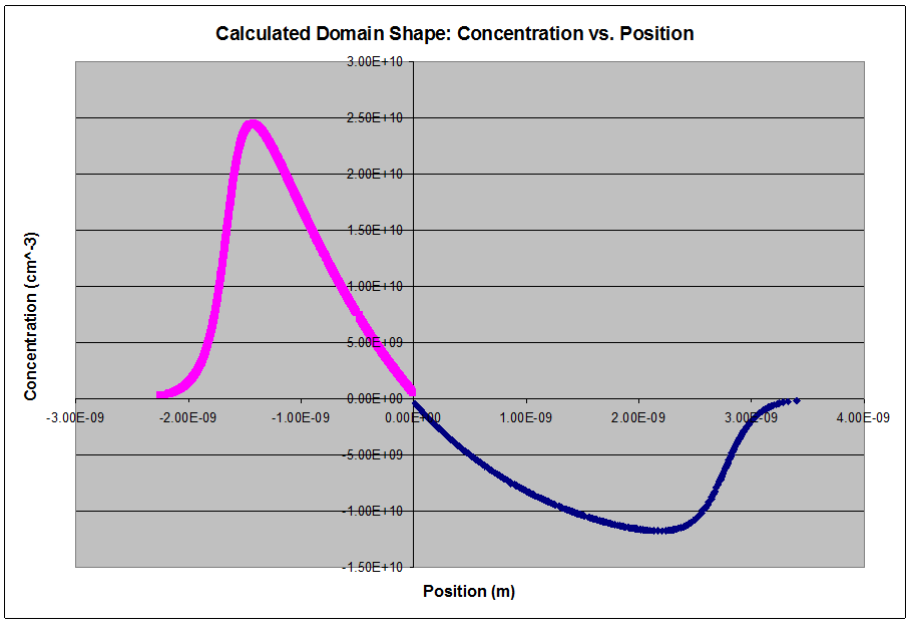

Figure 2.7: The third and final step of the Butcher-Fawcett method is to use Poisson's equation (2.11) to convert the electric field domain profile $E(y)$ into the net electron concentration profile $n(y) - n_0$.

2.3 Analytic Representation of the Gunn Domain

The most efficient way to use the numerical results from the equal-areas method in computer simulations is to fit them to a closed-form analytic function. An analytic representation of the Gunn domain profile is also useful for semi-manual calculations. The numerically-calculated domain profiles were manually fitted to a difference of Gaussians. The numerical values for the maximum and minimum electron concentrations ρ_{max} and ρ_{min} were fitted to the function

$$\rho(y) = \rho_{max}\, e^{-\left(\frac{y+\xi_a}{2\eta_a}\right)^2} - \rho_{min}\, e^{-\left(\frac{y+\xi_d}{2\eta_d}\right)^2} \tag{2.28}$$

by selecting positions ξ_i and widths η_i for the Gaussians representing the accumulation and depletion regions of the Gunn domain, where the subscript i assumes the value a for the accumulation region and d for the depletion region.

During the manual fitting, the charge density of both the accumulation and depletion regions was integrated to ensure that the total net charge was balanced to over 99.5%. A typical example of the analytic fitting technique is shown in Figure 2.8. The manual Gaussian fitting method was found to accommodate all the various Gunn domain shapes studied in this research. This methodology was found useful in making semi-analytic theoretical predictions of device performance which compare favorably with computer simulations.

Approximating the difference of Gaussians in a spreadsheet provides a straightforward way to discretize the Gunn domain onto 1D meshes of varying density and number of elements j, and these discrete values $\rho(y_j)$ are readily concatenated into text strings. In this manner, the same spreadsheet used to make the analytic approximation to the numerical Gunn domain profile also generates code for the program used to perform the theoretical calculations. As will be discussed below, gnuplot was

used to calculate the radiated electromagnetic field quantities from the discretized Gunn domains obtained in the manner described in this section.

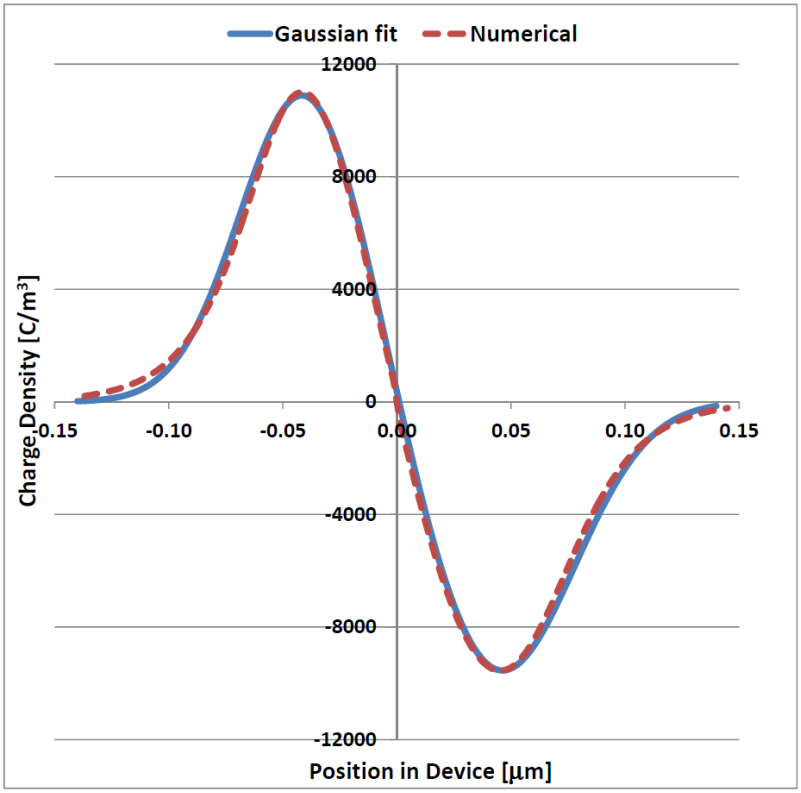

Figure 2.8: Comparison of a numerically-calculated Gunn domain profile (red) to its analytic Gaussian fit from Eq. (2.28) (blue).

3. SMITH-PURCELL EFFECT

As discussed above, the Smith-Purcell effect has historically been of interest in accelerator physics and high-power vacuum electronics. The term *Smith-Purcell effect* refers to the mechanism by which electromagnetic radiation is produced by electric charges in uniform rectilinear motion near a metallic grating. Smith and Purcell hypothesized that a vacuum electron beam focused parallel to a stationary metallic grating would create moving image-charge dipoles, and that these moving dipoles would generate electromagnetic radiation. [5] The radiation thus produced is called *Smith-Purcell radiation* (SPR).

In order to study the Smith-Purcell effect in a solid-state device, the section begins with the derivation of a simple 3D model for the Smith-Purcell radiation produced by a single point charge in close proximity to a metallic grating. This is followed by a 2D derivation of the SPR produced by a line charge, since the 2D geometry is identical to that used in computer simulations. The 2D and 3D derivations are shown to be equivalent. The principle of superposition of the electric field is then applied to the single-charge Smith-Purcell theory, which makes it possible to calculate the radiation field generated by the Gunn domains calculated in the previous section.

Combining the theoretical results for the Gunn effect (Section 2) and the Smith-Purcell effect in this manner provides very a detailed prediction of the time-domain electric field radiated from the semiconductor device. In Section 4, the theoretically-calculated electric field will be compared to the electric field from computer simulations of the device. A high degree of agreement between theory and simulation is demonstrated, validating the theoretical results.

3.1 3D Potentials of a Point Charge Near a Metallic Grating

Figure 3.1 illustrates the physical problem to be solved. A metallic grating with period P and tooth width ℓ is located in the $z = 0$ plane, with its (infinite) teeth parallel to the y-axis. A point charge q moves with non-relativistic velocity v along the positive x-axis at a height $z = b$. For simplicity, the edge of the first grating tooth is placed on the y-axis and the grating is assumed to be an integer number n of periods long so that its total length is $L = nP$.

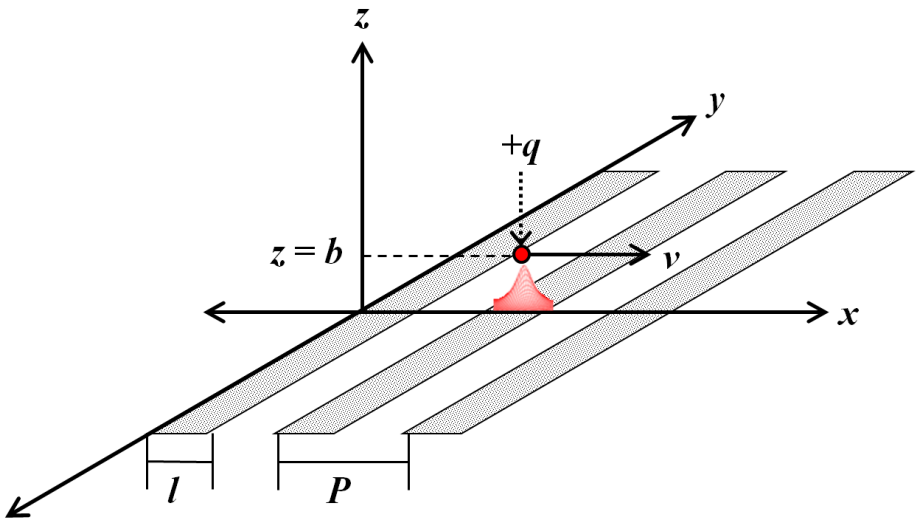

Figure 3.1: Coordinate system for a single point charge near a metallic grating.

The uniformly moving point charge does not radiate, but it will be shown that as the charge passes by the grating, the periodic image charge packets it induces on the grating teeth *do* generate electromagnetic radiation. The end goal is to determine the radiative properties of the system in the *far-field*. Thus it is advantageous to first calculate the vector and scalar potentials of this system. The potentials of a uniformly moving point charge provide a useful starting point for the derivation.

3.1.1 Uniformly Moving Point Charge

The case of a point charge q charge moving with uniform non-relativistic velocity $\boldsymbol{v}$ is treated in most introductory textbooks. The vector potential $\boldsymbol{A}$ and scalar potential Φ as observed a distance $r = |\boldsymbol{r}|$ from the point charge are given by: [75]

$$\boldsymbol{A}(\boldsymbol{r}, t) = \frac{\mu_0}{4\pi} \frac{q\boldsymbol{v}}{r} \tag{3.1}$$

$$\Phi(\boldsymbol{r}, t) = \frac{1}{4\pi\epsilon_0} \frac{q}{r} \tag{3.2}$$

Equations (3.1) and (3.2) provide a useful basis of comparison for the potentials associated with the induced image charge distribution.

3.1.2 Periodic Image Charge Distribution

Assumptions about the induced image charge are that (1) the point charge does not change direction of motion as it interacts with the grating, (2) the induced charges in the metallic grating move much more quickly than the velocity $v = |\boldsymbol{v}|$ of the point charge, and therefore (3) the actual induced charge density $\rho(\boldsymbol{r'}, t)$ can be approximated by the charge density induced on an infinite grounded conductor by a point charge q. It follows that (4) the grating is accurately modeled as a series of discrete teeth.

At low velocity and small impact parameter, it may be anticipated that the potentials of the periodic image charge should reduce to (3.1) and (3.2) "being switched on and off". The strategy to derive the potentials of the induced image charge is to simply make a "brute force" calculation of the vector potential $\boldsymbol{A}$ and scalar potential

Φ by integrating over the whole grating (V'):

$$\boldsymbol{A}(\boldsymbol{r},t) = \frac{\mu_0}{4\pi}\int_{V'} \frac{[\boldsymbol{J}(\boldsymbol{r'},t)]_{ret}}{|\boldsymbol{r}-\boldsymbol{r'}|}\, d^3r' \tag{3.3}$$

$$\Phi(\boldsymbol{r},t) = \frac{1}{4\pi\epsilon_0}\int_{V'} \frac{[\rho(\boldsymbol{r'},t)]_{ret}}{|\boldsymbol{r}-\boldsymbol{r'}|}\, d^3r' \tag{3.4}$$

Time-retarded source functions ensure that the potentials (and the electromagnetic waves calculated from them) have the correct time delay at the observation point $\boldsymbol{r}$, and have the form:

$$[f(\boldsymbol{r'},t)]_{ret} = f\left(\boldsymbol{r'}, t - \frac{|\boldsymbol{r}-\boldsymbol{r'}|}{c}\right) \tag{3.5}$$

The current density $\boldsymbol{J}(\boldsymbol{r'},t)$ is the product of the charge density $\rho(\boldsymbol{r'},t)$ and the instantaneous velocity $\boldsymbol{v}$ of the point charge as indicated in (3.6). The charge density induced at any point $\boldsymbol{r'} = (x',y',z')$ on an infinite grounded conducting plane by a moving point charge q with time-varying location $\boldsymbol{r}_q(t) = (x_q(t), y_q(t), z_q(t))$ is given by (3.7). Combining these results with (3.5) yield the retarded current density $[\boldsymbol{J}(\boldsymbol{r'},t)]_{ret}$, which is given in terms of the coordinate system from Figure 3.1 in (3.8).

$$\boldsymbol{J}(\boldsymbol{r'},t) = \rho(\boldsymbol{r'},t)\boldsymbol{v} \tag{3.6}$$

$$\rho(\boldsymbol{r'},t) = \frac{-qz_q(t)}{2\pi[(x'-x_q(t))^2 + (y'-y_q(t))^2 + (z'-z_q(t))^2]^{\frac{3}{2}}} \tag{3.7}$$

$$[\boldsymbol{J}(\boldsymbol{r'},t)]_{ret} = -\left(\frac{qbv}{2\pi}\right)\frac{\delta(z'-b)\ \hat{\boldsymbol{x}}}{[(x'-v(t-\frac{|\boldsymbol{r}-\boldsymbol{r'}|}{c}))^2 + y'^2 + z'^2]^{\frac{3}{2}}} \tag{3.8}$$

Therefore the vector potential $\boldsymbol{A}$ in Cartesian coordinates is:

$$\boldsymbol{A}(\boldsymbol{r},t) = -\left(\frac{\mu_0}{4\pi}\right)\left(\frac{qbv}{2\pi}\right)$$
$$\sum_{n=0}^{\frac{L}{P}-1}\left[\int_{nP}^{nP+\ell} dx' \int_{-\infty}^{\infty} dy' \int_{-\infty}^{\infty} \frac{\delta(z'-b)\ dz'}{|\boldsymbol{r}-\boldsymbol{r'}|\ [(x'-v(t-\frac{|\boldsymbol{r}-\boldsymbol{r'}|}{c}))^2+y'^2+z'^2]^{\frac{3}{2}}}\right]\hat{\boldsymbol{x}} \quad (3.9)$$

where:

q = magnitude of the source charge

v = non-relativistic velocity of the source charge

b = fixed source charge distance from the grating

P = grating period

ℓ = grating tooth width

n = integer number of periods the grating contains

$L = nP$ = total grating length

In order to integrate over all space, the grating as illustrated in Figure 3.1 extends to infinity in the direction transverse to the path of the point charge q, giving the limits of integration for y'. It is understood that the induced image charge is localized to a circular region with radius of several b. Similarly, the integrand along x' (the direction of motion of the point charge) vanishes when the charge is not directly above a grating tooth.

As discussed above, Equation (3.9) is solved in the case where the observation distance $\boldsymbol{r}$ is assumed large compared to the integration variable $\boldsymbol{r'}$ over the grating, since the far-fields are of particular interest. Typical device lengths are less than ten microns and the shortest wavelengths produced are of order hundreds of microns. Thus within even a few wavelengths, the device is well-represented by a point radiation source. Therefore it is justified to make the simplification $|\boldsymbol{r}-\boldsymbol{r'}| \approx |\boldsymbol{r}| = r$

which is independent of the integration variables and simplifies the expression for $\boldsymbol{A}$:

$$\boldsymbol{A}(\boldsymbol{r},t) = -\left(\frac{\mu_0}{4\pi}\right)\left(\frac{qbv}{2\pi r}\right) \sum_{n=0}^{\frac{L}{P}-1}\left[\int_{nP}^{nP+\ell} dx' \int_{-\infty}^{\infty} dy' \int_{-\infty}^{\infty} \frac{\delta(z'-b)\, dz'}{[(x'-v(t-\frac{r}{c}))^2+y'^2+z'^2]^{\frac{3}{2}}}\right]\hat{\boldsymbol{x}} \quad (3.10)$$

The delta function makes z'-integration normal to the grating trivial:

$$\boldsymbol{A}(\boldsymbol{r},t) = -\left(\frac{\mu_0}{4\pi}\right)\left(\frac{qbv}{2\pi r}\right) \sum_{n=0}^{\frac{L}{P}-1}\left[\int_{nP}^{nP+\ell} dx' \int_{-\infty}^{\infty} \frac{dy'}{[(x'-v(t-\frac{r}{c}))^2+y'^2+b^2]^{\frac{3}{2}}}\right]\hat{\boldsymbol{x}} \quad (3.11)$$

Defining $a^2 = ((x'-v(t-r/c))^2+b^2)$ allows use of the integral identity:

$$\int_{-\infty}^{\infty} \frac{dy'}{(y'^2+a^2)^{\frac{3}{2}}} = \left[\frac{y'}{a^2|y'|\sqrt{1+(a/y')^2}}\right]_{-\infty}^{\infty} = \frac{2}{a^2} \quad (3.12)$$

The identity reduces the vector potential $\boldsymbol{A}$ to:

$$\boldsymbol{A}(\boldsymbol{r},t) = -\left(\frac{\mu_0}{4\pi}\right)\left(\frac{qbv}{\pi r}\right) \sum_{n=0}^{\frac{L}{P}-1}\left[\int_{nP}^{nP+\ell} \frac{dx'}{(x'-v(t-\frac{r}{c}))^2+b^2}\right]\hat{\boldsymbol{x}} \quad (3.13)$$

Defining $u = x' - v(t-r/c)$ simplifies the last integration to:

$$\boldsymbol{A}(\boldsymbol{r},t) = -\left(\frac{\mu_0}{4\pi}\right)\left(\frac{qbv}{\pi r}\right) \sum_{n=0}^{\frac{L}{P}-1}\left[\int_{nP+vr/c-vt}^{nP+\ell+vr/c-vt} \frac{du}{u^2+b^2}\right]\hat{\boldsymbol{x}} \quad (3.14)$$

which is readily solved by using the integral identity:

$$\int \frac{du}{u^2+b^2} = \frac{\tan^{-1}(\frac{u}{b})}{b} \quad (3.15)$$

With all integrations complete, definition of $\beta = v/c$ gives the vector potential $\boldsymbol{A}$ as:

$$\boldsymbol{A}(\boldsymbol{r},t) = -\frac{\mu_0}{4\pi}\,\frac{qv}{\pi r} \sum_{n=0}^{\frac{L}{P}-1} \left\{ \tan^{-1}\left[\frac{(\beta r + nP + \ell) - vt}{b}\right] - \tan^{-1}\left[\frac{(\beta r + nP) - vt}{b}\right] \right\} \hat{\boldsymbol{x}} \quad (3.16)$$

It is convenient to define the function $F(\boldsymbol{r},t)$:

$$F(\boldsymbol{r},t) = \left(\frac{1}{\pi}\right) \sum_{n=0}^{\frac{L}{P}-1} \left[\tan^{-1}(a_1) - \tan^{-1}(a_2) \right] \quad (3.17)$$

$$\text{and } a_1 = \left(\frac{1}{b}\right)\Big(vt - (\beta r + nP)\Big) \quad (3.18)$$

$$\text{where } a_2 = \left(\frac{1}{b}\right)\Big(vt - (\beta r + nP + \ell)\Big) \quad (3.19)$$

Each term of the sum in $F(\boldsymbol{r},t)$ represents the interaction of the point charge with a single grating tooth. Depending on the values of the parameters describing the problem (which will be later shown to directly correspond to the design of the device), the nature of the interaction can be varied significantly. The definition of $F(\boldsymbol{r},t)$ provides a means to compactly write the vector potential $\boldsymbol{A}$ and scalar potential Φ (which involves the same integrations):

$$\boldsymbol{A}(\boldsymbol{r},t) = -\frac{\mu_0}{4\pi}\frac{q\boldsymbol{v}}{r}\,F(\boldsymbol{r},t) \quad (3.20)$$

$$\Phi(\boldsymbol{r},t) = -\frac{1}{4\pi\epsilon_0}\frac{q}{r}\,F(\boldsymbol{r},t) \quad (3.21)$$

Comparing the above potentials for the periodic induced charge to those of the

non-interacting charge given in Equations (3.1) and (3.2), it is seen that the only differences are the negative sign and the presence of $F(\boldsymbol{r}, t)$. The negative sign arises since the induced surface charge necessarily has the opposite polarity of q. As discussed in detail in Appendix A, $F(\boldsymbol{r}, t)$ is a switching function that varies smoothly as a function of its input parameters. In the limit of a "very strong" argument, $F(\boldsymbol{r}, t)$ approximates a finite train of rectangular pulses of unit height. The pulse width corresponds to the point charge traveling under the grating tooth as expected.

3.2 2D Fields of a Line Charge Near a Metallic Grating

Empirical investigations of Gunn diodes show that the space charge profile is uniform in the direction transverse to the motion of the domain [68]. Thus a 2D *line charge* near a metallic grating more accurately models the device operation than the 3D point charge considered above. Moreover, computer simulations utilize 2D geometry, making a 2D theoretical treatment worthwhile.

3.2.1 Static Line Image Charge Density

First consider an infinite line charge of charge density $\lambda\ C/m$ in the vicinity of an infinite grounded plane conductor as indicated in Figure 3.2. A Cartesian coordinate system is chosen which places the conductor on the x-axis, and the solution is described in cylindrical coordinates, since the line and conductor are infinite in the z-direction. The scalar potential Φ at an arbitrary point P in the half-space occupied by the source line charge λ is determined using the method of images. In terms of an arbitrary reference distance ρ_0, the scalar potential of an infinite line charge is:

$$\Phi(\boldsymbol{\rho}) = \frac{\lambda}{4\pi\epsilon_0} \ln\left(\frac{\rho_0^2}{\rho^2}\right) = \frac{\lambda}{2\pi\epsilon_0} \ln\left(\frac{\rho_0}{\rho}\right) \tag{3.22}$$

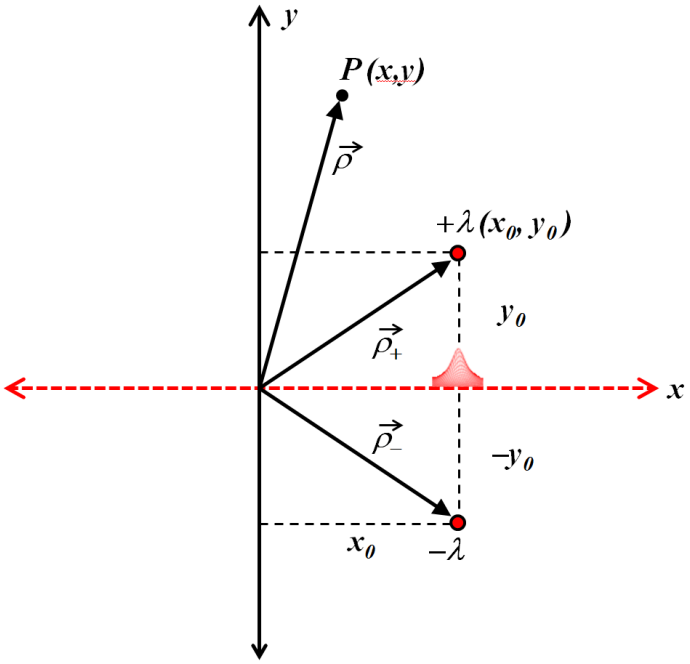

Figure 3.2: Line charge λ and its image. The x-axis is an infinite grounded plane conductor.

where in this case $\rho = |\boldsymbol{\rho}|$ is the distance from the source line charge to the observation point P. For the case of the image charge problem, Figure 3.2 shows the relevant position vectors needed to express the scalar potential:

$$\Phi(\boldsymbol{\rho}) = \frac{\lambda}{2\pi\epsilon_0}\left[\ln\left(\frac{\rho_0}{|\boldsymbol{\rho}-\boldsymbol{\rho}_+|}\right) - \ln\left(\frac{\rho_0}{|\boldsymbol{\rho}-\boldsymbol{\rho}_-|}\right)\right]$$
$$\Phi(\boldsymbol{\rho}) = \frac{\lambda}{2\pi\epsilon_0}\ln\left(\frac{|\boldsymbol{\rho}-\boldsymbol{\rho}_+|}{|\boldsymbol{\rho}-\boldsymbol{\rho}_-|}\right) \tag{3.23}$$

The induced image charge is more readily found by temporarily expressing the scalar potential in cartesian coordinates:

$$\Phi(\boldsymbol{\rho}) = \frac{\lambda}{2\pi\epsilon_0}\ln\left(\frac{\sqrt{(x-x_0)^2+(y-y_0)^2}}{\sqrt{(x-x_0)^2+(y+y_0)^2}}\right) \tag{3.24}$$

The image surface charge density σ induced on the conductor is the normal derivative of the scalar potential evaluated at the conductor:

$$\sigma = \epsilon_0(\nabla\Phi \cdot \hat{\boldsymbol{n}})\big|_{\text{conductor}} \tag{3.25}$$

In the coordinate system of Figure 3.2, the conductor is on the x-axis so that:

$$\sigma = \frac{-\lambda y_0}{\pi[(x-x_0)^2 + y_0^2]} \tag{3.26}$$

3.2.2 Potentials of the Periodic Image Charge Distribution

For the case of the line charge moving parallel to a metallic grating, the same assumptions made for the point charge are made – namely, that the static image charge distribution of Equation (3.26) continues to hold true when the line charge moves with constant velocity $\boldsymbol{v} = v\hat{\boldsymbol{x}}$ a perpendicular distance b from the grating. A delta function places the conductor at $y = 0$, which gives the surface charge density σ and current density $\boldsymbol{J}$ as functions of the observation point $P = |\boldsymbol{\rho}|$ and time t:

$$\begin{aligned} x_0 &= vt \\ y_0 &= b \\ \sigma(\boldsymbol{\rho}, t) &= -\frac{\lambda b \delta(y)}{\pi[(x-vt)^2 + b^2]} \qquad (3.27) \\ \boldsymbol{J}(\boldsymbol{\rho}, t) &= \sigma(\boldsymbol{\rho}, t)\boldsymbol{v} \qquad (3.28) \end{aligned}$$

The vector potential $\boldsymbol{A}$

$$\boldsymbol{A}(\boldsymbol{\rho}, t) = \frac{\mu_0}{4\pi}\int_{V'} \frac{[\boldsymbol{J}(\boldsymbol{\rho'}, t)]_{ret}}{|\boldsymbol{\rho} - \boldsymbol{\rho'}|}\, d^2\rho' \tag{3.29}$$

and the scalar potential Φ

$$\Phi(\boldsymbol{\rho}, t) = \frac{1}{4\pi\epsilon_0} \int_{V'} \frac{[\sigma(\boldsymbol{\rho'}, t)]_{ret}}{|\boldsymbol{\rho} - \boldsymbol{\rho'}|} \, d^2\rho' \tag{3.30}$$

are written in terms of the retarded source functions:

$$[f(\boldsymbol{\rho'}, t)]_{ret} = f\left(\boldsymbol{\rho'}, t - \frac{|\boldsymbol{\rho} - \boldsymbol{\rho'}|}{c}\right) \tag{3.31}$$

The vector potential $\boldsymbol{A}$ is given by:

$$\boldsymbol{A}(\boldsymbol{\rho}, t) = -\frac{\mu_0}{4\pi} \frac{\lambda b v}{\pi} \int_{-\infty}^{+\infty} dx' \int_{-\infty}^{+\infty} \frac{\delta(y') dy'}{|\boldsymbol{\rho} - \boldsymbol{\rho'}|[(x' - vt + \frac{v|\boldsymbol{\rho} - \boldsymbol{\rho'}|}{c})^2 + b^2]} \tag{3.32}$$

The observation distance is again assumed to be much greater than any dimension associated with integration over the grating, thus $|\boldsymbol{\rho} - \boldsymbol{\rho'}| \approx \rho$ and the y-integration is again trivial:

$$\boldsymbol{A}(\boldsymbol{\rho}, t) = -\frac{\mu_0}{4\pi} \frac{\lambda b v}{\pi\rho} \int_{-\infty}^{+\infty} \frac{dx'}{[(x' - vt + \frac{v\rho}{c})^2 + b^2]} \tag{3.33}$$

The integrand again vanishes everywhere except on the grating teeth so that the vector potential $\boldsymbol{A}$ is:

$$\boldsymbol{A}(\boldsymbol{\rho}, t) = -\frac{\mu_0}{4\pi} \frac{\lambda b v}{\pi\rho} \sum_{n=0}^{L/P} \left\{ \int_{nP}^{nP+\ell} \frac{dx'}{[(x' - vt + \frac{v\rho}{c})^2 + b^2]} \right\} \hat{\boldsymbol{x}} \tag{3.34}$$

Making the substitution $u = x' - vt + \frac{v\rho}{c} \rightarrow du = dx'$:

$$\boldsymbol{A}(\boldsymbol{\rho}, t) = -\frac{\mu_0}{4\pi} \frac{\lambda b v}{\pi\rho} \sum_{n=0}^{L/P} \left\{ \int_{nP - vt + \frac{v\rho}{c}}^{nP + \ell - vt + \frac{v\rho}{c}} \frac{du}{u^2 + b^2} \right\} \hat{\boldsymbol{x}} \tag{3.35}$$

The integral has the elementary inverse tangent solution so that:

$$\boldsymbol{A}(\boldsymbol{\rho},t) = -\frac{\mu_0 \lambda v}{4\pi\rho} F(\boldsymbol{\rho},t)\hat{\boldsymbol{x}} \tag{3.36}$$

In polar coordinates, the 2D vector and scalar potentials are completely analogous to the 3D case with the point charge q replaced with a line charge with charge density λ:

$$\boldsymbol{A}(\boldsymbol{\rho},t) = -\frac{\mu_0}{4\pi}\frac{\lambda v}{\rho} F(\boldsymbol{\rho},t)\left(\cos\phi\,\hat{\boldsymbol{\rho}} - \sin\phi\,\hat{\boldsymbol{\phi}}\right) \tag{3.37}$$

$$\Phi(\boldsymbol{\rho},t) = -\frac{1}{4\pi\epsilon_0}\frac{\lambda}{\rho} F(\boldsymbol{\rho},t) \tag{3.38}$$

3.2.3 Fields of the Periodic Image Charge Distribution

The electric field, magnetic field, and Poynting vector can now be calculated from:

$$\boldsymbol{E}(\boldsymbol{\rho},t) = -\nabla\Phi - \frac{\partial \boldsymbol{A}}{\partial t} = \boldsymbol{E}_\Phi + \boldsymbol{E}_A \tag{3.39}$$

$$\boldsymbol{B}(\boldsymbol{\rho},t) = \nabla \times \boldsymbol{A} \tag{3.40}$$

$$\boldsymbol{S}(\boldsymbol{\rho},t) = \frac{1}{\mu_0}\boldsymbol{E} \times \boldsymbol{B} \tag{3.41}$$

As discussed in Appendix A, the partial derivatives of $F(\boldsymbol{\rho},t)$ are:

$$\frac{\partial F}{\partial t} = \frac{v}{\pi b}\, G(\boldsymbol{\rho},t) \tag{3.42}$$

$$\frac{\partial F}{\partial \rho} = -\left(\frac{\beta}{b\pi}\right) G(\boldsymbol{\rho},t) = -\frac{1}{c}\frac{\partial F}{\partial t} \tag{3.43}$$

Thus the electric field components $\boldsymbol{E}_\Phi$ and $\boldsymbol{E}_A$ are:

$$\boldsymbol{E}_\Phi = \frac{\lambda}{4\pi\epsilon_0}\left(\frac{\beta}{b\pi}\frac{G}{\rho} - \frac{F}{\rho^2}\right)\hat{\boldsymbol{\rho}} \tag{3.44}$$

$$\boldsymbol{E}_A = \frac{\mu_0}{4\pi^2}\frac{\lambda v^2}{b\rho}G\Big(\cos\phi\,\hat{\boldsymbol{\rho}} - \sin\phi\,\hat{\boldsymbol{\phi}}\Big) \tag{3.45}$$

The radial and angular components of the electric field E_ρ and E_ϕ are given by Equations (3.46) and (3.47). As will be shown below, the radiation field is associated with the angular component of the electric field E_ϕ.

$$E_\rho = \frac{\lambda}{4\pi\epsilon_0}\frac{\beta}{\pi b\rho}G\Big(1 - \beta\cos\phi\Big) - \frac{\lambda}{4\pi\epsilon_0}\frac{F}{\rho^2} \tag{3.46}$$

$$E_\phi = \frac{\lambda}{4\pi\epsilon_0}\frac{\beta^2}{\pi b\rho}G\sin\phi \tag{3.47}$$

The magnetic field $\boldsymbol{B}$ is:

$$\boldsymbol{B} = \nabla\times\boldsymbol{A} = \begin{vmatrix} \hat{\boldsymbol{\rho}} & \hat{\boldsymbol{\phi}} & \hat{\boldsymbol{z}} \\ \frac{\partial}{\partial\rho} & \frac{1}{\rho}\frac{\partial}{\partial\phi} & \frac{\partial}{\partial z} \\ A_\rho & A_\phi & 0 \end{vmatrix} \tag{3.48}$$

The magnetic field has no radial or angular components:

$$\boldsymbol{B} = \frac{\mu_0 \lambda v}{4\pi}\left(\frac{\partial}{\partial\rho}\frac{F\sin\phi}{\rho} + \frac{1}{\rho}\frac{\partial}{\partial\phi}\frac{F\cos\phi}{\rho}\right)\hat{\boldsymbol{z}} \tag{3.49}$$

$$B_z = \frac{1}{c}\frac{\lambda}{4\pi\epsilon_0}\frac{\beta^2}{\pi b\rho}G\sin\phi - \frac{\mu_0}{4\pi}\frac{2\lambda v}{\rho^2}F\sin\phi \tag{3.50}$$

$$B_z = \frac{1}{c}E_\phi - \frac{\mu_0}{4\pi}\frac{2\lambda v}{\rho^2}F\sin\phi \tag{3.51}$$

The $1/\rho^2$ terms are disregarded, since only *radiation* fields are of interest for device operation. The Poynting vector $\boldsymbol{S}$ (electromagnetic power flow) is directed radially outward, away from the device. Equation (3.53) shows that the radiated power of a single charge behaves as a point Larmor dipole radiator. Its power varies as the fourth power of velocity and the square of the charge density.

$$\boldsymbol{S} = \frac{1}{\mu_0}\boldsymbol{E}\times\boldsymbol{B} = \frac{1}{\mu_0}\begin{vmatrix} \hat{\boldsymbol{\rho}} & \hat{\boldsymbol{\phi}} & \hat{\boldsymbol{z}} \\ 0 & E_\phi & 0 \\ 0 & 0 & B_z \end{vmatrix} = \frac{E_\phi B_z}{\mu_0}\hat{\boldsymbol{\rho}} = \frac{E_\phi^2}{c\mu_0}\hat{\boldsymbol{\rho}} \tag{3.52}$$

$$\boldsymbol{S} = \frac{1}{c\mu_0}\left(\frac{\lambda}{4\pi\epsilon_0}\right)^2\left(\frac{\beta^2}{\pi b\rho}\right)^2 G(\rho,t)^2\sin^2\phi\,\hat{\boldsymbol{\rho}} \tag{3.53}$$

4. THEORY VS. SIMULATION

The principle of superposition allows the single-charge Smith-Purcell theory developed in Section 3 to be applied to the Gunn domains calculated using the methods of Section 2. This is achieved by first discretizing the analytic approximation of the Gunn domain given in Equation (2.28) on a finite number of points j. The resulting array of sampled values (y_j, ρ_j) of position within the domain and corresponding 1D charge density are transformed into coordinates suitable for use with Equation (2.28).

Gnuplot is used to calculate the j-term superposition of the electric field $E_\phi(t)$ radiated by the device as a function of time at a fixed point in space. The analytic result for $E_\phi(t)$ obtained from gnuplot is compared to that obtained from to Comsol® computer simulations of "bare devices" – devices without antennas present to maximize power output.

4.1 Finalizing the Analytic Model

In Section 3, the 1D charge density inside the Gunn domain ρ_j was shown to be constant in the direction transverse to the motion of the domain. Thus each ρ_j can be represented by a 2D line charge λ_j in Equation (3.47). Likewise, the within-domain location coordinates y_j can all be transformed to the same frame of reference x_j defined in Figure 3.2. An Excel® routine was used to create the gnuplot scripts to calculate the j equations needed to determine the superposed electric field created by the Gunn domain.

The gnuplot script superposing the j equations was written to calculate the azimuthal electric field as a function of time at an observation point chosen to be a fixed distance ρ normal to the midpoint of the device, in order to make direct com-

parison with computer simulations. In order to evaluate the impact of discretization on the stability of the gunplot solutions, the number of points j was varied from a very sparse 20-element array to a very dense 4000-point array. For each solution, the superposed electric field was determined from the relationship:

$$E_\phi(t) = \frac{1}{j}\sum_{i=1}^{j} E_{\phi,i}(t) \tag{4.1}$$

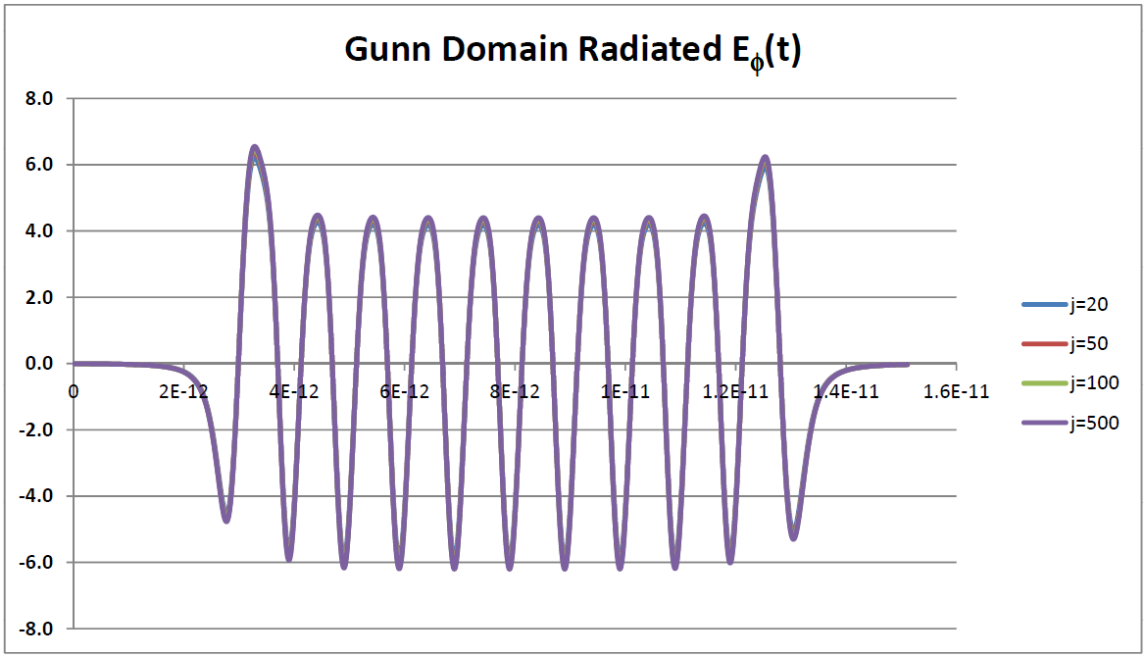

Figure 4.1: Analytically-calculated radiated electric field $E_\phi(t)$ at fixed distance of 3 wavelengths for a Gunn domain discretized to 20, 50, 100, and 500 points.

Figure 4.1 shows that varying j from 20 to 500 has no effect on the analytically-calculated $E_\phi(t)$. It was observed that the sparsest representations of the Gunn

domain did introduce a few percent underestimation of the minima of the field oscillations. Additional calculations with $j = 1000$ and $j = 4000$ did not show any significant difference from the $j = 500$ result. Therefore all subsequent analytic calculations were done using a 500-point sampling of the Gunn domains.

The gnuplot analytic model is only intended to demonstrate physical understanding of the operation of the device. For the model to be a fully predictive design tool, it would have to accurately comprehend three quantities: (1) the finite thickness of the Gunn drift region, (2) the dielectric constant of the constituent materials , and (3) the radiation resistance of the device as a function of its length and environment. This is manually calibrated for one specific case to demonstrate the level of agreement that can between achieved the analytic model and computer simulations. In practice, the simulations are found to be a more useful design tool since they solve quickly, as will be discussed in more detail below. Implementing a robust analytic design tool is beyond the scope of this research, but is noted as an opportunity for further research.

The 1D mesh used to represent the Gunn domain does not accurately capture the contributions to the radiation field of a finite-thickness drift region. The gnuplot calculation used to calibrate the model to the computer utilizes a second sum to numerically integrate over the impact parameter b in order to more accurately represent the thin (100Å) drift region used in the simulations. For the calibration exercise, the gnuplot script was run at 10Å increments around each simulated value of b shown in Figure 4.2. The resulting analytic values were then calculated from:

$$E_\phi(t) = \frac{1}{j}\sum_{k=1}^{m}\sum_{i=1}^{j} E_{\phi,ik}(t, b_k) \tag{4.2}$$

The presence of dielectrics slightly alter the solution of image charge problems.

In textbooks, these are typically presented as minor corrections to the idealized all-vacuum solutions. This model was followed in Section 3 to streamline the presentation, and therefore the derivation of SPR from a single charge did not explicitly include dielectrics. There are a number of ways to rigorously introduce dielectrics into an electrodynamic theory. For the purposes of this exercise, the simplest approach was to assign an effective dielectric thickness b'_k to the analytically-calculated field minima given in Equation (4.2):

$$b'_k = \left(\frac{\epsilon + 1}{\epsilon - 1}\right) b_k \tag{4.3}$$

The dielectric constant used in most simulations was $\epsilon = 12.85$.

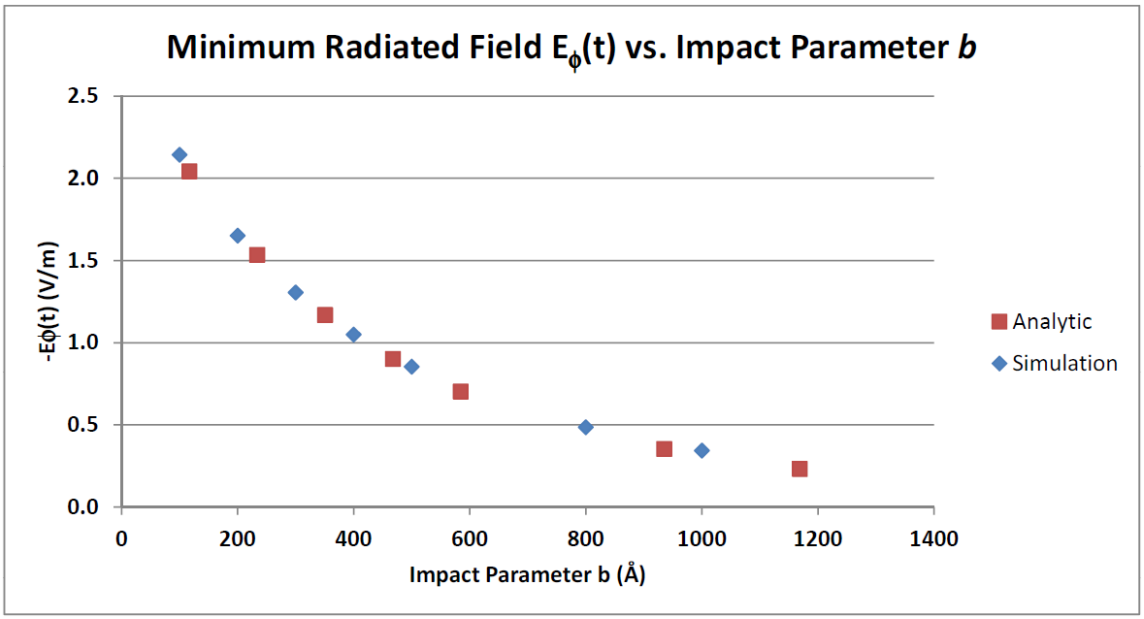

Figure 4.2: Comparison of the analytically-calculated minimum electric field $E_\phi(t)$ to results of computer simulations of the device.

The radiation resistance of a dipole of length L varies as $1/L^2$, and therefore short dipoles face significant difficulty coupling to their surroundings. The radiation field expression in Equation (4.1) does not depend on L, and thus does not accurately account for device length. It was evident during the model-calibration exercise that simulation of shorter devices offsets this shortcoming to a large extent. The drawback in modeling very short devices, however, is that the overall $E_\phi(t)$ waveform loses definition since the grating contains only a few periods. For this reason, the calibration exercise is targeted to matching the minima of the radiated electric field as a function of the dielectric spacer thickness b.

The result of the model-calibration exercise is given in Figure 4.2. A series of simulations was run at seven different dielectric thicknesses b. The corresponding analytically-calculated field minima are plotted as a function of the effective dielectric thickness b' as discussed above. Agreement between the two methods is more than sufficient to validate the theoretical methods. After a description of the methods used to simulate the devices, a final comparison between theory and simulation is given for the qualititative differences between grating densities. In these cases, an overall constant is manually fitted to the analytic results without further justification.

4.2 Computer Simulations of the Device

Comsol® Multiphysics, version 3.4 was selected as the program with which to perform computer simulations of the device. Simulations were performed using the time-dependent mode of the RF module to solve for in-plane transverse-magnetic (TM) waves. No attempt was made to develop a full multi-physics simulation utilizing the semiconductor module to have Comsol® internally generate Gunn domains and then pass them to the RF module. The development of a fully integrated multi-physics device model including semiconductor, thermal, and electrodynamic effects

may represent another future research opportunity.

The Comsol® model geometry of the device was identical to that pictured in Figure 1.1. Rectangular subdomains were used to model the drift region of the Gunn diode, the dielectric spacer, the grating teeth, and where applicable, the two lobes of the dipole antenna. Antenna results will be more fully discussed in the next section.

As discussed above, Equation (2.28) was developed using the methods of Section 2, and this equation was shown to accurately represent the space charge profile of the Gunn domain. Therefore the Gunn diode portion of the device (labeled 'Semiconductor' in Figure 1.1) was simulated with a rectangular block containing a volume current-density source term, since Comsol® seeks to solve the Maxwell relation:

$$\nabla \times \boldsymbol{B} = \mu_0 \boldsymbol{J} \tag{4.4}$$

Equation (2.28) allows use of the source term $\boldsymbol{J}(t) = \rho(t)\boldsymbol{v}$. In Section 2, the charge density $\rho(y)$ was implicitly defined as a function of time since it was derived in terms of the time-dependent variable $y = x - vt$, where it is understood that $v = v_{dom}$ is the domain velocity. To complete definition of the domain drift region, values of the dielectric constant $\epsilon = 12.85$ and electrical conductivity $\sigma = 20.4$ of the drift region were chosen to represent a typical highly-doped semiconductor.

In recently reported InGaAs heterostructure planar Gunn diodes, AlGaAs buffer layers are deposited above and below the drift region. [76] In normal device fabrication processes, it is not uncommon to cap the highly n-doped drift region with a corresponding buffer layer. Therefore the dielectric spacer region was modeled to the same dielectric constant as the drift region, as mentioned above. The conductivity σ of the spacer layer was set to that of the default quartz material definition provided with Comsol®. The thickness of the dielectric spacer corresponds to the impact

parameter b used in the Smith-Purcell theory of Section 3.

Rectangular blocks were used to represent the metallic grating teeth and the lobes of the dipole antennas. A limited number of simulations were run to ascertain the relative impact of grating thickness and composition on the output power. This was done by changing the material properties of the blocks using Comsol's® built-in definitions of copper and aluminum, since these are the preferred interconnect process technologies for mature silicon CMOS. It was found that switching to aluminum had no discernible effect on the output power of the device. The intended application of the proposed technology is its integration into a silicon CMOS process. Therefore the results presented below all use the metallic properties of copper.

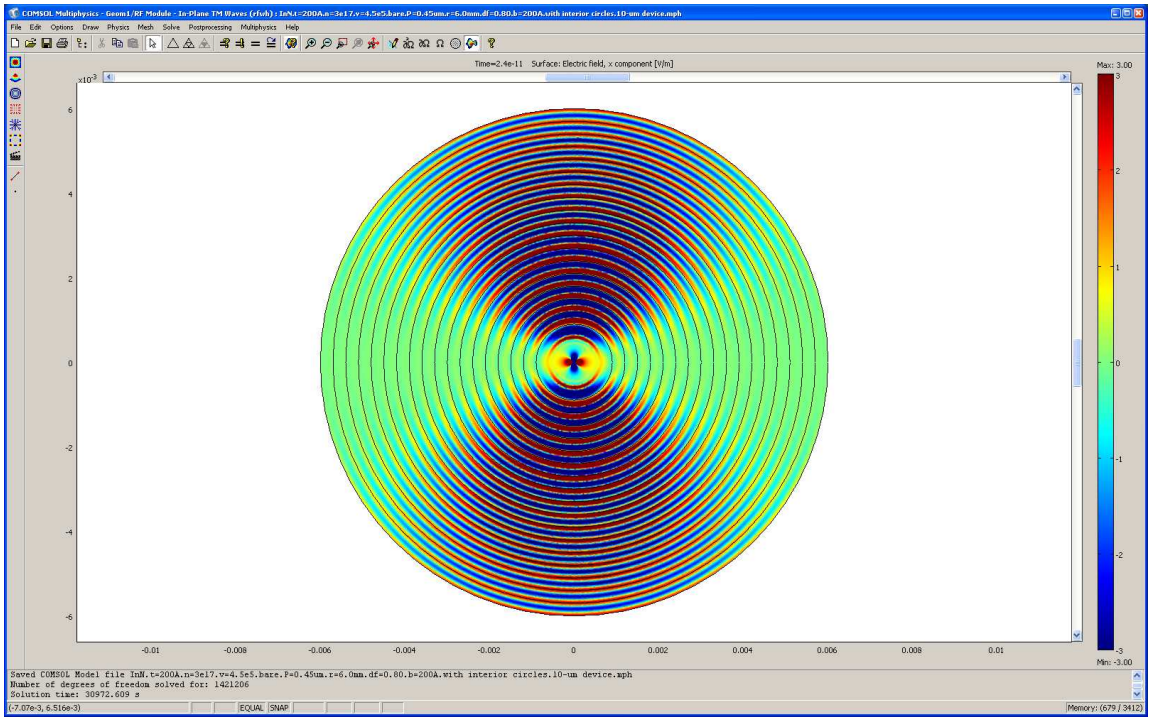

Figure 4.3: Comsol® device simulation showing E_x. The air box radius is $r = 10\lambda$.

The device geometry was placed in a large circular air box, with the device centered at the Cartesian coordinate system provided by Comsol®. The typical radius of the air box was set to three times the free-space wavelength of the device. The Smith-Purcell radiation frequency λ_{SPR} determined by the grating period P and domain velocity v is:

$$\lambda_{SPR} = \frac{c}{f_{SPR}} = \frac{cP}{v} \tag{4.5}$$

where c is the speed of light in vacuum. Figure 4.3 shows a device model with the radius of the air box set significantly larger than typical (10λ) to more clearly illustrate the dipole radiation pattern than might be seen at a distance of three wavelengths.

The outer boundary of the air box used Comsol's® scattering boundary condition and all the interior boundaries were set to continuity. Two different time-dependent solvers were evaluated in device simulations (UMFpack and PARDISO). No significant differences in the radiated electric field were observed between the solvers. Since UMFpack was found to be significantly slower than PARDISO, PARDISO was the preferred solver for all simulations. The time steps used in the simulations were chosen to ensure that the Gunn domain moved between 20Å and 50Å per time step. Depending on the length of the drift region simulated, between 300 and 2000 steps were required to simulate a single pass of the Gunn domain through the drift region. Time was added to allow the electromagnetic pulse train to fully propagate through the edge of the air box.

Various post-processing methods were used to investigate the large (tens of gigabytes) solution files created for each simulation. Perhaps the most useful information was obtained by placing a probe point into the simulation geometry at the intersection of the air box with the y-axis. The probe point collects field information at each

time step so that it can be saved immediately upon solution. In Equation (3.47) the azimuthal angle ϕ was measured from the z-axis. Measuring from the x-axis in the more usual polar notation yields:

$$E_\phi = \frac{\lambda}{4\pi\epsilon_0}\frac{\beta^2}{\pi b\rho}G\cos\phi \tag{4.6}$$

One of the post-processing modes available in Comsol® allows various field quantities to be evaluated on geometry boundaries. Evaluation of the electric field along the outer boundary of the air box confirms that the magnitude of E_ϕ during simulation displays the sinusoidal variation expected from a dipole radiation source. Therefore the use of the probe point in the simulation provides a simple proxy for the radiation passing through the entire boundary as a function of time. Additionally, using the probe plot to determine $E_\theta(t)$ also allows a simple means to calculate the *radiated power* of the device. Comsol® internally defines the instantaneous Poynting flux with the variable name nP_0. Post-processing the full (very large) solution file allows the Poynting flux (measured in W/m) to be integrated over the entire boundary for each of the hundreds of time steps in the simulation. Alternatively, the probe plot allows the instantaneous power density to be directly obtained using the following relationship:

$$nP_0(t) = c\epsilon_0\pi r E_\phi^2(t) \tag{4.7}$$

where c is the vacuum speed of light, ϵ_0 is the vacuum permittivity, and r is the radius of the air box. This method is used to calculate the simulated power densities throughout the remainder of this work.

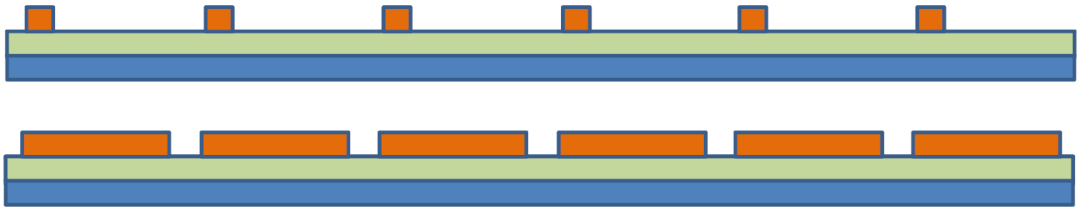

Figure 4.4: Schematic of gratings with density $\delta = 0.1$ (upper) and $\delta = 0.8$ (lower).

4.3 Electric Field From Sparse and Dense Gratings

The analytic Gunn-Smith-Purcell theory developed in Sections 2 and 3 has a high degree of qualitative agreement with simulation. This is can be seen by comparing the theory to simulation for a Gunn domain passing by gratings with fixed period P but different grating density δ (defined as the ratio of the tooth width to the grating period, as discussed in Appendix A). Figure 4.4 illustrates a sparse grating with $\delta = 0.1$ and a dense grating with $\delta = 0.8$.

The domain profile shown in Figure 4.5 is calculated for indium nitride with bulk doping density of $3 \times 10^{23}\, electrons/m^3$. The drift velocity is selected to be $4.5 \times 10^5\, m/sec$, resulting in a Smith-Purcell radiation frequency of 1.0 THz. The tradeoff with Gunn domains is that higher applied bias increases the domain size and therefore increases radiated RF power. However, the larger domain has lower drift velocity and thus lower frequency. Additionally, the increased bias increases the DC current. Since there is not corresponding increase in RF power, the efficiency of the device is decreased. This tradeoff is well-known in the experimental Gunn diode literature and is discussed in more detail below. [77]

Figure 4.6 shows analytic and simulation results for $E_\phi(t)$ from the sparse grating. The electric field is characterized in this case by positive spikes generated as the

domain passes under the narrow grating teeth. The analytic result correctly identifies the slight asymmetry between the depletion and accumulation regions that can be seen in the Gunn domain profile of Figure 4.5. The analytic result does not precisely capture the behavior of the domain as it passes through the large open regions between grating teeth, but clearly approximates the salient qualitative features of $E_\phi(t)$.

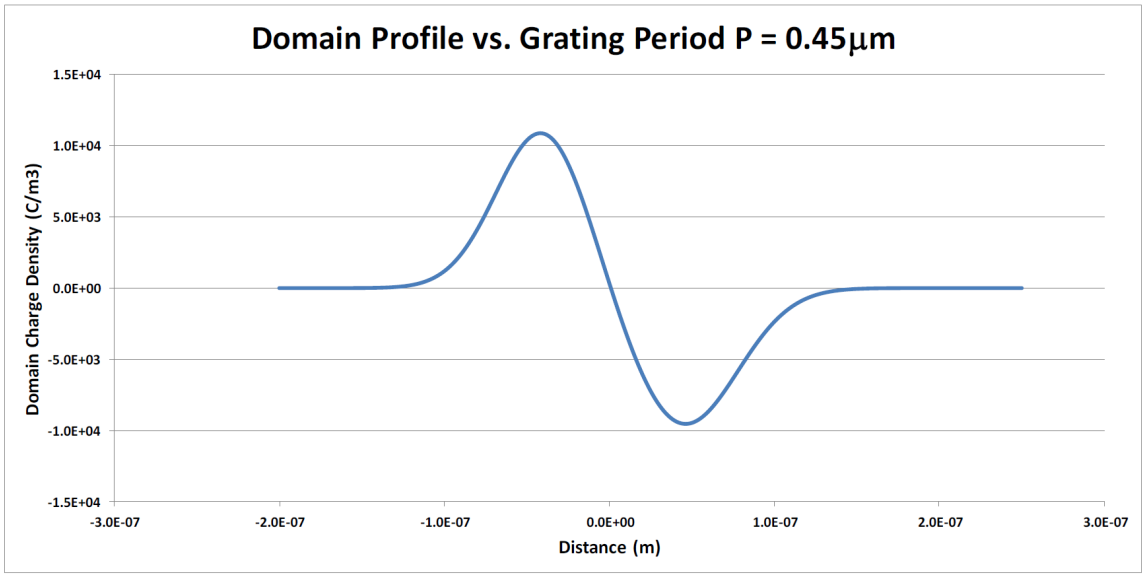

Figure 4.5: InN Gunn domain used to compare analytic theory to computer simulation. The width of the line corresponds to the grating period $P = 0.45\mu m$.

In much the same manner, the analytic result for the dense grating with $\delta = 0.8$ also corresponds closely with the results of computer simulation. The primary characteristic of the dense grating is seen to be the large negative pulse generated as the domain travels past the narrow gap between grating teeth. The distortion of the first pulse of the simulation results of Figure 4.7 is an artifact – the initial

position of the pulse starts directly under the first grating tooth. Again it is clearly seen that the analytic calculation accurately detects the asymmetry of the Gunn domain and the direction and size of the electric field pulses. The analytic result slightly overestimates the edge contributions of the grating teeth, exactly as it did in the case of the sparse grating. Now that a correspondence between theory and simulation has been established, all further results in this work will specifically refer to simulations.

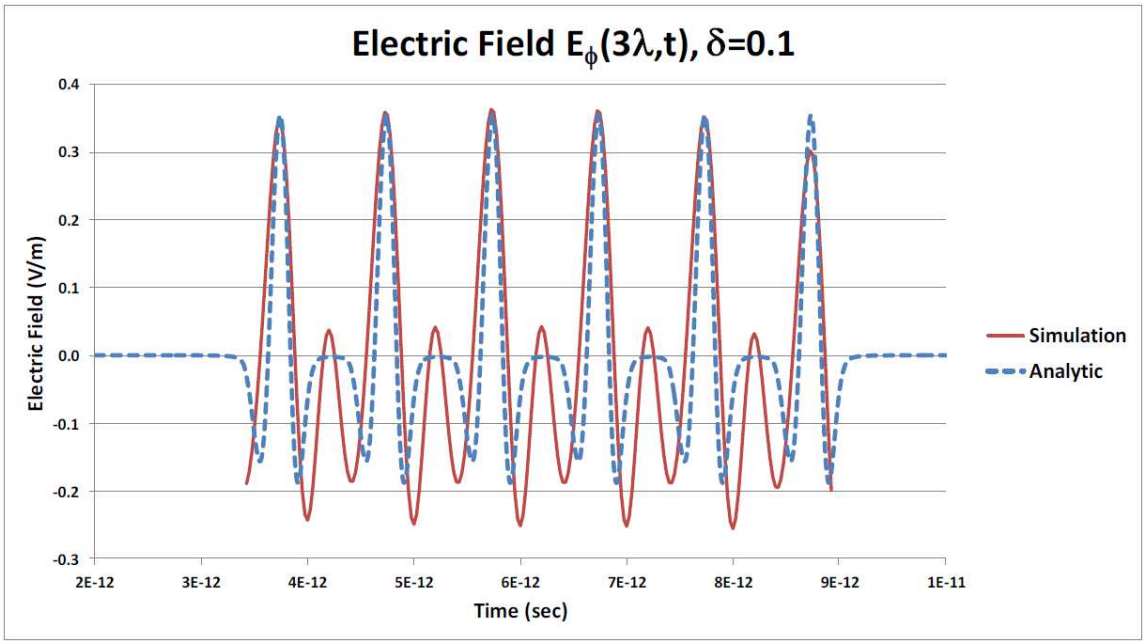

Figure 4.6: Comparison of the analytic and simulation results for $E_\phi(t)$ in the case of a Gunn domain passing near a sparse grating ($\delta = 0.1$). The main contribution to the electric field is made by the narrow grating tooth (positive spikes).

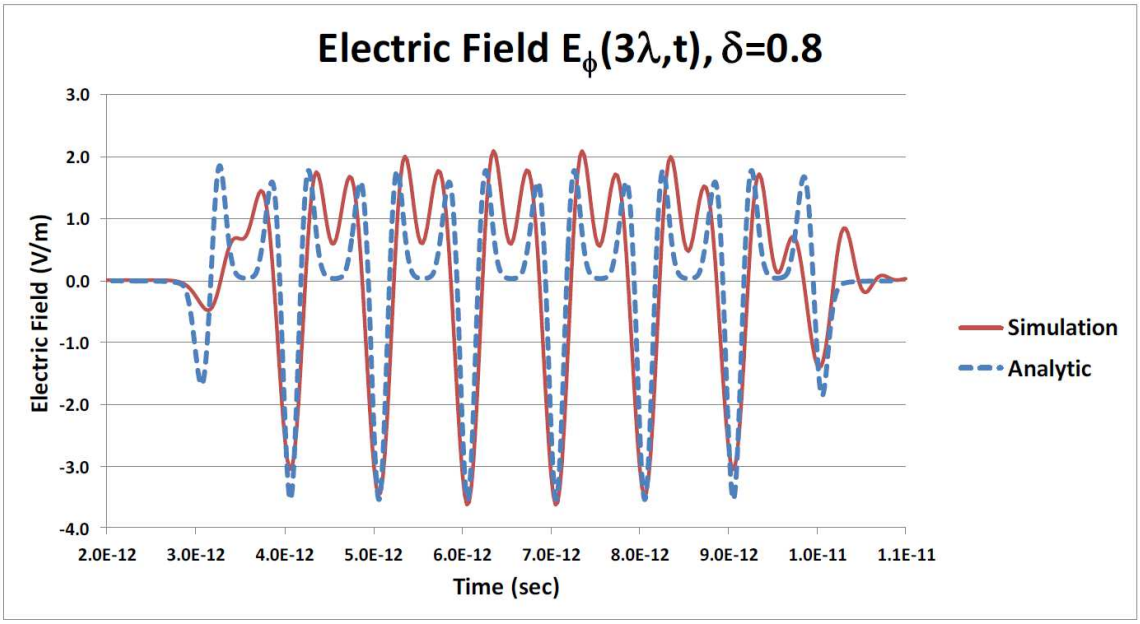

Figure 4.7: Comparison of $E_\phi(t)$ for a dense grating (density $\delta = 0.8$). In distinction to Figure 4.6, the main electric field contribution is made from the narrow *gaps* between grating teeth (negative spikes).

5. RESULTS

As discussed in more detail in the Conclusion, a follow-up research topic related to this work is the improvement of device modeling. Currently the most effective method to determine the SPR power density of a specific device is simulation. This is due to the high degree of interaction between the various electrical and geometry design parameters inherent in the operation of the device. This section presents the impact of these design parameters on the SPR power density output (performance) of Smith-Purcell devices with and without an integrated antenna. It is understood that a comprehensive multi-variate characterization is well beyond the current scope.

5.1 Performance of Bare Devices

For practical radiative applications, the most important device characteristic is its SPR power density. Therefore it is important to determine the manner in which the SPR power density depends on the device design parameters. Adding an integrated antenna significantly boosts the SPR power density radiated by a bare device, as presented below. The results of this section illustrate the role that device length L plays, even for the very short (few μm) bare devices currently under consideration. As discussed Section 6, bare devices without an integrated antenna may play an important role in future millimeter-wave and terahertz integrated circuits.

All results use the probe-point methodology described in Section 4 to collect electric field data as a function of time at a fixed point three wavelengths normal to the midpoint of the device. These data were imported into Excel®, and Equation (4.7) was applied to convert the electric field time traces into instantaneous power density traces, from which the average power density values were then calculated.

5.1.1 *Power vs. Domain Charge Density*

Equation (3.53) of Section 3 also indicates that the SPR power density varies as the square of the charge density – it is *stimulated* Smith-Purcell radiation. A set of non-physical simulations were run in which the total integrated charge density Q of the Gunn domain was varied while keeping the domain shape and velocity constant. The exercise of verifying the SPR power density dependence on Q provides a good check on whether the device simulations were developed and implemented correctly. Since Comsol® solves Maxwell's Equations and because the Gunn domain is directly entered into the simulation as a current density source term, deviation of the simulated power from the expected Q^2 dependence would indicate a serious error in either the theory or experiment.

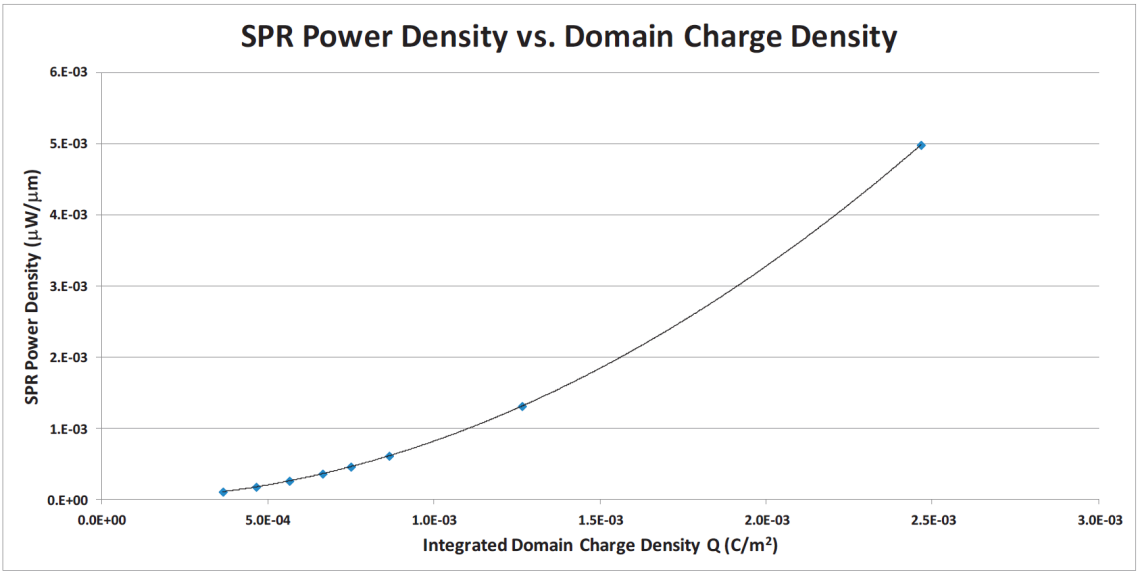

Figure 5.1: The power density of the bare Smith-Purcell device varies as the square of the Gunn domain integrated charge density Q^2, consistent with Equation (3.53).

Figure 5.1 shows that the SPR power density calculated from the simulations using the probe-point methodology described above does indeed have the expected Q^2 dependence derived in Equation (3.53). The Excel® Q^2 trend line had a perfect fit metric of $R^2 = 100.00\%$, and no further confirmation was attempted.

5.1.2 Power vs. Domain Velocity

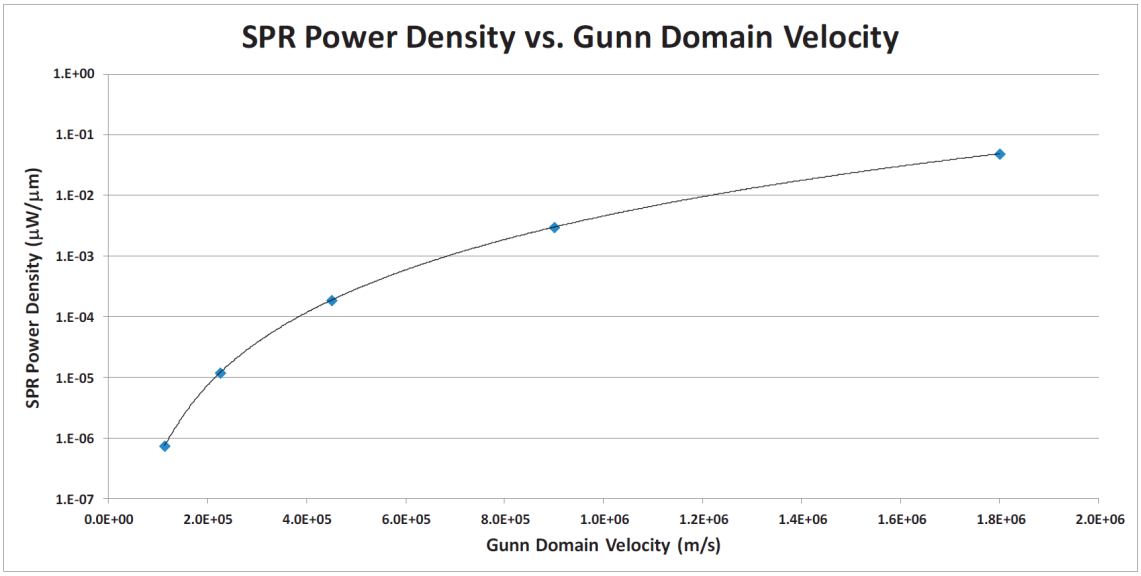

Figure 5.2: The power density of the bare Smith-Purcell device varies as the fourth power of the Gunn domain velocity v^4, consistent with Equation (3.53).

The theoretical calculations in Section 3 develop the properties of the radiated fields. Equation (3.53) predicts that the radiated power varies as the fourth power of the velocity of the charge – that the device behaves as a point Larmor dipole radiator. In order to examine this prediction with Comsol®, a different set of non-physical simulations was performed in which all parameters were held constant except for the domain velocity. As was presented in Section 2, a physical Gunn domain changes

shape under the different applied bias required to change its velocity.

Additionally, the maximum velocity of the domain used in this set of simulations was $1.8 \times 10^6\ m/s$, significantly higher than any currently-known semiconductor drift velocity. The point of the exercise was to simulate the device over a wide range of Gunn domain velocity v in order to determine the dependence of power density on v. Figure 5.2 shows the result of the simulation experiment (points) and an Excel® fitted trendline of power density as a function of v^4. It is apparent that the SPR power density behaves exactly as expected from Equation (3.53).

5.1.3 Power vs. Device Length

Longer devices have higher radiated power density than short devices because of their increased ability to electromagnetically couple to their surroundings, due to their higher radiation resistance R_r. Textbook calculations of an ideal infinitesimal dipole of length L give R_r in terms of the impedance of free space $\eta = \mu_0 c$ and the radiation wavelength as:

$$R_r = C\eta \frac{2\pi}{3} \left(\frac{L}{\lambda} \right)^2 \tag{5.1}$$

The primary importance of Equation (5.1) is to determine the extent to which the THz SPR power radiated by the device scales obeys the expected device length L^2 dependence displayed by an ideal point dipole radiator. Equation (5.1) contains a device-dependent scaling factor C that is not usually presented for the ideal infinitesimal dipole. In the case of an ideal infinitesimal dipole, it is assumed that all the current flowing through the dipole actively generates power – namely, that $C = 1$.

This is *not* the case for the Smith-Purcell device, since only a portion of the RF Gunn domain current – the induced image charge – is available to generate THz SPR power. As discussed below, C provides a measure of the RF-to-THz frequency upconversion efficiency provided by the grating via the Smith-Purcell effect. This is

analogous to the DC-to-RF efficiency figure quoted in the literature for planar Gunn diodes. Smith-Purcell upconversion efficiency is considered in more detail below. The dependence of SPR power density upon device length L is first investigated.

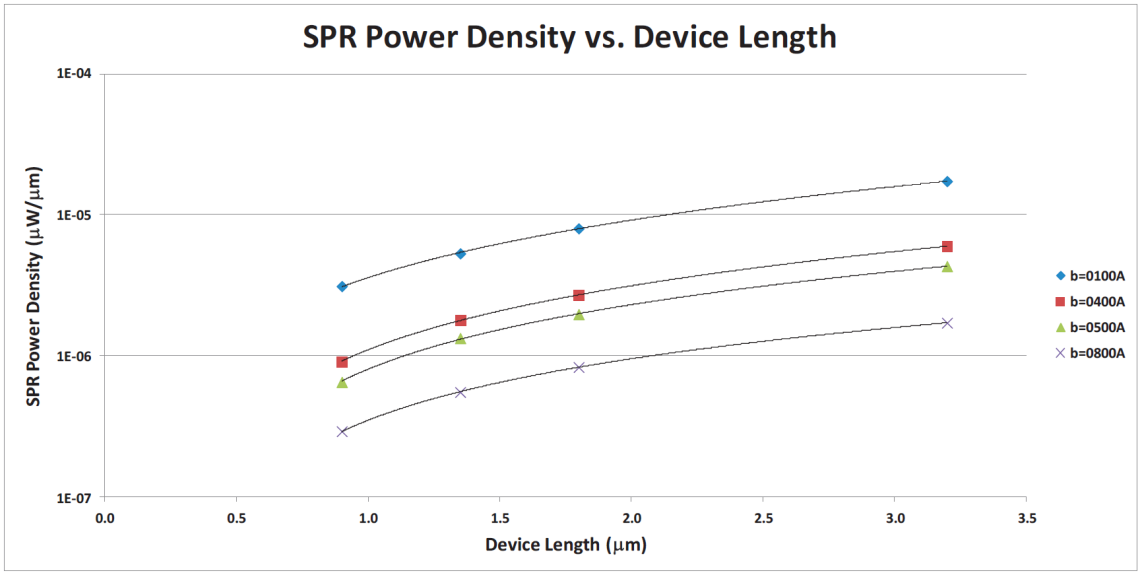

Figure 5.3: The power density of the bare Smith-Purcell device varies as the square of device length L^2, confirming the expectation of point dipole behavior.

In order to determine the dependence of SPR power density on device length L, several sets of simulations were run using the $v = 4.5 \times 10^5\, m/s$ InN Gunn domain depicted in Figure 4.5. The grating period was held fixed at $P = 0.45\mu m$, the grating density was held fixed at $\delta = 0.8$, and the grating thickness t was held fixed at 100Å. The spacer thickness b was varied for four different device lengths L. As the device length was increased, periods were added to the grating. The physical extent of the Gunn domain was $0.2\mu m$, which is smaller than the grating period P.

Moreover, it was noted in the discussion surrounding Figure 4.7 that the narrow

gaps between grating teeth make the main contribution to the electric field and thus the SPR power. These considerations lead to the expectation that the operation of the Smith-Purcell device is well-approximated by a point dipole, and therefore that the simulation results should exhibit the L^2 dependence predicted by Equation (5.1). Figure 5.3 shows the results of the simulations testing the effect of L on the SPR power density. Fitting the data series to a second-degree polynomial in Excel® makes it clear that SPR power does have the expected L^2 dependence. The R^2 quality of fit was 99.99% in two cases and 100.00% in the other two, confirming that the Smith-Purcell device indeed displays the expected behavior of a point dipole radiator.

5.1.4 THz Upconversion Efficiency

The power-versus-length investigation provides a means by which to gain insight into the RF-to-THz frequency upconversion efficiency of the bare Smith-Purcell device. A brief explanation of the DC-to-RF conversion efficiency of planar Gunn diodes is apropos. Gunn effect efficiency is observed to be in the range $1\% - 10\%$ for fixed-length devices with varying applied bias. This provides a reference point with which to compare the RF-to-THz upconversion efficiency of the Smith-Purcell effect.

The DC-to-RF efficiency in a planar Gunn diode improves at higher applied bias, and this is understood in terms of the theoretical methods of Section 2. A minimum-size Gunn domain occurs at the onset of NDR – at minimum applied bias. Domain size increases with bias until it reaches its maximum, which is determined by the electron diffusion D of the material. Applying additional bias past this point increases the diode's DC current without increasing its RF current, thus decreasing RF conversion efficiency. The DC-to-RF conversion efficiency of Gunn diodes is thus observed to increase, flatten out, and finally roll off as the applied bias is increased.

The values of C required to match Equation (5.1) to the simulation data were manually determined for the four devices. In order to do this, a method was needed to best reconcile the lack of an explicit dependence on L in the theoretical results. As discussed in Section 4, the minimum device length that could be simulated was two grating periods, which in the current case was $L_0 = 0.90\mu m$. RF-to-THz up-conversion efficiency estimates are made under the assumption the power density obtained from the minimum-length device is due to a point dipole of length $P\delta$ – the gap between grating teeth. The power density of longer devices is then systematically extrapolated from the minimum-length device by iteratively defining an effective dipole length $\Delta\ell_i = (P\delta)(L_{i+1}/L_i)$.

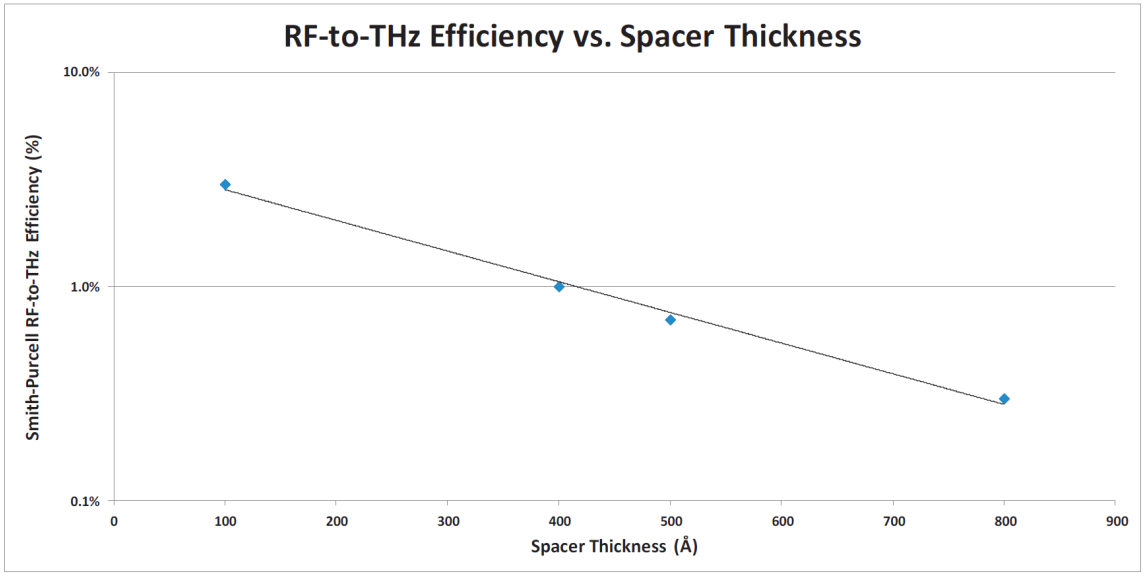

Figure 5.4: Simulation data from Figure 5.3 fitted to Equation (5.1) gives the Smith-Purcell THz power upconversion efficiency as a function of spacer thickness b.

These effective dipole lengths are then used in Equation (5.1) to determine RF-

to-THz upconversion efficiency C values that best match the simulation data for a given spacer thickness b. Figure 5.4 shows the results for C as a function of b. The THz upconversion efficiency is observed to decrease exponentially with b, varying from 3% for the $b = 100$Å device to 0.3% for the $b = 800$Å device, with an exponent of -0.0033. The exponential decrease in efficiency as a function of spacer thickness b is caused by the reduction in induced image current, as discussed below.

THz upconversion efficiency Smith-Purcell is in the single-digit range for radiation *from a bare device*. This figure is comparable to the DC-to-RF conversion efficiency provided by the Gunn effect, and it implies an overall DC-to-THz conversion efficiency in the 0.1% range, even without an antenna present. This leads to the expectation that the addition of an integrated antenna leads to a THz device with efficiency comparable to that of a planar Gunn diode. The antenna results presented below are found to be outperform standard Gunn devices in the low THz. [78]

5.1.5 Power vs. Spacer Thickness

In vacuum electronic devices, SPR power is empirically observed to decrease exponentially as the impact parameter (charge-grating separation) increases. In the semiconductor Smith-Purcell THz device, the impact parameter is controlled by the dielectric spacer thickness b. In order to determine the dependence of SPR power density on b, four sets of simulations were run. In the simulations, all parameters were held constant except for the spacer thickness b and device length L. Figure 5.5 shows the results of the twenty-five simulations run for this investigation.

All data series in Figure 5.5 were fitted with exponential trendlines in Excel®. No special statistical analysis was performed beyond the trendline fit. It was found that all four fit exponents were within 3% of the nominal exponent value of -0.0031. The Excel® quality of fit metric (R^2) was between 99.8% and 99.5% for the three longest

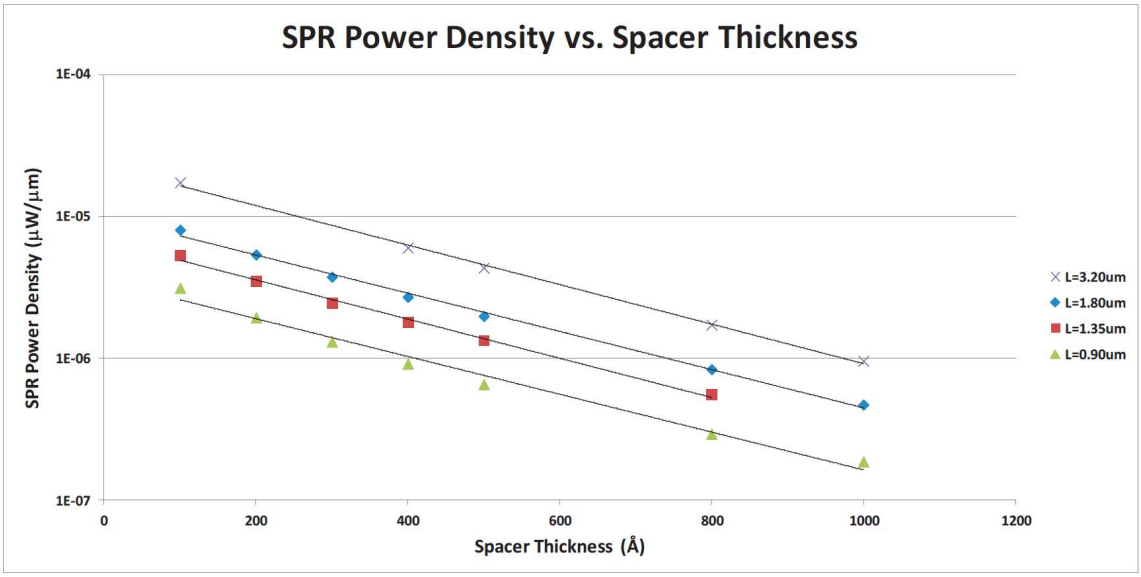

Figure 5.5: Power vs. spacer thickness is exponential (fit lines) for four different device lengths L – this matches the expectations set by empirical observations.

devices. As can be seen in Figure 5.5, the power density of the shortest ($0.9\mu m$) device – which only contained one negative spike of the form illustrated in Figure 4.7 – increases slightly faster at the very thinnest spacer values than the other devices. This leads to a slight decrease in the R^2 quality of fit of for this device ($R^2 = 98.4\%$). The results are in agreement with the Smith-Purcell effect being responsible for the THz radiation produced by the semiconductor device. The exponential decay of SPR power density with spacer thickness b confirms the result for SPR efficiency, with the decay exponents agreeing to within a few percent.

5.1.6 Power vs. Drift Region Thickness

The previous comparison between theory and simulation minimized the thickness of the Gunn drift region. This was done in order to best match the 1D Gunn theory with the 2D simulations. In practice, the thickness of the drift region t will

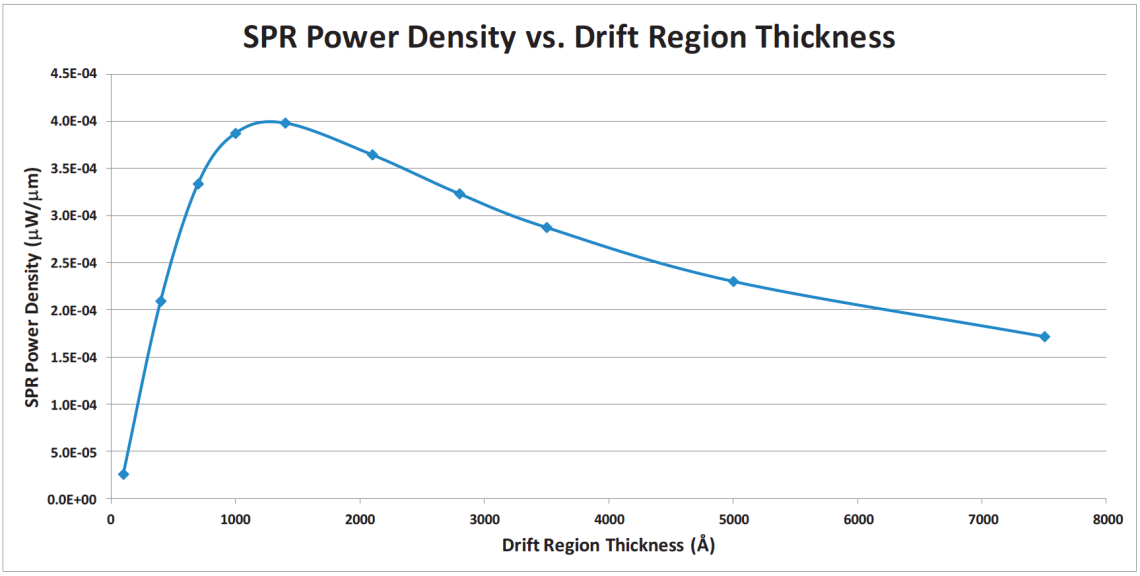

Figure 5.6: Power vs. drift region thickness t increases to a device-specific maximum at t_c then slowly decreases for $t > t_c$.

be optimized to maximize either the total SPR power density or the DC-to-THz conversion efficiency, depending on the specifics of a particular application.

Between the minimum drift region thickness (100Å) and some critical thickness t_c, it is reasonable to expect that the SPR power density will increase monotonically. Moreover, Debye charge screening leads to the expectation that power density increases fastest per unit of t increase for thinnest drift regions, and the rate of power increase per unit t slows as t_c is approached. This is expected because the charge density of the Gunn domain is reasonably uniform through the thickness of the drift region. Therefore as thin "slabs" of drift region are added to the bottom of the device, the added charge density is less effective at inducing image charge on the grating.

As the drift region becomes "too thick" (relative to the grating period P), the additional layers of charge stacked under the grating begin to diminish the ability of the domain to induce image charge. Therefore the SPR power is expected to slowly

decrease for $t > t_c$. Simulations confirm the general expectations for power density as a function of drift region thickness, as shown in Figure 5.6. Subsequent simulations, including the antenna results presented below, utilize the observed critical thickness $t_c = 1400\text{Å}$.

5.1.7 Power vs. Grating Density

Perhaps the two most important design parameters are the grating period P and the grating density δ. It is found in the course of this research that there is not yet a universal prescription for geometry optimization. As mentioned above, simulation experiments are currently required to determine the impact of the design parameters on the SPR power density. Figure 5.7 illustrates the variation of SPR power density as a function of grating density δ for devices with different spacer thicknesses b.

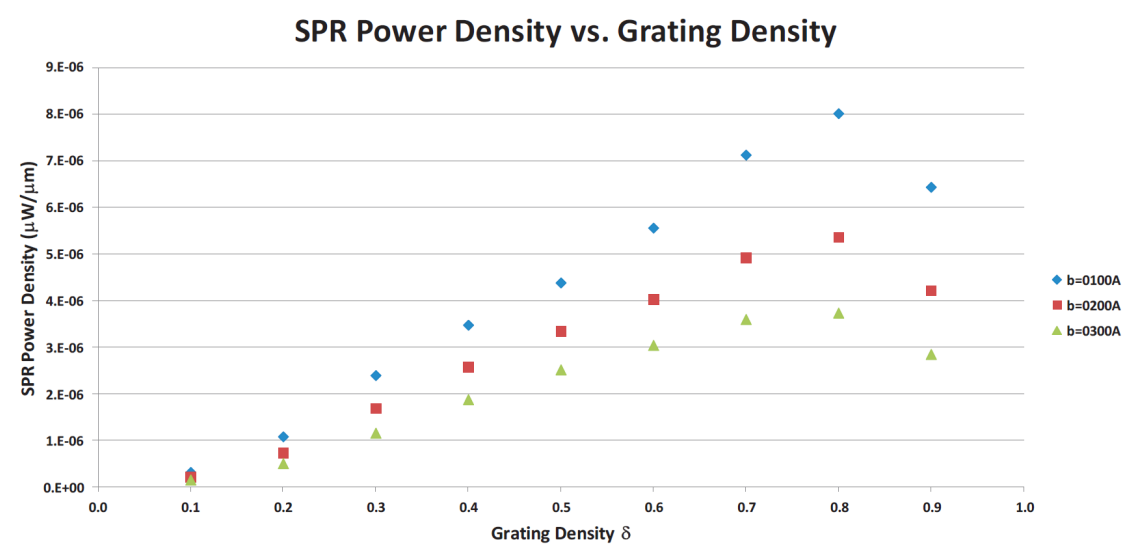

Figure 5.7: Power vs. grating density δ increases linearly up to a maximum at $\delta = 0.8$, then rolls off rapidly for very dense gratings.

The domain pictured in Figure 4.5 is used for these sets of simulations. The SPR power density is observed to increase linearly with grating density δ up to a maximum at about $\delta = 0.8$. In future work it is suggested to systematically study the optimal grating density as a function of applied bias (varying Gunn domain profiles), grating period P, and drift thickness t.

5.1.8 Power vs. Grating Period and Applied Field

The SPR power density of the bare Smith-Purcell device was shown above to behave as a point Larmor dipole source. Non-physical experiments determined the dependence of SPR power density on domain velocity v and integrated domain charge Q. The power density was found to depend on velocity as v^4 by using a fixed Gunn domain profile that did not change in width or height.

Additionally, the power density was found to depend on the square of the integrated domain charge Q^2. This was done by running a series of simulations with Gunn domains of fixed accumulation width a. In order to vary Q, the maximum charge density ρ_{max} of the domain accumulation region and the minimum charge density ρ_{min} of the depletion region were varied. In reality, the Gunn domain profile changes as a function of the applied field E.

The final design parameter considered for bare Smith-Purcell devices is the frequency f, which depends on the domain velocity v and grating period P according to Equation (1.6):

$$f = v/P$$

The grating period P of the Smith-Purcell device is a straightforward parameter to control since it is photolithographically defined. The domain velocity v, however, is non-trivially related to the applied field E via the velocity-field characteristic $v(E)$ discussed in Section 2. Referring to Figure 2.2, no Gunn oscillations occur below the

field value corresponding to the maximum electron velocity – this value of E marks the onset of NDR.

Therefore, dipole oscillations occur on the portion of the $v(E)$ curve with negative slope where v *decreases* with increasing field. However, the dependence of SPR power density on E is more complicated than just determining the drift velocity v. The complication arises from the fact it is not only the domain velocity v that changes in response to the electric field E – the entire shape of the Gunn domain changes, as shown in Figure 5.8 for n-doped InN with doping concentration $n_0 = 1 \times 10^{17}$ ion/cc. The physical characteristics of these Gunn domains are listed in Table 5.1.

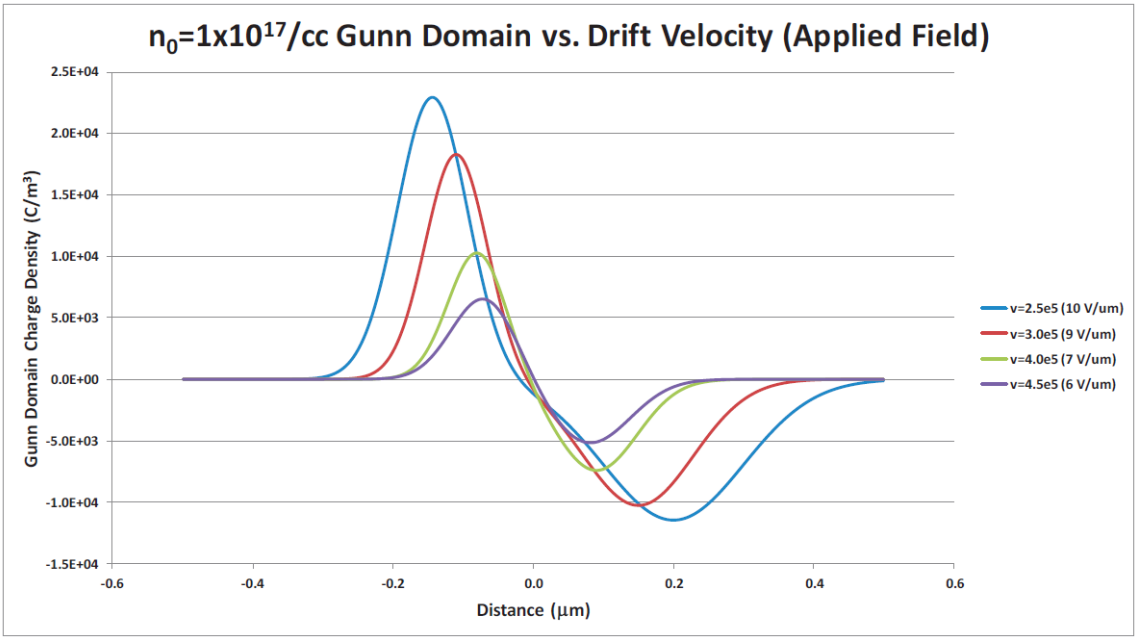

Figure 5.8: Gunn domains for InN with bulk doping concentration $n_0 = 1 \times 10^{17}$ ion/cc. Higher applied field decreases the drift velocity and increases the domain size.

A brief explanation of terminology used to refer to specific Gunn domains may

prove useful. Since the velocity-field characteristic $v(E)$ uniquely correlates each value of the applied field E to a value of the drift velocity v, references to drift velocity are interchangeable with references to the applied field. Applied field (more specifically, the *bias voltage*) is more germane to the discussion of a Smith-Purcell device within an integrated circuit, whereas drift velocity is more intuitive for the current discussion concerning only the operation of the bare Smith-Purcell device. For practical applications, the applied bias voltage required to make a specific device operate in an expected manner is a critical parameter. Moreover, the DC current generated by the Gunn diode must be managed in order to prevent thermal damage to the device.

Table 5.1: Physical characteristics of InN Gunn domains with $n_0 = 1 \times 10^{17}$.

E $(V/\mu m)$	v $(10^5 m/s)$	a (μm)	Q_{int} (C/m^2)	ρ_{max} (C/m^3)	ρ_{min} (C/m^3)
10.40	2.50	0.294	2.82×10^{-3}	22984	-11475
8.80	3.00	0.234	1.96×10^{-3}	18300	-10250
6.70	4.00	0.202	9.91×10^{-4}	10400	-7430
5.90	4.50	0.212	6.67×10^{-4}	6700	-5200

Lower applied field E produces faster and narrower Gunn domains, both of which are desirable for high frequency operation. These fast domains, however, contain less integrated charge Q. Adding to the complication is the additional dependence of power density on the size ratio ξ, defined as the ratio of the width of the grating tooth ℓ to the width of the Gunn domain's accumulation region a:

$$\xi = \frac{\ell}{a} \tag{5.2}$$

The frequency analysis of bare Smith-Purcell devices using different Gunn domains below leads to the conclusion that the size ratio ξ plays an important role in determining SPR power density. The size ratio ξ defined in Equation (5.2) explains the flatter frequency response of narrower domains, as will be shown below. Consideration of the data in Table 5.1 completes the discussion of Gunn domain variation. It is noted that the maximum charge density ρ_{max} and the total integrated charge density Q of the domains in Table 5.1 decrease with drift velocity as $1/v^2$.

Figure 5.9 shows the SPR power density of $5\mu m$-long bare devices with $0.14\mu m$ thick drift regions made of InN with the $n_0 = 1 \times 10^{17}\ ion/cc$ domains shown in Figure 5.8. Each data series corresponds to a different applied bias (and thus domain velocity v) as noted in the legend. The frequency of each data point was obtained by simulating devices of varying grating period P. The grating density was fixed at $\delta = 0.8$ for all devices. The SPR power density data shows that a $100\mu m$-wide bare device of this type could generate $2\mu W$ at 0.25 THz and $3.6nW$ at 1.8 THz. While the addition of antenna will be seen to significantly increase the SPR power density, the results indicate that it may be possible to find practical applications for bare devices with power output in this range.

Figure 5.9 illustrates the crux of the design tradeoffs encountered in considering frequency, SPR power density, and DC power consumption. At lower applied field, the DC power consumption is lower and the frequency is higher, but the SPR power density is lower. This is because the narrower domains remain effective in generating the maximum amount of SPR power possible from gratings of smaller period P than do the wider domains. Therefore defining the optimal characteristics of a Smith-Purcell terahertz source is expected to be an application-specific design exercise. In Section 6, suggestions are made for additional investigations that may prove useful for implementing Smith-Purcell devices into future integrated circuit designs.

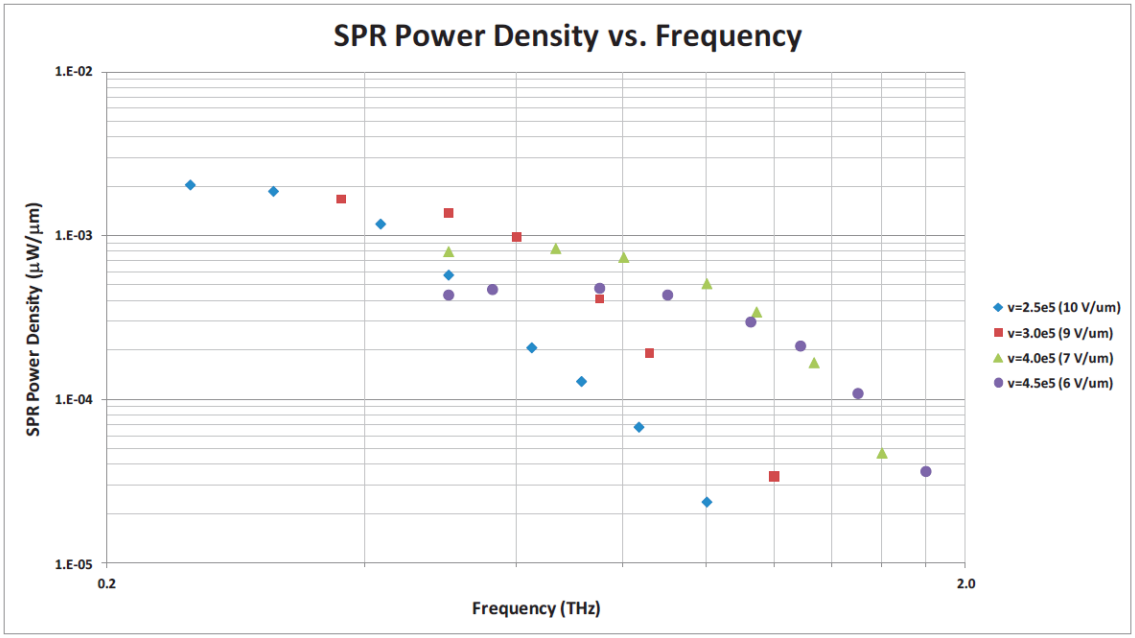

Figure 5.9: Frequency response using the domains of Figure 5.8. All bare devices have diode length $L = 5\mu m$ long and grating density $\delta = 0.8$. A $100\mu m$-wide bare device would thus generate $0.2\mu W$ at 0.25 THz and $3.6nW$ at 1.8 THz.

5.1.9 Size Ratio Analysis – Bare Devices

As discussed above, the physical mechanism responsible that generates SPR power in the Smith-Purcell device is induced current density moving across the grating teeth. It is found that the size ratio ξ defined in Equation (5.2) provides a useful figure of merit with which to describe this device property. Continuing the analysis of the bare devices from the previous section, the tooth widths ℓ for the devices used to compile Figure 5.9 ranged from $0.2 - 1.3\mu m$. The widths of the accumulation regions of the Gunn domains shown in Figure 5.8 range from $0.21 - 0.29\mu m$ as shown in Table 5.1. For fixed domain width a and decreasing tooth width ℓ corresponding to higher frequency, the decreasing values of ξ represent the smaller fraction of domain charge "captured" by the grating tooth. It is therefore expected that SPR power density approaches zero in the limit $\xi \to 0$ and increases with ξ up to some maximum value.

Assuming a fixed Gunn domain size and grating density δ, it is expected that there is some value of tooth width ℓ at which the induced image current becomes saturated at its maximum. As the grating period P is increased at fixed grating density δ, both the tooth width ℓ and the gaps between teeth grow. The induced current density is saturated and therefore the fixed current density is forced to generate SPR across a growing gap. Thus the SPR power density is expected to *decrease* slowly at very large values of ξ.

To test the above hypothesis and to determine the role of device geometry in SPR power density, the data from Figure 5.9 was recast. For each Gunn domain, the power density at each value of frequency was first normalized to its maximum value. Next, ξ values were calculated for each data point by using the accumulation width a of each Gunn domain from Table 5.1. Finally, the normalized SPR power density

plotted as a function of ξ to create the plot of Figure 5.10.

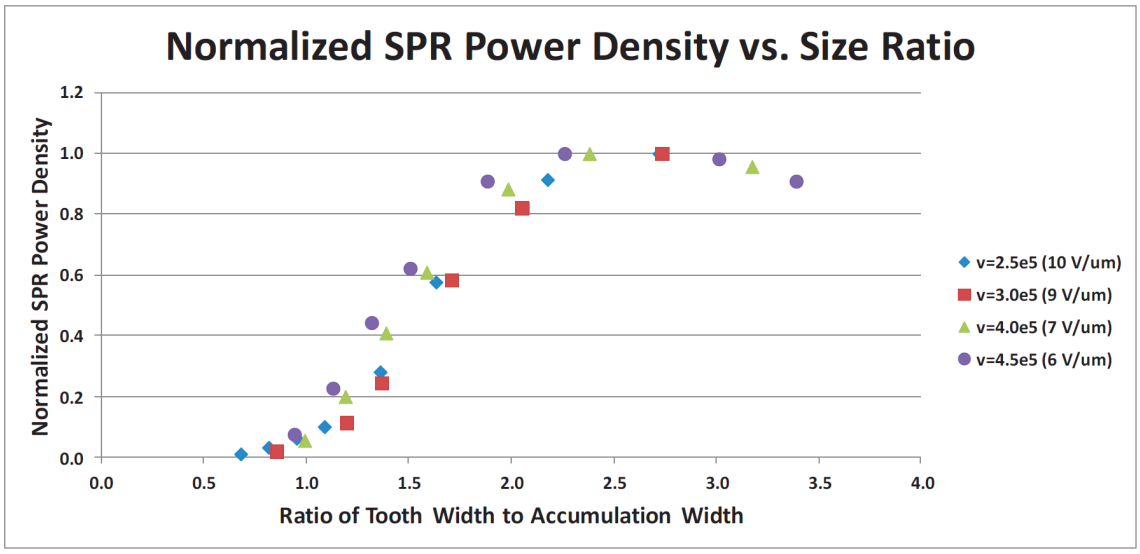

Figure 5.10: Power data of Figure 5.9 normalized to the peak power for each Gunn domain, then plotted as a function of the size ratio ξ defined in Equation (5.2).

Organizing the data in the geometric manner described above confirms the hypothesis that fixed induced current density across increasing tooth gap results in lower SPR power density at large values of size ratio ξ. Moreover, the power density versus size ratio data suggest the existence of a "universal" SPR power density model. The results for antenna devices discussed below are found to follow a "universal" model depending only on ξ and the integrated charge Q. The bare devices, however, do not cleanly correlate with Q scaling. At this time normalized power density and size ratio provide the cleanest model for bare devices. This clearly suggests that another factor is convolved with the data in Figure 5.10, and the most likely contributor is the nearest-neighbor tooth interactions discussed above. The full solution for bare device modeling is left to future researchers.

Most importantly, Figure 5.10 ties together the main ideas and results of the previous three Sections. The Gunn effect physics developed in Section 2 is directly tied to the Smith-Purcell physics developed in Section 3, using the simulation and theoretical methods developed in Section 4. Having thus presented the response of the bare Smith-Purcell device with respect to the design parameters and tying together the threads begun in the preceding Sections, the next topic evaluates the performance of Smith-Purcell devices with integrated antennas.

5.2 Performance of Devices With Antennas

It was shown above that since the radiating portion of the Smith-Purcell device is very short – on order of the (sub)micron grating period P – bare devices have low radiation resistance and thus low SPR power density. In order to set realistic expectations for the SPR power density achievable in future experimental work on Smith-Purcell THz devices, an antenna structure needs to be added to the bare device. Several variations of antenna design were briefly investigated, but only the antenna design used in this research was a half-wave dipole with solid metal arms.

The 2D device modeling methods covered previously are not readily adapted to the unique challenges of modern high-frequency antenna design. Developing the 3D modeling environment best-suited to antenna design was beyond the scope of the current research. Therefore is it recommended that a future research project be focused specifically on antenna optimization. In the simulation models, the arms of the Gunn diode are connected directly to the ends of the device, consistent with the usage of standard Gunn diodes to directly drive antennas.

During the course of this research, results were obtained from simulations covering a wide portion of design space. The Gunn diode length L, active thickness t, grating thickness g, spacer thickness b, and grating period P were varied, as discussed in

detail above for bare devices. The material type, bulk doping concentration, and applied bias (drift velocity) were also varied in order to change the Gunn domain profile. In order to standardize the antenna device design, the length of the Gunn diode L is chosen to be seven times the grating period P in all cases ($L = 7P$). The length of each arm of the dipole antenna is chosen to be one-quarter of a free-space wavelength minus half the Gunn diode length ($L/2$). The total antenna device length thus is always equal to one half the free-space wavelength.

The frequency response of four series of $5\mu m$-long bare devices with varying grating period P drift velocity v were presented in Figure 5.9. All devices had bulk doping concentration $n_0 = 1 \times 10^{17}\ ion/cc$. Over the frequency range $0.2 - 0.6$ THz, the lowest-frequency series of bare devices with drift velocity $v = 2.5 \times 10^5\ m/s$ had SPR power density in the range $3 \times 10^{-3}\ \mu W/\mu m$ to $3 \times 10^{-4}\ \mu W/\mu m$. This series of devices was selected to measure the impact of the dipole antenna on the SPR power density, as shown in Figure 5.11.

To create the plot, each of the bare device models was modified in the manner described above to convert it to a standard device. The SPR power density data was collected by the probe-point method described in detail above. Then the two sets of data were graphically matched by multiplying the power density of each bare device by the same constant. The multiplicative constant was selected by minimizing the average percent difference for the data values in the $0.5 - 1.0$ THz range as shown.

The intent of the matching exercise is simply to identify an order-of-magnitude estimate of the improvement made by the simple dipole antenna. It is found that a factor of 900 gives a reasonable match between bare and antenna device power densities over most of the frequency range. Having found that the antenna devices are able to significantly improve the SPR power density over that observed in bare devices, it is evident that technologically relevant radiated power can be generated

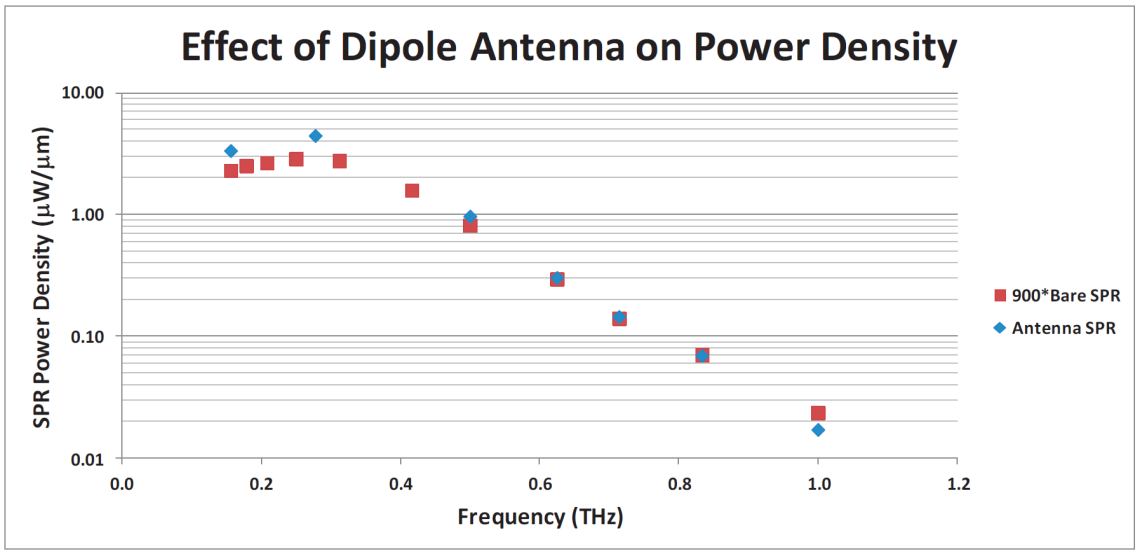

Figure 5.11: Adding half-wave dipole antennas to the bare devices of Figure 5.9 boosts their SPR power density by a factor of 900. It is noted that the "tooth-limited" low-frequency rolloff is observed for both bare and antenna devices.

from the Smith-Purcell THz device. Figure 5.11 indicates that a 100 μm-wide device of this design would generate $448\mu W$ of power at 0.3 THz and $1.7\mu W$ of power at 1.0 THz. The frequency versus power data for the antenna device displays the same low-frequency rolloff as was observed for bare devices. This supports the "tooth-limited" mechanism described above being the correct mechanism for this phenomenon.

5.2.1 Power vs. Bulk Doping Concentration

Figure 5.8 showed how the shape of the Gunn domain varied with applied bias for n-doped InN with bulk doping concentration of 1×10^{17} ion/cc. As was mentioned in Section 2, bulk doping concentration has a strong effect on the shape of the Gunn domain – higher doping concentration gives narrower and higher domains, both of which are advantageous for higher SPR power and flatter frequency response. The design tradeoff is that the DC power of the planar Gunn diode increases, which

increases the waste heat that must be managed.

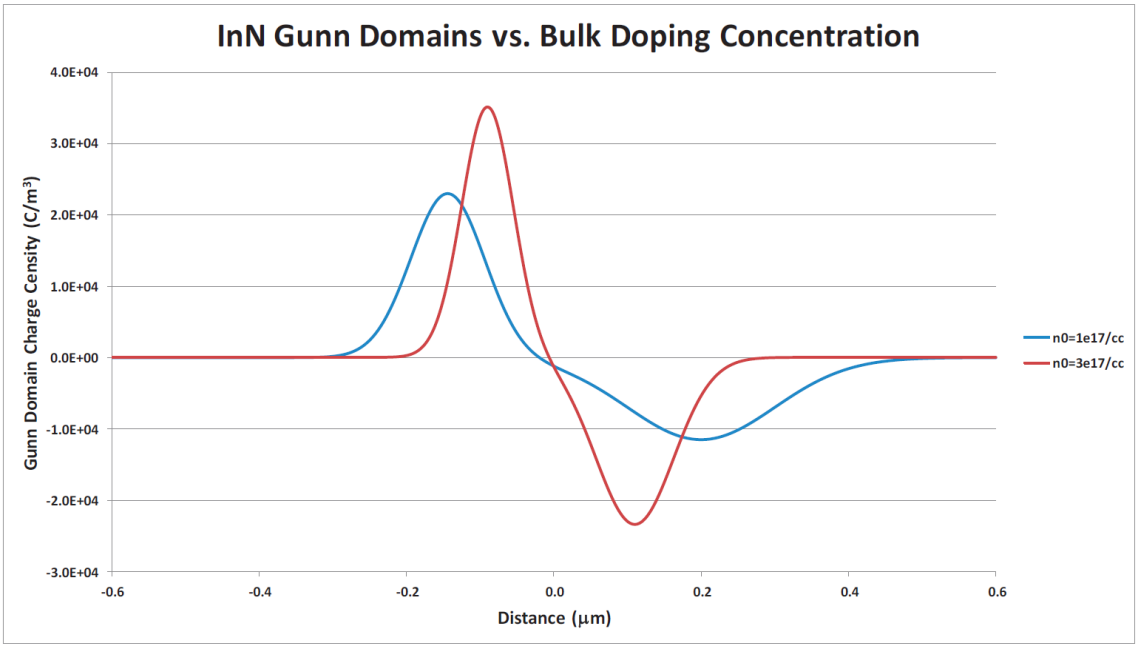

Figure 5.12: InN Gunn domain profiles for applied field 10 $V/\mu m$ ($v = 2.5\times10^5\ m/s$) at different bulk doping concentrations n_0. Higher doping provides a favorable Gunn domain profile, but also generates more DC current (thus more heat).

Figure 5.12 shows the effect of increasing n_0 from $1\times10^{17}\ ion/cc$ to $3\times10^{17}\ ion/cc$ in InN at constant applied electric field $E = 10\ V/\mu m$. A complete presentation of the properties of the Gunn domains in the higher-doped material will be given below, after the effect of doping on power density is more fully investigated. In the previous case where the domain profile was changed via the applied field E, narrower domains were obtained by reducing the applied field. The field-narrowed domains had higher velocity v but lower peak charge density ρ_{max} and lower integrated charge Q.

Changing the doping by a small amount (less than an order of magnitude) does not make appreciable changes in the drift velocity. In Figure 5.12, both domains

have velocity $v = 2.5 \times 10^5\ m/s$. Higher doping is seen to *decrease* the domain width – the accumulation widths are $a_1 = 0.29\mu m$ and $a_2 = 0.20\mu m$, respectively, for the wide and narrow domains. This is expected to allow the entire domain to induce image charge on narrower grating teeth as seen previously. A size ratio analysis for the antenna devices will be presented below. Finally, the higher doping is expected to provide a performance increase due to the presence of extra n-type doping which *increases* the peak charge density. The domain characteristics of Figure 5.12 as well as the data for grating period P, frequency, tooth width ℓ, size ratios and SPR power density used for Figure 5.13 is listed in Table 5.2.

Table 5.2: Data for the Gunn domains of Figure 5.12 with $a_1 = 0.29\mu m$ and $a_2 = 0.20\mu m$ and the power and size data used for Figures 5.13 and 5.14.

$P\ (\mu m)$	$f\ (THz)$	$\ell\ (\mu m)$	δ	$\xi_1 = \ell/a_1$	$\xi_2 = \ell/a_2$	$n_0 = 1 \times 10^{17}$ SPR $(\mu W/\mu m)$	$n_0 = 3 \times 10^{17}$ SPR $(\mu W/\mu m)$
1.60	0.16	1.28	0.80	4.34	6.31	3.37	
0.90	0.28	0.72	0.80	2.44	3.55	4.48	3.95
0.50	0.50	0.40	0.80	1.36	1.97	0.98	3.40
0.40	0.63	0.32	0.80	1.08	1.58	0.31	2.04
0.35	0.71	0.28	0.80	0.95	1.38	0.15	1.12
0.30	0.83	0.24	0.80	0.81	1.18	0.07	0.44
0.25	1.00	0.20	0.80	0.68	0.99	0.02	0.10

The SPR power density data confirms the above expectations, as shown in Figure 5.13. Identical device geometries are used for both the higher and lower doping values. The grating period P is reduced at constant domain velocity $v = 2.5 \times 10^5\ m/s$ and constant grating density $\delta = 0.8$. As discussed above, the diode length L was scaled as $L = 7P$, and the length of the antenna arms was scaled to maintain total device length $\lambda/2$. The SPR power density data was collected using the probe-point method

and measured at a distance $\rho = 3\lambda$ above the device midpoint as was done for the bare device results discussed above.

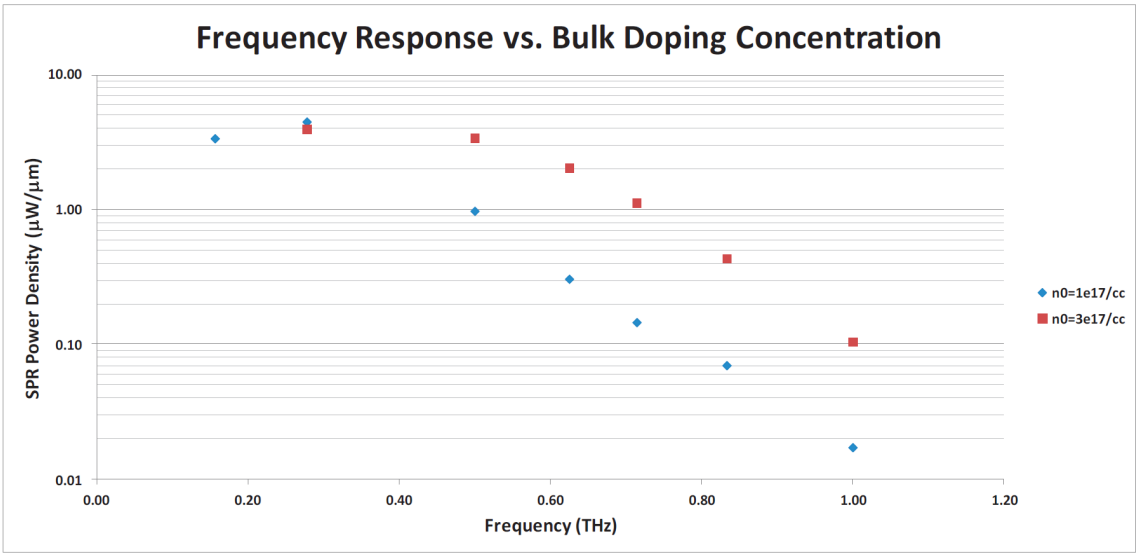

Figure 5.13: Increasing the bulk doping concentration n_0 improves the frequency response, as expected from the domain profiles in Figure 5.12.

Figure 5.13 shows that at low frequency both the wide and narrow pulse produce similar SPR power density. This is again the "tooth-limited" case discussed previously in which the image charge induced by the domain is small compared to the total capacity of the tooth. As the grating period P is reduced to achieve higher frequency, the narrow domain in the higher-doped material consistently generates higher SPR power density than the wide domain in the lower-doped material. This behavior is again understood by plotting the SPR power density versus the size ratio ξ – the tooth width ℓ divided by the accumulation width a defined in Equation (5.2).

5.2.2 Size Ratio Analysis – Antenna Devices

It was found that the SPR power density for the many $n_0 = 1 \times 10^{17}$ InN bare devices approximately obeyed the "universal" SPR power density relationship shown in Figure 5.10. It was noted in the discussion of bare devices that the SPR power density values for each field-determined domain profile needed to be normalized to the peak power generated in the series of devices. The hypothesis is that the (very short) radiative length of the bare device leads to an heightened dependence on within-grating interactions that are not comprehended by the current theory.

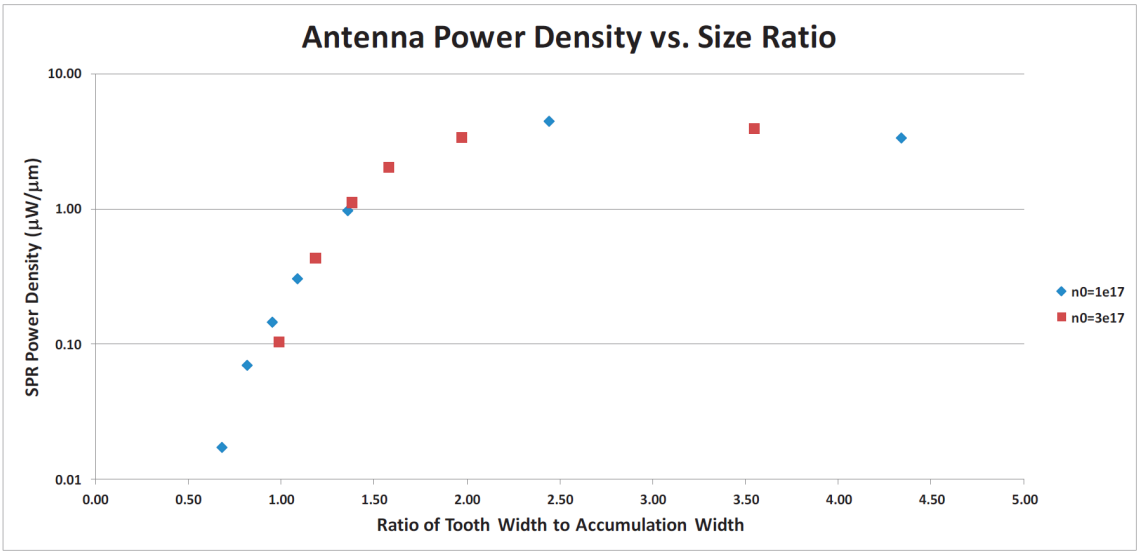

Figure 5.14: Size analysis of the SPR power density data from Figure 5.13. Note that the antenna devices do *not* require normalized power as did the bare devices presented in Figure 5.10.

Therefore, the data for the two domains just considered in the above comparison of antenna devices with different bulk doping concentration are analyzed in the same manner to determine the extent to which size ratio ξ plays a role in describing the

SPR power density. It is found that the antenna devices indeed obey a similar relationship between SPR power density and the size ratio ξ.

Figure 5.14 shows the result of performing the size ratio analysis for the antenna devices with different bulk doping concentrations using the data in Table 5.2. Unlike the bare devices, however, *the antenna devices do not require SPR power density normalization*. This supports the hypothesis made above that the effective device length interacts with the domain properties and device geometry to spread the power data in a manner not captured solely by ξ.

In the following section the properties of the higher-doped material are investigated in detail, and it is shown that a simple addition to the current size ratio analysis appears to fully describe the operation of the Smith-Purcell antenna devices.

5.2.3 Best-Case Antenna Power Results

Table 5.3: Physical characteristics of InN Gunn domains with $n_0 = 3 \times 10^{17}$.

E $(V/\mu m)$	v $(10^5 m/s)$	a (μm)	Q_{int} (C/m^2)	ρ_{max} (C/m^3)	ρ_{min} (C/m^3)
10.40	2.50	0.202	3.01×10^{-3}	35118	-23422
8.80	3.00	0.158	1.91×10^{-3}	28459	-20346
7.70	3.50	0.140	1.36×10^{-3}	22424	-17081
6.70	4.00	0.132	9.90×10^{-4}	17000	-13541
5.90	4.50	0.138	6.65×10^{-4}	11200	-9660

It was demonstrated above that a slight increase in bulk doping concentration n_0 can make a significant improvement in SPR power density. Therefore the final set of InN simulation experiments focus on the best-case scenario with $n_0 = 3 \times 10^{17}$ ion/cc. The same set of applied field conditions as for the $n_0 = 1 \times 10^{17}$ ion/cc case were

repeated. An extra field condition with velocity $v = 3.5 \times 10^5\ m/s$ was added, as shown in Table 5.3. The domains are plotted in Figure 5.15.

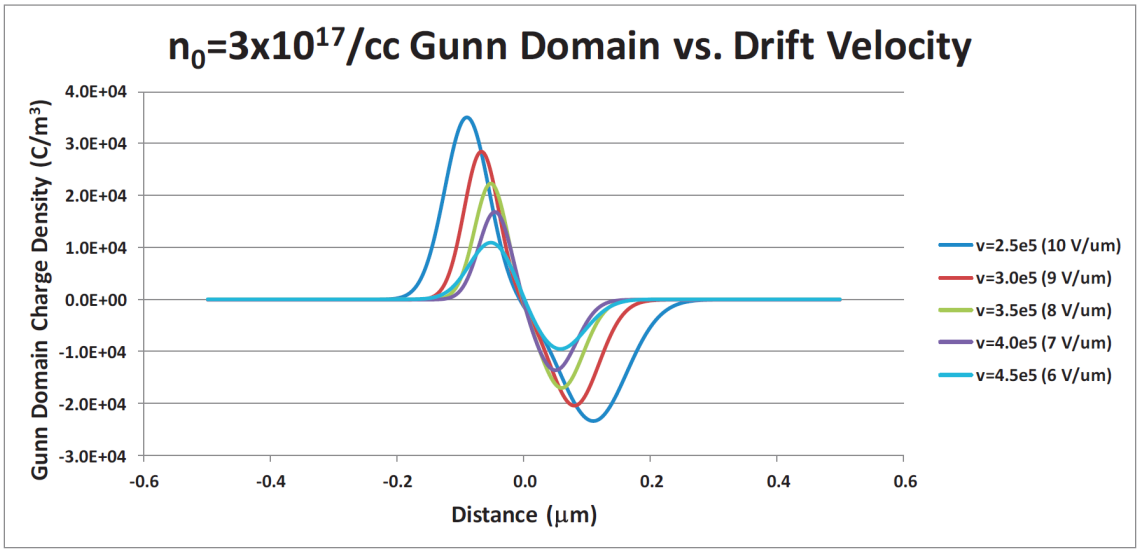

Figure 5.15: Gunn domains in higher-doped InN ($n_0 = 3 \times 10^{17}\ ion/cc$) at several drift velocities – compare to $n_0 = 1 \times 10^{17}\ ion/cc$ domains in Figure 5.8.

The same experimental conditions and design criteria were followed as has been the case in previous cases. The SPR power density was found to behave in a manner now seen to be typical for the Smith-Purcell device – strong high-frequency rolloff, a peak at moderately low frequency, and slight tooth-limited low-frequency rolloff. The SPR power density data is plotted in Figure 5.16 as a function of frequency and domain velocity. The peak power density is found to be 3.65 $\mu W/\mu m$ at 0.28 THz.

The highest device frequency was 2.5 THz, with power density 0.01 $\mu W/\mu m$. Assuming a 100 μm-wide device, the SPR power generated across the $0.28 - 2.5$ THz range definitely has technological relevance – 0.4 mW at 0.28 THz and 1 μW at 2.5THz. The data of Figure 5.15 were in fact used to create Figure 1.4 in Section 1

by selecting the maximum SPR power density at each frequency tested.

Since the Smith-Purcell device is intended to be incorporated into an integrated circuit, it is expected that power from multiple devices can readily be combined, making it a very attractive solution to the problem of building compact room-temperature sources of THz radiation. It was mentioned above that an addition to the size ratio analysis made it possible to describe a simple "universal scaling law" for the SPR power density of the Smith-Purcell antenna device. In the following section, it is shown that the integrated charge density Q is the key factor required.

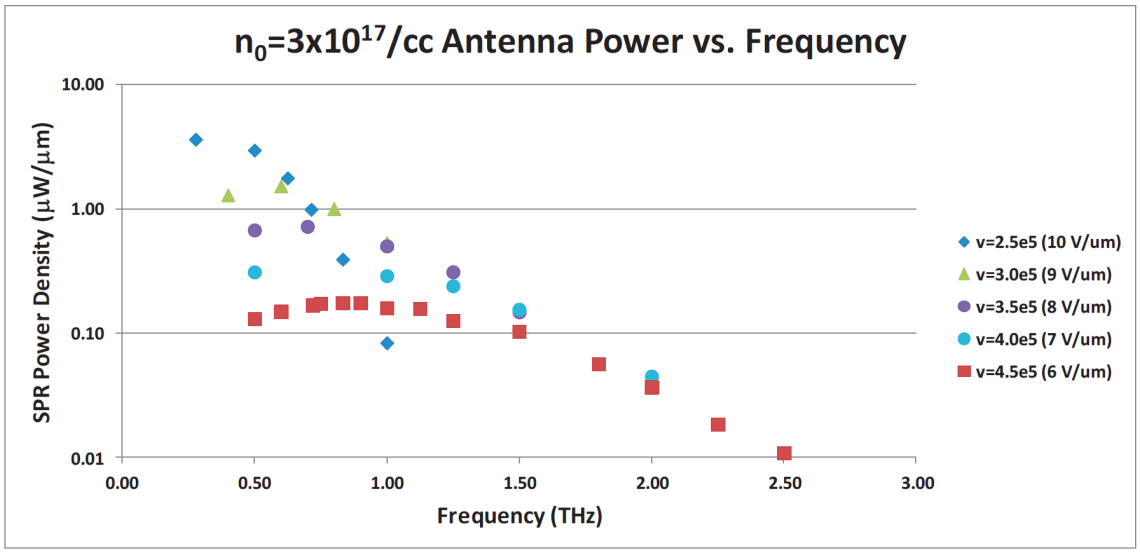

Figure 5.16: Frequency performance for the 34 antenna devices used to determine the efficacy of the Smith-Purcell concept from mm-wave into the low THz range. A 100 μm device would generate 365 μW at 0.28THz and 1μW at 2.5THz.

5.2.4 Antenna Power Density Scaling

In the discussion of bare devices, the definition of the size ratio ξ suggested that the SPR power density data might be made to fall onto a "universal curve". By

plotting the *normalized* power density for each value of domain velocity v (or equivalently, applied field E) corresponding to a different Gunn domain profile. Attempts to fit the unnormalized power density data for bare devices to a simple model involving ξ, Q, or v were unsuccessful and this problem remains unsolved. It is conjectured if the theory of device operation is improved enough to comprehend medium-scale effects, then the short-device effects will be correctly resolved.

Subsequent size analysis of *antenna* devices with different bulk doping concentrations at the same applied field and similar values of integrated charge Q were indeed able to be fit to a single curve as shown in Figure 5.14. Next, a large set of 34 different simulation experiments were run across the five different Gunn domain profiles shown in Figure 5.15 and whose physical properties are tabulated in Table 5.3. It was found that a simple plot of SPR power density as a function of ξ resulted in a family of curves – one for each domain, similar to what was observed in Figure 5.14.

At the beginning of this section, Figure 5.1 showed that SPR power density increases as the square of the integrated charge density Q^2. The bare devices did not scale with Q^2 as expected, but it *was* possible to scale the SPR power density of the antenna devices by this method. The Q^2 scaling was done in terms of the largest domain ($v = 2.5 \times 10^5\ m/s$). Its integrated charge value from Table 5.3 was defined as $Q_0 = 3.01 \times 10^{-3}\ C/m^2$. The scaled SPR power density values SPR_{scale} of subsequent domains were scaled according to:

$$SPR_{scale} = SPR_{act}\left(\frac{Q_0}{Q_i}\right)^2 \tag{5.3}$$

where the subscript i cycles through the four domains in Table 5.3. The scaled SPR power density values are then plotted as a function of the size ratio ξ, which results

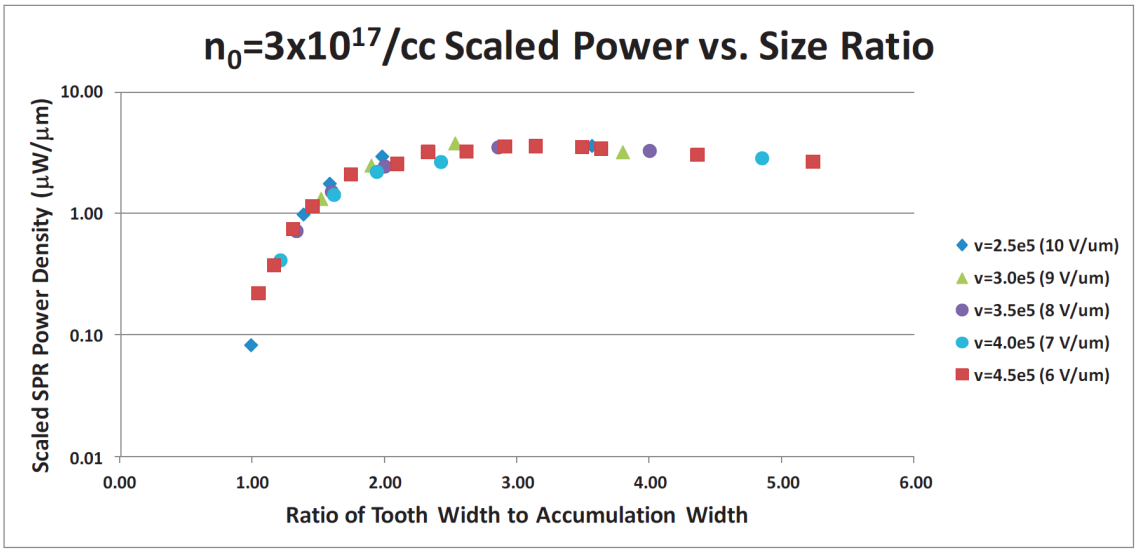

Figure 5.17: Data from the 34 ($n_0 = 3 \times 10^{17}$ ion/cc) antenna devices in Figure 5.16 plotted by size ratio. When the SPR power density is scaled by the ratio of the square of the integrated charge in the domain, a "universal curve" is realized.

in Figure 5.17. With the high quality of fit found by using Equation (5.3), it is concluded that the operation of the Smith-Purcell antenna device is now reasonably well understood, and that the goals set out in the research proposal have been fully met.

6. CONCLUSIONS AND SUGGESTIONS FOR FUTURE WORK

The combination of the transferred-electron (Gunn) effect and the Smith-Purcell effect have been shown to offer a novel and compelling approach to the fabrication of future millimeter-wave and terahertz electronic devices, as illustrated in Figure 1.1. The theory of operation is presented and has been demonstrated to be reasonably well-understood. Computer simulations of the device agree well with theory, and design experiments have explored the capabilities of the approach. It is found that the performance of the Smith-Purcell THz device compares favorably to other semiconductor THz sources (Figure 1.4).

The main conclusion to draw from this research is that the simplicity of construction of the Smith-Purcell THz device makes it a very attractive alternative to more established high-frequency solid-state devices, to which its performance is comparable.

The primary suggestion for future work is to experimentally confirm the high-frequency responses predicted in this Dissertation.

6.1 Summary and Conclusions

The Introduction (Section 1) described the motivation for (and challenges of) exploiting the unique physics available in the frequency range $0.3 - 3.0$ THz. Examples were given of practical application spaces, such as spectroscopic analysis, which exhibit a compelling need for compact THz sources with at least microwatt power output levels. A brief survey of current state-of-the-art semiconductor THz sources was presented in which the technical limitations of the various approaches were noted.

Section 1 made the case for the conclusion that *clear paths to manufacturability and high yield are key evaluation criteria for any semiconductor device.* This is due

to the practical reality that *unit cost* has historically determined the extent to which new semiconductor technologies have gained widespread application. Figure 1.1 illustrates the proposed concept for a novel room-temperature semiconductor device capable of generating technologically relevant amounts of high-frequency electromagnetic radiation, in which the transferred-electron (or Gunn) effect is used to create compact packets of moving space charge. The moving charge packets (Gunn domains) travel under and very near to a metallic grating with (sub)micron dimensions, which cause induced image currents to flow in the grating teeth. These periodic image currents then radiate via the Smith-Purcell effect with frequency in the $0.25 - 2.5$ THz range.

Section 2 provided an explanation of the transferred-electron effect, which is also eponymously known as the Gunn effect for the first researcher to report experimental evidence of the phenomenon. The Gunn effect is observed as a spontaneous change in the charge transport properties of certain semiconductor crystals. The effect was theoretically predicted by Ridley, Watkins, and Hilsum. They predicted that direct-gap bandgap materials whose band diagrams have satellite valleys with effective mass higher than that found in the main valley would experience negative differential resistivity (NDR) at high applied electric field. They predicted that the onset of NDR in such a material would produce an instability in the conduction current and electric field distribution in the crystal.

This instability was predicted to manifest as a free-traveling dipole layer (called a domain) moving through the crystal, and that the cyclic production of these dipole domains would cause the spontaneous DC-to-RF behavior observed by Gunn. Butcher, Fawcett, and Hilsum provided a straightforward numerical method to calculate the physical properties of the domain. The main conclusion from Section 2 is that *an accurate implementation of the Butcher-Fawcett domain-calculation method*

is used for this research.

Section 3 provided the theoretical background for the Smith-Purcell effect, in which a uniformly-moving charge generates electromagnetic radiation when it passes near to a metallic diffraction grating. The distinction was made between spontaneous (incoherent single-electron) and stimulated (coherent many-electron) Smith-Purcell radiation. It was noted that spontaneous Smith-Purcell radiation had previously been observed in semiconductors, but only in very pure GaAs samples at low temperature, with extremely low power. The connection was made that the Gunn effect potentially provided a method by which stimulated Smith-Purcell radiation could be generated from a semiconductor device.

First-principles calculations were made of the Smith-Purcell radiation for the special case of a semiconductor device – non-relativistic electron speed and extremely small impact parameter (charge-grating distance). It was shown that under these conditions there was an exact closed-form solution for the vector potential that accurately captured the expected behavior of a single charge, as presented in Appendix A. The primary conclusion from Section 3 was that *an exact theoretical expression for the Smith-Purcell electric field of a single charge was known.*

Section 4 introduced the computer simulation methodology in detail and investigated to what extent simulation agreed with theory. It was shown that superposition of the electric field allowed the single-charge theory of Section 3 to be applied to the Gunn domains calculated with the methods of Section 2. When these analytic methods were combined to calculate the radiated electric field, it was found that qualitative agreement with simulation was very good. It was then demonstrated that calibrations of the analytic model resulted in reasonable quantitative agreement with simulation. The main conclusion from Section 4 was that *theory and simulation agreed well enough for the purposes of this research, but that opportunities exist for*

future improvement in both aspects.

Section 5 presented the results of the research, both for bare Smith-Purcell THz devices and for devices with integrated dipole antennas. The Smith-Purcell radiation (SPR) power density was studied as a function of all the design parameters relevant to future experimental work. Non-physical experiments in which the Gunn domain was artificially manipulated showed that the power density varied as the fourth power of domain velocity v^4 and as the square of the integrated domain charge Q^2. This led to the first conclusion that *The (sub)micron radiative portion of the Smith-Purcell device behaves as a point Larmor dipole source.*

Next it was found that the power density of the bare devices varied with the square of the diode length L^2, which is the expected behavior for a short dipole. However, this discovery confirmed the previous conclusion that the theoretical methods need improvement. A sharper conclusion is thus reached that *the single-charge theory does not correctly "comprehend" the length of the grating to which it is applied.* Analysis of the length dependence of the bare devices allowed the RF-to-THz conversion efficiency to be estimated in the range $0.3\% - 3.0\%$, which is comparable with the DC-to-RF conversion of regular Gunn diodes operating in the dipole-transit oscillation mode.

The SPR power density was found to decrease exponentially with increasing spacer thickness b – the measure of the impact parameter – the charge-distance separation mentioned above. *It it concluded that the solid-state device displays the identical response to impact parameter to that of traditional vacuum Smith-Purcell devices.* The power density response to diode thickness showed that there is an optimal thickness above which the power density declines.

Compiling the results of several systematic studies on bare devices led to the analysis of power density as a function of the size ratio $\xi = \ell/a$ of the grating tooth

ℓ and the domain accumulation width a. The primary conclusions from these results are that *bare devices may find some practical applications and that the bare devices have a significant sensitivity to diode length.*

The final portions of Section 5 investigate the SPR power density response of Smith-Purcell devices with built-in half-wave dipole antennas. It was found that the antenna devices do not have the severe sensitivity to device length seen in the bare devices. As a result, it was possible to discover the "universal scaling law" involving only the size ratio and the integrated domain charge. The main conclusion is that *Smith-Purcell devices can be designed with hundreds of* μW *at* 0.3 *THz and in excess of* 1 μW *at* 2.5 *THz.*

6.2 Suggestions for Future Research

The scope of research presented in this Dissertation demonstrates the viability of a simple room-temperature, solid-state semiconductor device that can operate into the terahertz range. It can be implemented in a very straightforward manner into any existing compound-semiconductor process technology. It is expected that by using novel epitaxial deposition techniques it can also readily be incorporated in to mainstream silicon CMOS processes as well. Any development path from device concept to mainstream manufacturing necessarily implies the existence of a complex (and usually arduous) sequence of projects. Therefore it is appropriate that in closing, a few of the highest-impact opportunities be highlighted.

The most obvious project to undertake is to experimentally verify the predictions of this research. A planar Gunn diode is arguably the single easiest semiconductor device in the world to build – it's a block with two contacts. Therefore it should be extremely simple to fabricate a planar Gunn diode with a thin dielectric cover and a patterned metallic grating. The literature provides many examples of how

to measure the domain characteristics. The methods developed in this research can readily convert those measurements into the expected SPR power density generated by the device. Moreover, measurement methods for the empirical radiated power density are well-known for all frequencies accessible to the Smith-Purcell device. It is hoped that within the next 1-2 years that proof of concept is established.

The simple analytic model correctly demonstrates the basic physical mechanisms of device operation, as discussed in Section 5. Nonetheless, it was shown that the "toy model" developed herein is insufficient to quantitatively predict the output electric field under all conditions. Therefore it may be of interest for future researchers to return to the basic assumptions laid out in Sections 2 and 3 to develop a more sophisticated device model. Ideally, the need for a separate equal-areas solver would be eliminated in favor of a first-principles multiphysics simulator working in conjunction with a process simulator. This "bottoms-up" integration would be extremely useful by accurately accounting for subtle changes in doping profile and local field gradients due to process conditions.

Assuming that the Smith-Purcell device concept is experimentally verified, it is expected that it will eventually be incorporated into a mainstream manufacturing process flow. In this case, it will be expedient to develop a set of design tools adequate for accurately modeling this device. The current simple model cannot automatically determine the radiation resistance for a given set of device conditions. Therefore the only current recourse is either to perform iterative electromagnetic simulation (as has been done in this scope of research) or empirically determine the actual performance by fabricating and testing a number of devices. Therefore "top-down" integration with a circuit simulator would provide useful insight into how best to make practical design choices.

As indicated in Sections 4 and 5, the current theoretical model "is not aware" of

the size of the device in which it is embedded. Having a model that can comprehend the mesoscale environment would prove useful for determining the tooth-to-tooth variation in electric field of a given device. It is expected that incorporating the Smith-Purcell device into practical integrated circuits will *require* this level of detail.

For example, this research has shown that the time-domain profile of the electric field can be tailored by device design. The "spikiness" of the waveform generated by the device determines the amount of harmonic content the wave contains. Depending on the circuit in which the device is placed, it may prove advantageous to accept lower power density in order to reduce off-frequency components that can be fed into an amplifier and increase noise.

All these opportunities hinge upon the main conclusion that this concept be aggressively pursued as an experimental project. In closing, it is hoped that this work find practical use for future mainstream applications in the coming terahertz age.

REFERENCES

[1] D. D. Smith and A. Belyanin, "Room-temperature semiconductor coherent Smith-Purcell terahertz sources," *Appl. Phys. Lett.*, vol. 98, no. 6, pp. 063 501–063 504, Feb. 2011.

[2] C. Hilsum, "Transferred Electron Amplifiers and Oscillators," *Proc. IRE*, vol. 50, no. 2, pp. 185–189, Feb. 1962.

[3] B. K. Ridley and T. B. Watkins, "The possibility of negative resistance effects in semiconductors," *Proc. Phys. Soc.*, vol. 78, no. 2, pp. 293–304, Aug. 1961.

[4] J. B. Gunn, "Instabilities of Current in III–V Semiconductors," *IBM J. Res. Develop.*, vol. 8, no. 2, pp. 141–159, Apr. 1964.

[5] S. J. Smith and E. M. Purcell, "Visible Light from Localized Surface Charges Moving across a Grating," *Phys. Rev.*, vol. 92, no. 4, p. 1069, Nov. 1953.

[6] J. C. Wiltse, "History of Millimeter and Submillimeter Waves," *IEEE Trans. Microw. Theory Tech.*, vol. 32, no. 9, pp. 1118–1127, Sept. 1984.

[7] P. H. Siegel, "Terahertz technology," *IEEE Trans. Microw. Theory Tech.*, vol. 50, no. 3, pp. 910–928, Mar. 2002.

[8] G. P. Williams, "Filling the THz Gap," *Rep. Prog. Phys.*, vol. 69, no. 2, pp. 301–306, Dec. 2005.

[9] M. Cooke, "Filling the THz gap with new applications," *Semiconductor Today*, vol. 2, no. 1, pp. 39–43, Feb. 2007.

[10] P. F. Taday, "Applications of terahertz spectroscopy to pharmaceutical sciences," *Philos. Trans. R. Soc. London, Ser. A*, vol. 362, no. 1815, pp. 351–364, Feb. 2004.

[11] J. M. Chamberlain, "Where optics meets electronics: recent progress in decreasing the terahertz gap," *Philos. Trans. R. Soc. London, Ser. A*, vol. 362, no. 1815, pp. 199–213, Feb. 2004.

[12] D. Dragoman and M. Dragoman, "Terahertz fields and applications," *Prog. Quant. Electron.*, vol. 28, no. 1, pp. 1–66, Jan. 2004.

[13] G. P. Gallerano, "Overview of Terahertz Radiation Sources," in *Proc. 2004 FEL Conf.*, Trieste, Italy, pp. 216–221.

[14] M. Koch, "Terahertz Technology: A Land to Be Discovered," *Opt. Photonics News*, vol. 18, no. 3, pp. 20–25, Mar. 2007.

[15] S. Staff, "The Early Years of SAS," *Appl. Spectrosc.*, vol. 62, no. 9, pp. 5–14, Sept. 2008.

[16] T. W. Crowe, T. Globus, D. L. Woolard, and J. L. Hesler, "Terahertz sources and detectors and their application to biological sensing," *Philos. Trans. R. Soc. London, Ser. A*, vol. 362, no. 1815, pp. 365–377, Feb. 2004.

[17] M. K. Choi, A. Bettermann, and D. W. van der Weide, "Potential for detection of explosive and biological hazards with electronic terahertz systems," *Philos. Trans. R. Soc. London, Ser. A*, vol. 362, no. 1815, pp. 337–349, Feb. 2004.

[18] C. M. Armstrong, "The Truth About Terahertz," *IEEE Spectrum*, Aug. 2012. [Online]. Available: http://spectrum.ieee.org/aerospace/military/the-truth-about-terahertz/

[19] S. A. Lynch, D. J. Paul, P. Townsend, G. Matmon, Z. Suet, R. W. Kelsall, Z. Ikonic, P. Harrison, J. Zhang, D. J. Norris, A. G. Cullis, C. R. Pidgeon, P. Murzyn, B. Murdin, M. Bain, H. S. Gamble, M. Zhao, and W. Ni, "Toward

Silicon-Based Lasers for Terahertz Sources," *IEEE J. Sel. Topics Quantum Electron.*, vol. 12, no. 6, pp. 1570–1578, Nov. 2006.

[20] S. M. Sze, *Physics of Semiconductor Devices*, 2nd ed. Wiley-Interscience, 1981.

[21] F. Capasso, R. Paiella, R. Martini, R. Colombelli, C. Gmachl, T. L. Myers, M. S. Taubman, R. M. Williams, C. G. Bethea, K. Unterrainer, H. Y. Hwang, D. L. Sivco, A. Y. Cho, A. M. Sergent, H. C. Liu, and E. A. Whittaker, "Quantum cascade lasers: Ultrahigh-speed operation, optical wireless communication, narrow linewidth, and far-infrared emission," *IEEE J. Quantum Electron.*, vol. 38, no. 6, pp. 511–532, June 2002.

[22] G. Matmon, D. J. Paul, L. Lever, M. Califano, Z. Ikonic, R. W. Kelsall, G. Isella, H. von Kanel, E. Muller, and A. Neels, "Si/SiGe quantum cascade superlattice designs for terahertz emission," *J. Appl. Phys.*, vol. 107, no. 5, pp. 053 109–053 116, Mar. 2010.

[23] J. Faist, L. Ajili, G. Scalari, M. Giovannini, M. Beck, M. Rochat, H. Beere, A. G. Davies, E. H. Linfield, and D. Ritchie, "Terahertz quantum cascade lasers," *Philos. Trans. R. Soc. London, Ser. A*, vol. 362, no. 1815, pp. 215–231, Feb. 2004.

[24] G. Scalari, C. Walther, J. Faist, H. Beere, and D. Ritchie, "Electrically switchable, two-color quantum cascade laser emitting at 1.39 and 2.3 THz," *Appl. Phys. Lett.*, vol. 88, no. 14, pp. 141 102–141 105, Apr. 2006.

[25] Q. Hu, B. S. Williams, S. Kumar, A. W. M. Lee, Q. Qin, J. L. Reno, H. C. Liu, and Z. R. Wasilewski, "Terahertz quantum cascade lasers and real-time T-ray imaging," in *Future Trends in Microelectronics: Up the Nano Creek*. Hoboken, NJ: Wiley-IEEE Press, 2007, ch. 31, pp. 347–358.

[26] J. R. Freeman, O. P. Marshall, H. E. Beere, and D. A. Ritchie, "Electrically switchable emission in terahertz quantum cascade lasers," *Opt. Express*, vol. 16, no. 24, pp. 19 830–19 835, Nov. 2008.

[27] R. Borges, "Gallium nitride electronic devices for high-power wireless applications," RF Design, Tech. Rep., Sept. 2001.

[28] J. Wu, "When group-III nitrides go infrared: New properties and perspectives," *J. Appl. Phys.*, vol. 106, no. 1, pp. 011 101–28, July 2009.

[29] C. Sevik and C. Bulutay, "Simulation of Millimeter-Wave Gunn Oscillations in Gallium Nitride," *Turk. J. Phys.*, vol. 28, pp. 369–377, Nov. 2004.

[30] R. F. Macpherson, G. M. Dunn, and N. J. Pilgrim, "Simulation of gallium nitride Gunn diodes at various doping levels and temperatures for frequencies up to 300 GHz by Monte Carlo simulation, and incorporating the effects of thermal heating," *Semicond. Sci. Tech.*, vol. 23, no. 5, pp. 055 005–1–7, May 2008.

[31] I. P. Storozhenko and Y. V. Arkusha, "The Generation by Gunn Diodes Based on the GaN, InN, and AlN TED's in Biharmonic Regime," in *IEEE 2010 5th Int. Conf. on Ultrawideband and Ultrashort Impulse Signals*, Sevastopol, Ukraine, pp. 226–227.

[32] T. Gonzalez, I. de la Torre, D. Pardo, A. M. Song, and J. Mateos, "THz Generation Based on Gunn Oscillations in GaN Planar Asymmetric Nanodiodes," in *IEEE 2010 22nd Int. Conf. Indium Phosphide and Related Materials*, Kagawa, Japan, pp. 1–4.

[33] M. Lebby, A. Clark, and G. Ding, "Rare earth oxides: A great intermediary for GaN on large-area silicon," *Compound Semiconductor*, vol. 18, no. 5, pp. 37–41, July 2012.

[34] ——, "Crystalline Rare Earth Oxide Technology Primer," Translucent, Inc., Tech. Rep., 2012.

[35] J. G. Fiorenza, J. Park, J. Hydrick, J. Li, M. Curtin, M. Carroll, and A. Lochtefeld, "Aspect Ratio Trapping: An Enabling Technology for Ge and III-V MOSFET Integration," *ECS Trans.*, vol. 33, no. 6, pp. 964–976, Oct. 2010.

[36] Z. Cheng, J. Park, J. Bai, J. Li, J. Hydrick, J. Fiorenza, and A. Lochtefeld, "Aspect ratio trapping heteroepitaxy for integration of germanium and compound semiconductors on silicon," in *IEEE 2008 9th Int. Conf. Solid-State and Integrated-Circuit Technology*, Beijing, China, pp. 1425–1428.

[37] R. Krithivasan, Y. Lu, J. D. Cressler, J. Rieh, M. H. Khater, D. Ahlgren, and G. Freeman, "Half-terahertz operation of SiGe HBTs," *IEEE Electron Device Lett.*, vol. 27, no. 7, pp. 567–569, July 2006.

[38] R. Appleby, "Passive millimetre-wave imaging and how it differs from terahertz imaging," *Philos. Trans. R. Soc. London, Ser. A*, vol. 362, no. 1815, pp. 379–393, Feb. 2004.

[39] L. Maurer, G. Haider, and H. Knapp, "77 GHz SiGe based bipolar transceivers for automotive radar applications – An industrial perspective," in *IEEE 2011 9th Int. New Circuits and Systems Conf.*, Bordeaux, France, pp. 257–260.

[40] M. Jahn, K. Aufinger, T. F. Meister, and A. Stelzer, "125 to 181 GHz fundamental-wave VCO chips in SiGe technology," in *IEEE 2012 Radio Frequency Integrated Circuits Symp.*, Montreal, Canada, pp. 87–90.

[41] M. Koch, "Terahertz Communications: A 2020 vision," in *Terahertz Frequency Detection and Identification of Materials and Objects*. Springer Netherlands, 2007, vol. 19, pp. 325–338.

[42] H. Sugiyama, S. Suzuki, and M. Asada, "Resonant-tunneling-diode Terahertz Oscillator Based on Precisely Controlled Semiconductor Epitaxial Growth Technology," *NTT Technical Review*, vol. 9, no. 10, pp. 1–7, Oct. 2011.

[43] S. Suzuki, M. Asada, A. Teranishi, H. Sugiyama, and H. Yokoyama, "Fundamental oscillation of resonant tunneling diodes above 1 THz at room temperature," *Appl. Phys. Lett.*, vol. 97, no. 24, pp. 242 102–242 105, Dec. 2010.

[44] W. Prost, V. Khorenko, A. Mofor, A. Bakin, E. Khorenko, S. Ehrich, H. Wehmann, A. Schlachetzki, and F. J. Tegude, "High-Speed InP-based Resonant Tunnelling Diode on Silicon Substrate," in *IEEE 2005 Proc. 35th European Solid-State Device Research Conf.*, Grenoble, France, pp. 257–260.

[45] R. J. Hill, C. Park, J. Barnett, J. Price, J. Huang, N. Goel, W. Y. Loh, J. Oh, C. E. Smith, P. Kirsch, P. Majhi, and R. Jammy, "Self-aligned III-V MOSFETs heterointegrated on a 200 mm Si substrate using an industry standard process flow," in *IEEE 2010 Int. Electron Devices Meeting*, San Francisco, CA, pp. 6.2.1 – 6.2.4.

[46] F. Olsson, "Selective epitaxy of indium phosphide and heteroepitaxy of indium phosphide on silicon for monolithic integration," Ph.D. dissertation, School of Information and Communication Technology, Swedish Royal Institute of Technology, 2008.

[47] G. Doucas, J. H. Mulvey, M. Omori, J. Walsh, and M. F. Kimmitt, "First observation of Smith-Purcell radiation from relativistic electrons," *Phys. Rev. Lett.*, vol. 69, no. 12, pp. 1761–1764, Sept. 1992.

[48] K. J. Woods, J. E. Walsh, R. E. Stoner, H. G. Kirk, and R. C. Fernow, "Forward Directed Smith-Purcell Radiation from Relativistic Electrons," *Phys. Rev. Lett.*, vol. 74, no. 19, pp. 3808–3811, May 1995.

[49] Y. Shibata, S. Hasebe, K. Ishi, S. Ono, M. Ikezawa, T. Nakazato, M. Oyamada, S. Urasawa, T. Takahashi, T. Matsuyama, K. Kobayashi, and Y. Fujita, "Coherent Smith-Purcell radiation in the millimeter-wave region from a short-bunch beam of relativistic electrons," *Phys. Rev. E*, vol. 57, no. 1, pp. 1061–1074, Jan. 1998.

[50] J. H. Brownell and G. Doucas, "Role of the grating profile in Smith-Purcell radiation at high energies," *Phys. Rev. ST - Accel. Beams*, vol. 8, no. 9, pp. 091 301–11, Sept. 2005.

[51] M. Goldstein, J. E. Walsh, M. F. Kimmitt, J. Urata, and C. L. Platt, "Demonstration of a micro far-infrared Smith-Purcell emitter," *Appl. Phys. Lett.*, vol. 71, no. 4, pp. 452–454, July 1997.

[52] K. Ishiguro and T. Tako, "An Estimation of Smith-Purcell Effect as the Light Source in the Infra-red Region," *Opt. Acta*, vol. 8, no. 1, pp. 25–31, Jan. 1961.

[53] G. Toraldo di Francia, "On the theory of some Cerenkovian effects," *Il Nuovo Cimento*, vol. 16, no. 1, pp. 61–77, Jan. 1960.

[54] P. M. van den Berg, "Smith-Purcell radiation from a line charge moving parallel to a reflection grating," *J. Opt. Soc. Am.*, vol. 63, no. 6, pp. 689–698, June 1973.

[55] ——, "Smith-Purcell radiation from a point charge moving parallel to a reflection grating," *J. Opt. Soc. Am.*, vol. 63, no. 12, pp. 1588–1597, Dec. 1973.

[56] F. S. Rusin and G. D. Bogomolov, "Orotron–An electronic oscillator with an open resonator and reflecting grating," *Proceedings of the IEEE*, vol. 57, no. 4, pp. 720–722, Apr. 1969.

[57] Y. A. Grishin, M. R. Fuchs, A. Schnegg, A. A. Dubinskii, B. S. Dumesh, F. S. Rusin, V. L. Bratman, and K. Mobius, "Pulsed Orotron–A new microwave

source for submillimeter pulse high-field electron paramagnetic resonance spectroscopy," *Rev. Sci. Instrum.*, vol. 75, no. 9, pp. 2926–2936, Sept. 2004.

[58] V. Bratman, N. Ginzburg, Y. Grishin, B. Dumesh, F. Rusin, and A. Fedotov, "Pulsed wideband orotrons of millimeter and submillimeter waves," *Radiophys. and Quantum Electronics*, vol. 49, no. 11, pp. 866–871, Nov. 2006.

[59] V. L. Bratman, B. S. Dumesh, A. E. Fedotov, P. B. Makhalov, B. Z. Movshevich, and F. S. Rusin, "Terahertz Orotrons and Oromultipliers," *IEEE Trans. Plasma Sci.*, vol. 38, no. 6, pp. 1466–1471, June 2010.

[60] J. Urata, M. Goldstein, M. F. Kimmitt, N. A, P. C, and J. E. Walsh, "Superradiant Smith-Purcell Emission," *Phys. Rev. Lett.*, vol. 80, no. 3, pp. 516–519, Jan. 1998.

[61] C. A. Flory, "Analysis of super-radiant Smith-Purcell emission," *J. Appl. Phys.*, vol. 99, no. 5, pp. 054 903–1–11, Mar. 2006.

[62] E. Gornik, W. Boxleitner, V. Rosskopf, M. Hauser, C. Wirner, and G. Weimann, "Smith-Purcell effect in GaAs/AlGaAs heterostructures," *Superlattice Microst.*, vol. 15, no. 4, pp. 399–399, June 1994.

[63] H. Kroemer, "Proposed negative-mass microwave amplifier," *Phys. Rev.*, vol. 109, no. 5, p. 1856, Mar. 1958.

[64] ——, "The physical principles of a negative-mass amplifier," *Proceedings of the IRE*, vol. 47, no. 3, pp. 397–406, Mar. 1959.

[65] ——, "Theory of the Gunn effect," *Proceedings of the IEEE*, vol. 52, no. 12, pp. 1736–1736, Dec. 1964.

[66] P. Butcher and W. Fawcett, "Stable domain propagation in the Gunn effect," *Br. J. Appl. Phys.*, vol. 17, no. 11, pp. 1425–1432, Nov. 1966.

[67] J. B. Gunn, "Properties of a Free, Steadily Travelling Electrical Domain in GaAs," *IBM J. Res. Develop.*, vol. 10, no. 4, pp. 300–309, July 1966.

[68] M. Shoji, "Two-dimensional Gunn-domain dynamics," *IEEE Trans. Electron Devices*, vol. 16, no. 9, pp. 748–758, Sept. 1969.

[69] ——, "Functional bulk semiconductor oscillators," *IEEE Trans. Electron Devices*, vol. 14, no. 9, pp. 535–546, Sept. 1967.

[70] M. Shoji and P. W. Dorman, "Capacitively coupled GaAs current waveform generator," *Proceedings of the IEEE*, vol. 56, no. 9, pp. 1613–1614, Sept. 1968.

[71] J. B. Gunn, "On the shape of traveling domains in gallium arsenide," *IEEE Trans. Electron Devices*, vol. 14, no. 10, pp. 720–721, Oct. 1967.

[72] P. N. Butcher, W. Fawcett, and C. Hilsum, "A simple analysis of stable domain propagation in the Gunn effect," *Br. J. Appl. Phys.*, vol. 17, no. 7, pp. 841–850, July 1966.

[73] M. Shur, *GaAs Devices and Circuits*. New York, NY: Plenum Press, 1987.

[74] C. Hilsum, "Simple empirical relationship between mobility and carrier concentration," *Electron. Lett.*, vol. 10, no. 13, pp. 259–260, June 1974.

[75] R. Wangsness, *Electromagnetic Fields*. Hoboken, NJ: Wiley, 1986.

[76] C. Li, A. Khalid, S. H. Paluchowski, M. C. Holland, G. Dunn, and D. S. Cumming, "Design, fabrication and characterization of $In_{0.23}Ga_{0.77}As$-channel planar Gunn diodes for millimeter wave applications," *Solid-State Electron.*, vol. 64, no. 1, pp. 67–72, Oct. 2011.

[77] S. C. Binari, H. L. Grubin, and P. E. Thompson, "Notched InP Planar Transferred-Electron Oscillators," in *IEEE 1982 Int. Electron Devices Meeting*, San Francisco, CA, pp. 770–773.

[78] H. Eisele and R. Kamoua, "Submillimeter-wave InP Gunn devices," *IEEE Trans. Microw. Theory Tech.*, vol. 52, no. 10, pp. 2371–2378, Oct. 2004.

APPENDIX A

PULSE FUNCTION F AND SPIKE FUNCTION G

Section 3 contains derivations for the vector and scalar potentials of the periodic image charge packet induced by a single charge on the teeth of a nearby metallic grating. These derivations led to the definition of the "variable pulse function" $F(\boldsymbol{r}, t)$. In 3D, $F(\boldsymbol{r}, t)$ was defined in terms of the reduced velocity $\beta = v/c$ as:

$$F(\boldsymbol{r}, t) = \left(\frac{1}{\pi}\right) \sum_{n=0}^{\frac{L}{P}-1} \left\{ \tan^{-1}\left[\frac{vt - (\beta r + nP)}{b}\right] - \tan^{-1}\left[\frac{vt - (\beta r + nP + \ell)}{b}\right] \right\}$$

The same function arises in 2D calculations, with the only difference being in the definition of the observation point P. In 2D, P is located at $\boldsymbol{\rho}$ instead of $\boldsymbol{r}$:

$$F(\boldsymbol{\rho}, t) = \left(\frac{1}{\pi}\right) \sum_{n=0}^{\frac{L}{P}-1} \left\{ \tan^{-1}\left[\frac{vt - (\beta \rho + nP)}{b}\right] - \tan^{-1}\left[\frac{vt - (\beta \rho + nP + \ell)}{b}\right] \right\}$$

This Appendix explores the properties of this function and its derivatives in detail. Focusing on the 2D case, $F(\boldsymbol{\rho}, t)$ is rewritten to highlight the arguments:

$$F(\boldsymbol{\rho}, t) = \left(\frac{1}{\pi}\right) \sum_{n=0}^{\frac{L}{P}-1} \left[\tan^{-1}(a_1) - \tan^{-1}(a_2) \right] \tag{A.1}$$

$$\text{where } a_1 = \left(\frac{1}{b}\right)\Big(vt - (\beta \rho + nP)\Big)$$

$$\text{and } a_2 = \left(\frac{1}{b}\right)\Big(vt - (\beta \rho + nP + \ell)\Big)$$

Each term of the finite sum in $F(\boldsymbol{\rho}, t)$ defined in Equation (A.1) corresponds to a single pulse whose specific shape depends on the magnitudes of a_1 and a_2. The sum over all grating teeth yields a finite train of pulses. In the limit $b \to 0$, $F(\boldsymbol{\rho}, t)$ becomes a train of *rectangular unit pulses*. Recall that the inverse tangent function $\tan^{-1}(\theta)$ approaches $-\pi/2$ as its argument $\theta \to -\infty$ and $\pi/2$ as $\theta \to +\infty$. Therefore, dividing the inverse tangent by π gives a function that approximates a unit step function from $-1/2$ to $+1/2$ and crosses the x-axis when its argument is equal to zero. The "sharpness" of the step function is determined by the "strength" of its argument as shown in Figure A.1, using a real parameter α to increase the strength of the argument.

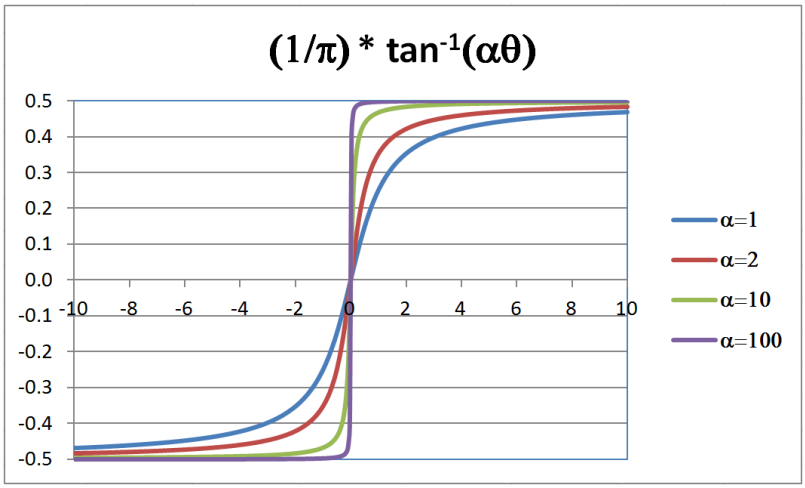

Figure A.1: The inverse tangent divided by π approximates a unit step function. The approximation improves with increasing strength of the argument α.

Therefore, the *difference* of a pair of inverse tangents whose arguments differ by an amount ϵ approximates a rectangular pulse of unit height and width ϵ when the arguments are "strong", as illustrated in Figure A.2.

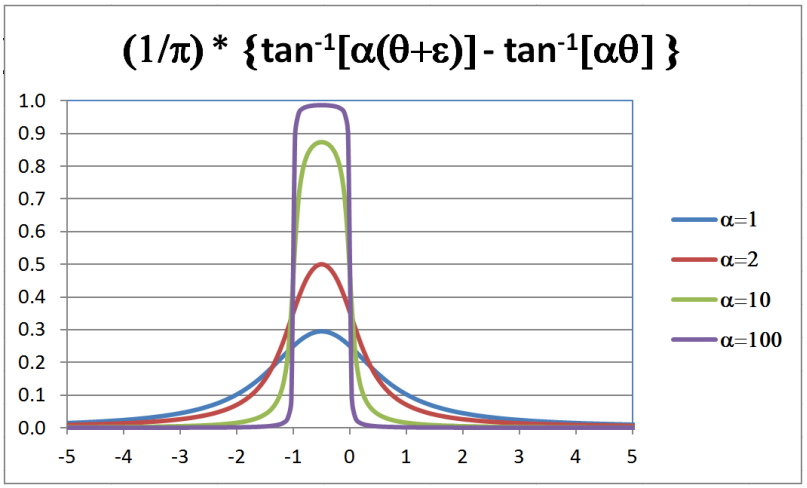

Figure A.2: Difference of inverse tangents from Figure A.1 and their images translated along the x-axis by a value $\epsilon = 1$.

Rewriting the arguments of the inverse tangent terms in Equation (A.1) in terms of the grating duty factor (or grating density) δ, the Smith-Purcell radiation frequency f and associated wavelength λ:

$$\delta = \frac{\ell}{P} \tag{A.2}$$

$$f = \frac{v}{P} \tag{A.3}$$

$$\lambda = \frac{cP}{v} \tag{A.4}$$

These expressions for a_1 and a_2 perhaps more clearly illustrate the relationship of $F(\boldsymbol{\rho}, t)$ to the device geometry:

$$a_1 = \left(\frac{\beta}{b}\right)\left(ct - r - n\lambda\right) \tag{A.5}$$

$$a_2 = \left(\frac{\beta}{b}\right)\left(ct - r - n\lambda - \delta\lambda\right) \tag{A.6}$$

Comparison to Figure A.2 with the definitions:

$$\alpha = \frac{\beta}{b} \tag{A.7}$$

$$\theta = ct - r - n\lambda \tag{A.8}$$

$$\epsilon = \delta\lambda \tag{A.9}$$

shows that each term in the sum of Equation (A.1) is indeed a pulse of width $\delta\lambda$.

Moreover, the form of the arguments as given in Equations (A.5) and (A.6) show the physical interpretation of the wave train described by $F(\boldsymbol{\rho}, t)$. At fixed time t, the maximum possible signal distance for an electromagnetic wave is ct. The leading edges of each pulse occurs inside this maximum distance with spatial periodicity λ as expected, since the edge of the pulse is zero every time that $r = ct - n\lambda$. The trailing edges follow the same trend a spatial distance $\delta\lambda$ behind the leading edges.

The interpretation follows in exactly the same manner when looking at $F(\boldsymbol{\rho}, t)$ as a function of time at fixed observation distance r. The arguments a_1 and a_2 can be rearranged in a "time-centric" format by recombining β in Equations (A.5) and (A.6) with the spatial terms. The reciprocal of the Smith-Purcell frequency f given in Equation (A.3) is its associated time period $T = 1/f = P/v$. In terms of T, the leading-edge argument a_1 is seen to be zero whenever $t = R/c + nT$. The trailing edge of each pulse is delayed by a time ℓ/v relative to the leading edge.

The above discussion illustrates the "switching" behavior of the vector and scalar potentials identified in Section 3 for *small* impact parameter b. Another interesting property of $F(\boldsymbol{\rho}, t)$ is that it also displays the intuitively correct "smearing" behavior in the opposite limit of *large* impact parameter b. Figure A.3 illustrates how increasing the charge-grating distance b has the intuitively expected effect of spreading out or "smearing" the image charge across multiple grating teeth.

For definiteness consider the case of a four-tooth grating observed at fixed observation distance ρ. At small values of impact parameter b, each tooth is well-defined and $F(t)$ approaches its maximum value of unity. At progressively larger values of b, the pulses from adjacent grating teeth begin to interfere with each other as the image charge spreads across multiple teeth.

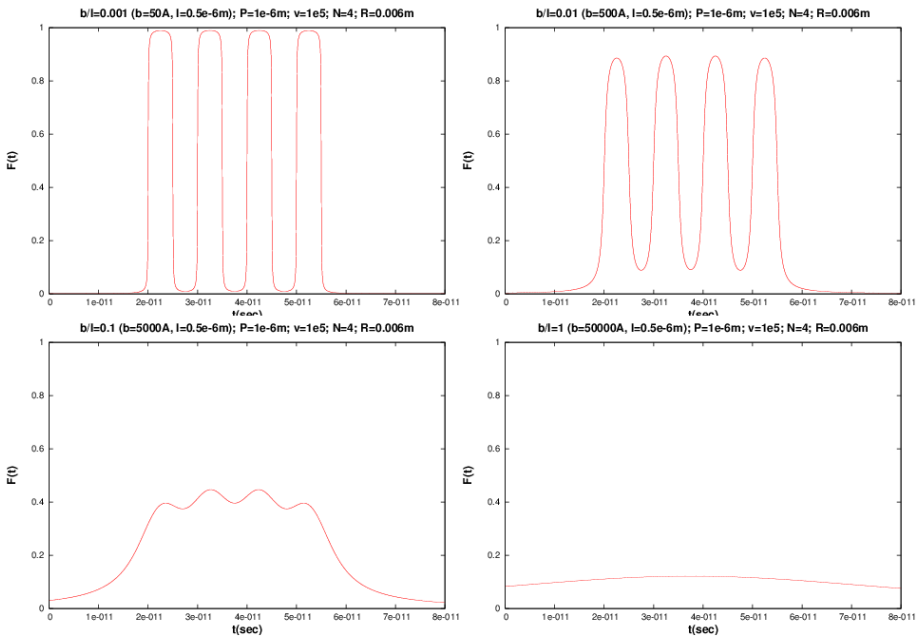

Figure A.3: Increasing b at fixed observation distance ρ "spreads out" the image charge induced on the grating teeth. When b is comparable to the grating period P, the charge induces no appreciable image charge on the grating.

At large values of the impact parameter b – specifically when the charge-grating separation becomes comparable to the grating period P – the charge does not interact with the grating at all. There is only a mimimal rise in $F(t)$ as the charge passes the grating, with no discernible tooth features visible.

Calculation of the electric field from the vector and scalar potentials requires the

computation of both the time and space derivatives of $F(\boldsymbol{\rho}, t)$. The above discussion showed that in the limit of small b, $F(\boldsymbol{\rho}, t)$ represents a step-like function in both space and time. Therefore it is reasonable to expect that the partial derivatives of $F(\boldsymbol{\rho}, t)$ with respect to ρ and t will involve a "delta-like" function in the same limit. It is useful to first recall the derivative of the inverse tangent function:

$$\frac{d}{dx}\tan^{-1}(\alpha x) = \frac{\alpha}{1+(\alpha x)^2} \tag{A.10}$$

The partial derivative of $F(\boldsymbol{\rho}, t)$ with respect to the time t is

$$\frac{\partial F}{\partial t} = \left(\frac{1}{\pi}\right)\left(\frac{v}{b}\right)\sum_{n=0}^{\frac{L}{P}-1}\left\{\frac{1}{1+\left[\frac{vt-(\beta\rho+nP)}{b}\right]^2} - \frac{1}{1+\left[\frac{vt-(\beta\rho+nP+\ell)}{b}\right]^2}\right\} \tag{A.11}$$

$$\frac{\partial F}{\partial t} = \frac{v}{\pi b}\, G(\boldsymbol{\rho}, t) \tag{A.12}$$

Similarly, the partial derivative of $F(\boldsymbol{\rho}, t)$ with respect to ρ is

$$\frac{\partial F}{\partial \rho} = \left(\frac{1}{\pi}\right)\left(\frac{-\beta}{b}\right)\sum_{n=0}^{\frac{L}{P}-1}\left\{\frac{1}{1+\left[\frac{vt-(\beta\rho+nP)}{b}\right]^2} - \frac{1}{1+\left[\frac{vt-(\beta\rho+nP+\ell)}{b}\right]^2}\right\} \tag{A.13}$$

$$\frac{\partial F}{\partial \rho} = -\left(\frac{\beta}{\pi b}\right)G(\boldsymbol{\rho}, t) = -\frac{1}{c}\frac{\partial F}{\partial t} \tag{A.14}$$

Both partial derivatives involve the function $G(\boldsymbol{\rho}, t)$, defined as

$$G(\boldsymbol{\rho}, t) = \sum_{n=0}^{\frac{L}{P}-1}\left\{\frac{1}{1+\left[\frac{vt-(\beta\rho+nP)}{b}\right]^2} - \frac{1}{1+\left[\frac{vt-(\beta\rho+nP+\ell)}{b}\right]^2}\right\} \tag{A.15}$$

The function $G(\boldsymbol{\rho}, t)$ describes an alternating series of positive and negative spikes

as shown in Figure A.4. In the limit of a "very strong" argument ($b \to 0$), the spikes in $G(\boldsymbol{\rho}, t)$ approach unit height, corresponding to the rising and falling edges of the pulses of $F(\boldsymbol{\rho}, t)$. At this point, the reader may wonder why so much effort has been made to so exhaustively document such seemingly anticlimactic (and perhaps even obvious) results. There are two reasons – the first is to clearly illustrate the simplicity of the physics behind the Smith-Purcell effect at small b.

The second – and perhaps more important reason – is to demonstrate the wide range of behaviors this simple theory satisfactorily explains. The results of the research show that the design parameter space accessible by current and future process technologies covers a wide frequency range. The simple theory developed herein allows future analog designers and device engineers to specifically optimize output waveforms for differentiated applications.

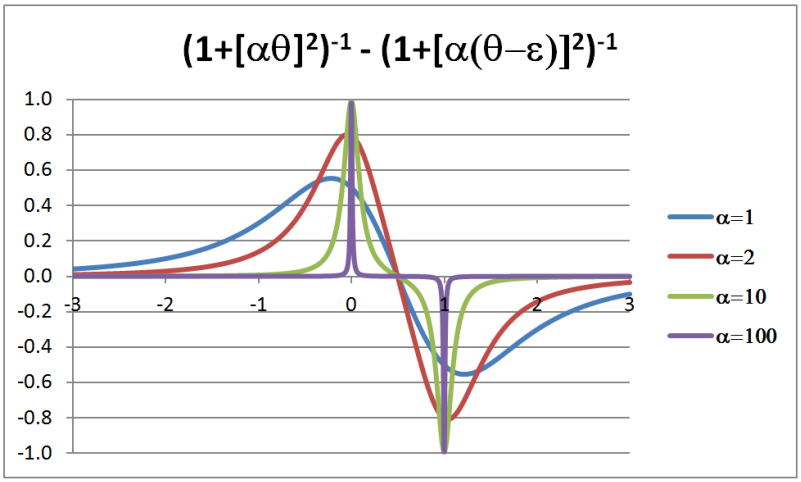

Figure A.4: $G(\boldsymbol{\rho}, t)$ defined in the derivation of the electric field generated by a point charge interacting with a single grating tooth corresponding to the rectangular pulse associated with the potential, as shown in Figure A.2.